



UNIVERSITY OF OSNABRUECK

DOCTORAL THESIS

Nondestructive Investigation of Guest Evaporation and Dynamics in Nanoporous Hosts.

Author:

Sachar Ichilmann, M.Sc.

Supervisors:

Prof. Dr. Martin Steinhart

Prof. Dr. Georg Fytas

Institute for Chemistry of New Materials

November 2015

Contents

Contents	i
1 Introduction	1
2 Nanoporous model hosts systems	4
2.1 Nanoporous materials	4
2.1.1 Morphological properties	4
2.1.2 Applications of nanoporous materials	6
2.2 Self ordered anodic aluminium oxide (AAO)	7
2.2.1 General information	7
2.2.2 AAO membranes used for experiments	11
2.3 Controlled Porous Glass (CPG)	13
2.3.1 General information	13
2.3.2 CPG membranes used for evaporation dynamics measurements	17
2.3.3 CPG membranes used for the BLS experiments	18
3 Experimental methods	20
3.1 Confocal laser scanning microscopy (CLSM)	20
3.1.1 General information	20
3.1.2 Fluorescence mapping in porous media	22
3.1.3 Experimental setup	23
3.2 Time resolved 3D orientation spectroscopy	24
3.2.1 General information	24
3.2.2 Experimental setup	25
3.3 Brillouin Light Scattering Spectroscopy	26
3.3.1 General information	26
3.3.2 Experimental setup	39
3.4 Thermal Analysis	39
3.4.1 General information	39
3.4.1.1 Differential Scanning Calorimetry (DSC)	39
3.4.1.2 Thermogravimetric analysis (TGA)	41
3.4.2 Experimental setup	42
4 Evaporation of volatile guests from hosts with sponge-like continuous pore systems	44

4.1	Introduction	44
4.2	Evaporation dynamics of ethanol in Controlled Porous Glass observed with confocal microscopy	47
4.3	Spatio-temporal mapping of fluorescence intensity/evaporation using stacks of CLSM images	49
4.4	Investigation with thermal analysis (combined TGA/DSC)	51
4.5	Calculation of enthalpy of evaporation	55
4.6	Discussion	57
4.6.1	Adiabatic conversion of an unstable liquid phase into a gas phase	57
4.6.2	Evaporation bursts vs. classical Haines jumps	59
4.6.3	Initiation mechanisms of adiabatic evaporation jumps	60
4.7	Conclusion and outlook	61
5	Evaporation of volatile guests from hosts with straight cylindrical pores	63
5.1	Introduction	63
5.2	Evaporation dynamics of ethanol in AAO observed with confocal microscopy	64
5.3	Intensity redistribution of R6G molecules in AAO as function of time and space	67
5.4	Discussion	71
5.5	Conclusion and outlook	75
6	Non-volatile liquid guests in nanoporous hosts: characterization by BLS spectroscopy	77
6.1	Introduction	77
6.2	Results	79
6.3	Discussion	82
6.3.1	Mode-guiding vs. effective medium	82
6.3.2	Sound velocity inside pore walls	88
6.3.3	Comparison of sound velocities of infiltrated and non-infiltrated CPGs	88
6.3.3.1	CPG2	89
6.3.3.2	CPG9	89
6.3.3.3	CPG26	90
6.3.4	Restricted mobility of PDMS infiltrated in CPG	90
6.4	Conclusion and outlook	91
7	Self diffusion of non-volatile fluids in quasi one-dimensional confinement	93
7.1	Introduction	93
7.2	Modification of the mathematical model of Fluorescence Recovery After Photobleaching (FRAP) method for one dimensional geometries	95

7.3	Algorithmic parameterization and search for parameters	100
7.4	Experimental implementation and tentative results	104
7.5	Conclusion and outlook	110
8	Summary and outlook	112
Bibliography		116
Declaration of Authorship		131
Acknowledgements		132

Chapter 1

Introduction

One of the most interesting and promising trends in material science of recent years is the development of the principles of the preparation of polymer nanocomposites and the methods of their study. Especially there is a need for non destructive investigation methods, due to complexity of studied systems that is associated with complicated manufacturing and the highest purity of starting materials. Samples that have not lost their physical integrity during the investigation process can be used for their direct purpose.

By definition [1], composite materials consist of two or more phases with a clear interface. Liquid polymer substance inside a nanoporous medium is a simple model system for a nanocomposite material [2], [3]. Two nanoporous media that are often used for production of nanocomposites are controlled porous glass (CPG)[4] and porous aluminium oxide (AAO) [5]. These materials have contrasting and well-documented [4],[5] geometric properties.

There are still many aspects of the production and properties of nanocomposites on the basis of AAO and CPG that require particular attention. **Evaporation of volatile liquid guest phase from porous host** is a key factor in processes such as production of nanoporous polymer membranes by thermally-induced phase separation and by swelling-induced morphology reconstruction[6],[7]. Evaporation of liquid phase generally plays an important role in filling a solid phase with different functional materials[8], like infiltration of high viscous polymers into the porous matrix using ethanol or any other solvent. The process of evaporation of volatile liquids from porous membranes has not been sufficiently studied up to date. Here two non destructive methods are presented that allow to study this process in real time using combined TGA/DSC analysis and real time confocal microscopy using

fluorescing markers.

Optical and acoustical properties of porous nanocomposites differ significantly from the properties of empty porous membranes of the same type. Being infiltrated with non-volatile component, such as liquid polymer melt, porous membranes change their phononic properties[9]. These properties were not studied for a system consisting of CPG with infiltrated liquid polymer melt. Here an extensive study is presented for empty CPG membranes with different pore diameters and CPG membranes infiltrated with liquid polymer melt.

The physics of self-diffusion of infiltrated non-volatile polymer melts inside porous nanocomposites differ significantly from those in free volume [10], [11]. Existing methods such a variety of NMR techniques are limited to relatively short diffusion time. When it comes to very long observation of diffusion process at low temperatures and for long chain length, a new method is needed that is presented in the framework of this thesis. This method is based on the observation of fluorescence recovery after bleaching using confocal microscopy in 1D and evaluating these data using specially taylored mathematical model.

This thesis is divided into eight chapters. In the following **second chapter** the nanoporous model host systems are described and characterized. Main properties of porous materials are defined and it is shown, what do the two investigated systems (CPG and AAO) have in common and where are the main differences. It is shown, how these materials are created and what are their main applications.

The **third chapter** describes in detail the experimental methods that have been used in the framework of this thesis. All these methods are united by the fact that they can be used or modified to the extent so as not to destroy the integrity of the investigated samples.

The chapters **four and five** deal with evaporation kinetics of volatile fluids from two different porous hosts with completely different morphologies - AAO and CPG. The **fourth chapter** describes the results of a study of the dynamics of evaporation of ethanol from a controlled porous glass. The studies were conducted by confocal microscopy using fluorescent molecules as well as directly by thermogravimetry and DSC methods.

The **fifth chapter** describes the results of a study of the dynamics of evaporation and behaviour of fluorophores in self ordered porous alumina. The research was conducted by confocal microscopy. During the investigation of the behaviour of

the solution of fluorophores, the focus was shifted from the dynamics of evaporation on the behaviour of fluorophores because a non-linear effect of fluorescence enhancement was observed in the last phase evaporation.

Chapters seven and eight deal with non-volatile fluids inside AAO and CPG. Polydimethylsiloxane (PDMS), was studied extensively with BLS method in the **sixth chapter**. Pure and infiltrated CPG membranes with different mean pore diameters are studied. It was shown that BLS method can be applied as a destruction free technique to study different properties of optically transparent nanocomposites.

The **seventh chapter** deals with the Fluorescence Recovery After Bleaching (FRAP) method inside AAO. It was shown that using the same mapping technique, as in the fourth and fifth chapter, it is possible to collect fluorescence data from special polymer mixture. A mathematical model is developed to evaluate the results of the quasi one-dimensional diffusion. The **eights chapter** is the summary and outlook.

Chapter 2

Nanoporous model hosts systems

2.1 Nanoporous materials

2.1.1 Morphological properties

In general, a nano-porous material can be defined as a solid containing in its volume free spaces in form of cavities, channels or pores with dimensions of few nanometer up to hundred nanometer [12]. The first important parameter that characterizes the structure of a porous body is **porosity**. Porosity is the proportion of pore volume of the total volume of the porous body. It is a dimensionless quantity that varies from 0 to 1 (or 0 to 100%). 0 corresponds to a material without pores. A 100% porosity is unattainable, but there are materials (such as aerogels [13]) that are approaching this value. The second parameter is the **degree of openness** of the pores. Regarding this factor there are two main types of porous materials - with open and enclosed pores, as is illustrated on Figure 2.1. In the case of open pores the porous structure is connected with environment. The second type of porous material, which will not be discussed in detail in this thesis, are samples with enclosed pores. The porous structure does not border with surface, pores are separated. Porous structure defines some physical properties such as density, thermal conductivity, acoustic properties and so on. Figure 2.1 illustrates the principle of ordered and disorder, enclosed and open pores.

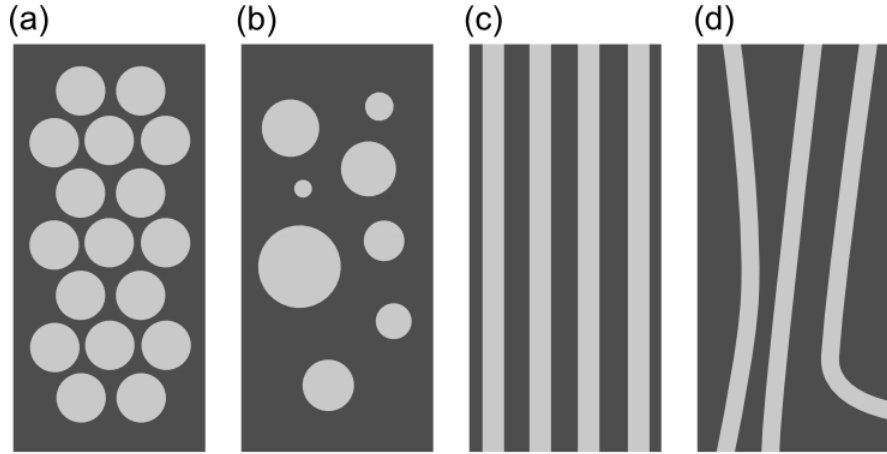


FIGURE 2.1: Types of pore morphologies. (a) Ordered pores with non penetrating character, (b) disordered pores with non penetrating character (c) ordered pores with penetrating character, (d) disordered pores with penetrating character (for instance controlled porous glass).

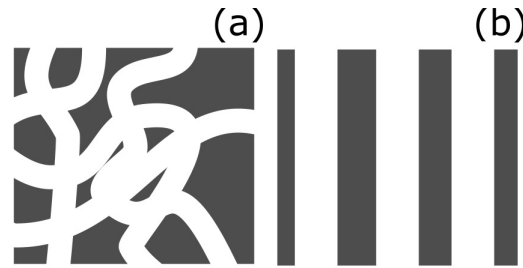


FIGURE 2.2: Schematical illustration of two pore morphologies - sponge like and parallel cylindrical

The structure of the porous body in case of opened disordered pores is divided into the granulate and spongy type. Granulate porous body (eg, silica gel) consists of fused particles of different shapes and sizes, and pores are gaps between these particles and their ensembles. It is not possible to distinguish individual primary particles in the spongy bodies (e.g. porous glass) and pores therein constitute a network of channels and cavities of different shape and variable cross section. Figure 2.2 illustrates the main difference between the two materials that are used as host systems in the framework of this thesis - the sponge like pores (a) and parallel cylindrical pores (b). The main difference between these two types of porous membrane is the interconnection of the pores. In the first time the porous phase builds a network of interconnected empty spaces, in the second type each single pore is a well separated cylinder. Therefore one can easily study the behavior of liquids in both, totally interconnected and well separated morphologies.

2.1.2 Applications of nanoporous materials

A closer look at the properties of nanoporous materials reveals following important factors:

- **High adsorption capacity** is caused due to the very large surface-area-to-volume ratio (both inner and outer surfaces) [14].
- **High selectivity** can be explained with two parameters - the surface chemistry [15] and highly monodisperse distribution of the average pore diameter [16]. The surface chemistry allows for instance to control the wetting ability and therefore the types of attached molecules. The high monodispersity of the pores allows to control the geometrical properties of the infiltrated materials, limiting their maximum size.
- **Controllable adsorption** follows from the chemical properties of the surface. First, as mentioned above, chemical properties of the surface define the adsorption capabilities of the material. Second, those properties can be modified selectively by adding different molecules to the functional groups, which makes the surface for instance wetting or non wetting.
- **Mechanical properties** of porous materials include such important parameters as hardness, strength and ductility. The combination of these parameters provides a variety of geometric shapes and sizes of outcoming materials.
- **Optical properties** of nanoporous materials are expressed in their transparency to radiation of different wavelength allowing investigation with several optical techniques such as confocal microscopy.
- Finally, **high stability and durability** of specimen, caused by their chemical and physical structure opens a wide field of application for this class of materials, both in fundamental research and for solving practical problems.

Porous permeable materials are widely used as filters for mechanical purification of liquids and gases, their drying and heating, for selective filtering, separation and enrichment of gases [17]. They can also be used as a dust collector, desalination, nuclear membrane filters and so on. Nature and kinetics of the flow of gases and liquids through porous system is mainly determined by the ratio of the pore

size and size of molecules of the penetrating phase. Effect of adsorption and electrostatic forces, concentration, orientation and distribution of pore size of the material also plays a very important role.

2.2 Self ordered anodic aluminium oxide (AAO)

2.2.1 General information

Anodization [18] [5] is technologically simple and effective method for synthesis of self-organized nano-structured materials with a periodic pore arrangement. Porous anodic oxide film may be grown on materials such as silicon, indium phosphide, titanium [19], niobium, tantalum, tin, etc. However, aluminium is the only material that yields stable membranes. Self ordered anodic alumina (schematic representation on Figure 2.3 [20]) has straight aligned cylindrical pores that are uniform in diameter with a tortuosity of 1, unique nanoscale cellular porous structure, high mechanical stability and interesting dielectric and optical properties[21]. By changing the anodizing process one achieves a large variety of different morphologies and electrophysical properties.

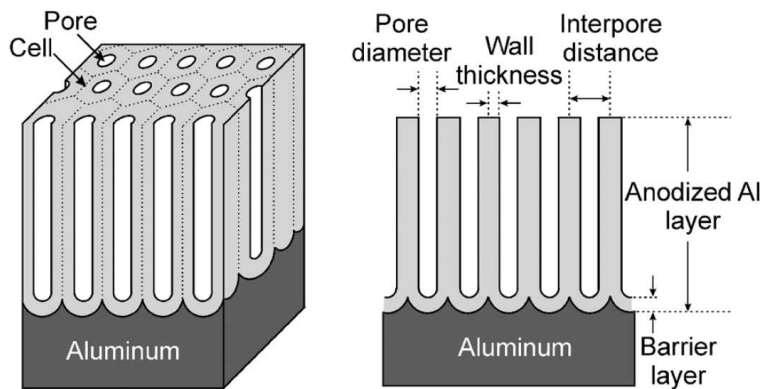


FIGURE 2.3: Idealized structure of anodic porous alumina and a cross-sectional view of the anodized layer. Figure taken from [20].

Anodic alumina can be used as a matrix for creating nano-size structures and composite materials [22], [23]. Filling the pores with dielectric materials makes it

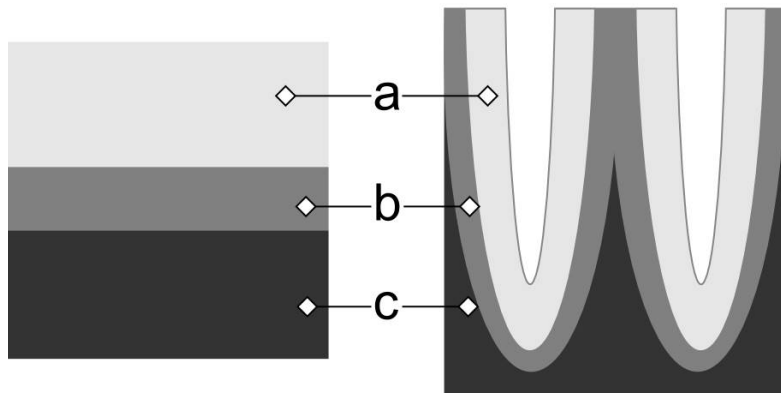


FIGURE 2.4: Two types of anodic films: barrier (left) and porous (right). a - outer oxide layer, b - inner oxide layer, c - aluminum.

possible to create a layer with very low permittivity [24]. The use of such materials as substrates of integrated circuits allows to considerably reduce the capacitive coupling between the elements and thereby increase the speed of developed devices. Another very common application of porous alumina oxide is template synthesis [25], [26] and filtering [27], [28]. These two applications are possible due to the pore morphology of self ordered porous alumina [20] - the pores are straight aligned, cylindrical and uniform in diameter, which makes it possible to fill the pores or to use them as filtering system in case when both, the bottom und top of the AAO membrane is opened. The narrow and separated nature of the pores of AAO is well illustrated in Figure 2.3

The surface of aluminium is oxidized spontaneously in air [29]. It happens due to large negative change in Gibbs free energy. Oxidation also occurs when a surface is wetted with water [30]. The oxide layer formed on the metal surface has a small thickness (5 to 20 nm) and prevents the metal from further oxidation. It is possible to control the process of surface oxidation using the electrochemical oxidation method [31] - anodizing aluminum in aqueous electrolyte solutions. Thus it is possible to obtain a thicker layer of aluminum oxide. The growth of oxide occurs at the anode (the aluminium substrate) and hydrogen ions are reduced at the cathode. The reaction intensity depends on the electrode potential, temperature and the pH level, which in turn are determined by the electrolyte used. Depending on the synthesis conditions, particularly on the electrolyte used, two kinds of anodic films can be formed - barrier type and porous type [32] (see Figure 2.4). Barier type can be obtained using electrolytes which do not dissolve the oxide, for instance boric acid solution. Porous film type [5] are formed in slightly soluble electrolytes, such as sulfuric [33], phosphoric [34] and oxalic [35] acid. The aluminum oxide

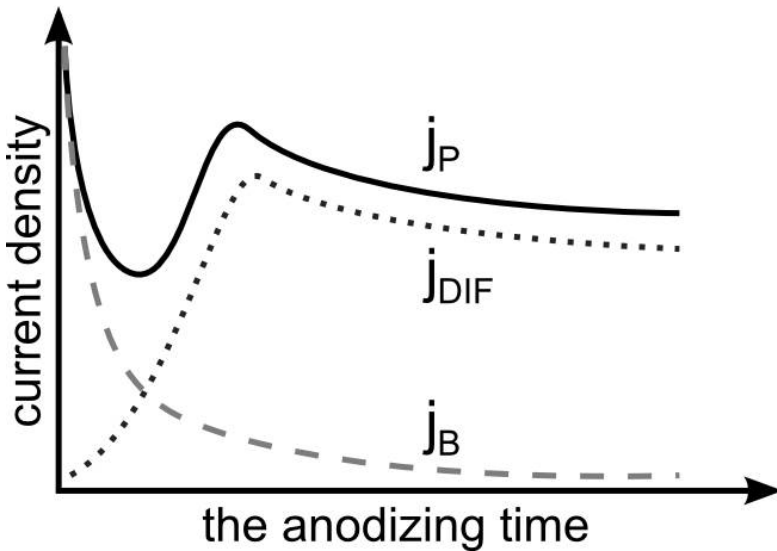


FIGURE 2.5: Kinetics of current density at a constant potential at the initial stage of the anodization process.

films, both the porous and barrier type, are composed of two parts [36] - inner and outer layer (fig. 2.4 a and b). The inner layer (b) is a pure alumina while the outer layer (a) contains various impurity ions. The most important parameters affecting the thickness of the porous film are the temperature, the electrolysis time, current density and the electrolyte used. With increasing temperature, current density increases. However, this does not lead to a significant increase in the rate of film growth since the dissolution rate of the oxide at the interface between the oxide and the electrolyte also increases. When the temperature is too high dissolution rate of the oxide becomes greater than the rate of its formation. As a result, the surface of the aluminum becomes smoother which is called an electrochemical polishing. Figure 2.5 demonstrates current density of oxide layer formation at the initial stage of the anodization process. Current density decreases exponentially with time in case of a formation of barrier type oxide layer (j_B). Transport of ions through the oxide layer is the limiting stage. Increasing the thickness of barrier-type oxide coating reduces the electric field intensity and leads to the cessation of growth of the film.

The current density rapidly decreases during the first stage of film formation of a porous type (j_P). It passes through a minimum, reaches the maximum value and get to the stationary mode. The current density j_P can be described as a sum of the current density j_B and hypothetical current density j_{DIF} which is the difference of porous and barrier current densities. j_B is defined only by the used electrolytes and the magnitude of the applied voltage and j_{DIF} depends on the

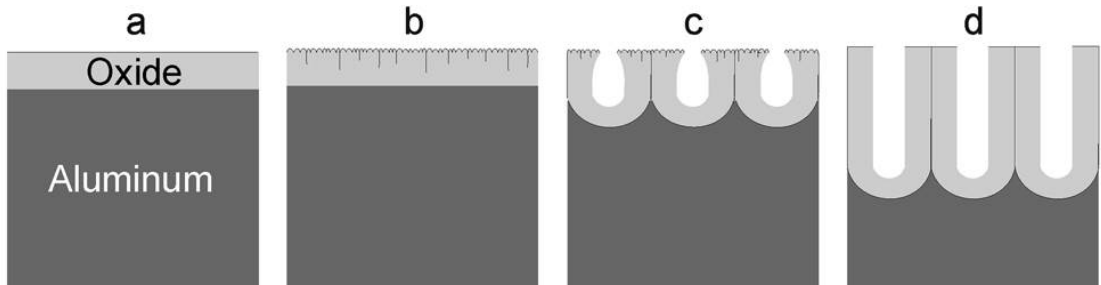


FIGURE 2.6: Four stages of pore formation [20].

used electrolytes, magnitude of the applied voltage and the temperature. The mechanism of pore formation is shown schematically in Figure 2.6. There are four main stages of formation of the porous structure. Aluminum surface is covered with non-conductive film of aluminum oxide barrier type at the beginning of oxidation (fig 2.6a). In this area, the current densities j_P and j_B behave identically. The electric field intensity is distributed non uniformly across the surface of the sample. Localization of field lines on the surface points that are close to the conductive substrate of aluminum leads to increased dissolution of oxide formed in these places(2.6b). This occurs due to the increase of the voltage of the electric field and the local heating. Not all nucleated pores can continue to grow due to the competition of the next points of dissolution of oxide(Figure 2.6c). This leads to a certain reduction in the current density. Ultimately j_P comes to an equilibrium, which implies the uniform growth of the pores(Figure 2.6d).

Self-assembled pore growth occurs during prolonged anodic oxidation [37]. The driving force of this process is the mechanical stress that is caused by repulsive forces between neighbouring pores. There is a two steps procedure for obtaining high alumina ordered arrangement of pores first reported by Masuda and Fukuda [38]. To prepare for this process, a high-purity aluminum surface is purified by acetone and by etching in an acid mixture. Then the aluminum substrate is annealed at a temperature of 500°C [39] for the growth of aluminum metal grains. The grain size of the metal after recrystallization annealing may be more than five millimetres. Increased grain size leads to an increase in the sizes of the domains of the porous film [40]. Mechanical or electrochemical polishing is usually carried out to reduce the surface roughness. Polishing and large grain size contribute to obtaining an ordered porous alumina structures with larger domains. First anodic oxidation is carried out after the pre-treatment. Pores that are formed at the initial stage phase are poorly ordered. Self-ordered porous structure is the result of the repulsive forces between adjacent pores through a long first oxidation. Periodic

structure with a dense hexagonal packing is formed at the interface of the metal oxide. After the first anodic oxidation the oxide film is dissolved in a mixture of Cr_2O_3 with phosphoric acid, without affecting the aluminum substrates to obtain a replica of the bottom of the oxide film that has a self ordered structure. In the subsequent, second anodic oxidation under the same conditions as in the first oxidation, it is possible to obtain an alumina film with a high degree of ordering of pores. If necessary, the pores can be isotropically widened with chemical etching, for example, using 0.5 molar solution of phosphoric acid.

Currently, the basic model to explain the formation of highly ordered hexagonal structure of pores, is the model of mechanical stress [41]. Oxidation takes place at the metal-oxide interface due to migration of oxygen-containing ions of the electrolyte. Dissolution, i.e. reduction in the thickness of the oxide layer is mainly due hydration of formed alumina. Part of Al^{3+} ions diffuse through the oxide layer into solution and do not contribute to the growth of the oxide film in the formation of porous alumina. Growth of the pores perpendicular to the surface of aluminum is the result of the equilibrium of two processes - oxide formation on the oxide-electrolyte interface and the formation of oxide at the oxide metal interface. The oxidation of aluminium metal to the oxide results in an increase in unit cell volume per atom of aluminum. The volumetric expansion in the formation of oxide at the interface metal-oxide leads to a compressive stress in the film plane, which is the driving force in the ordering of the pores. Expansion in the vertical direction contributes to the pore walls growth to the top.

It should be noted that the pores in the macro-scale ranked largely depends on the purity of the starting material. Technical aluminum enables to obtain hexagonal lattice with a low degree of ordering, but the material is advantageous in terms of cost and production in an industrial scale. High-purity aluminum with a purity of more than 99% provides a highly ordered structure, however, is very expensive in terms of material cost.

2.2.2 AAO membranes used for experiments

For evaporation experiments conducted in the framework of this thesis(Chapters 4 and 5), AAO membranes with 60 nm pore diameter and 60 μm membrane thickness where used. These parameters have been chosen because of practical reason. 60 nm diameter is big enough to quickly infiltrate the ethanol solution

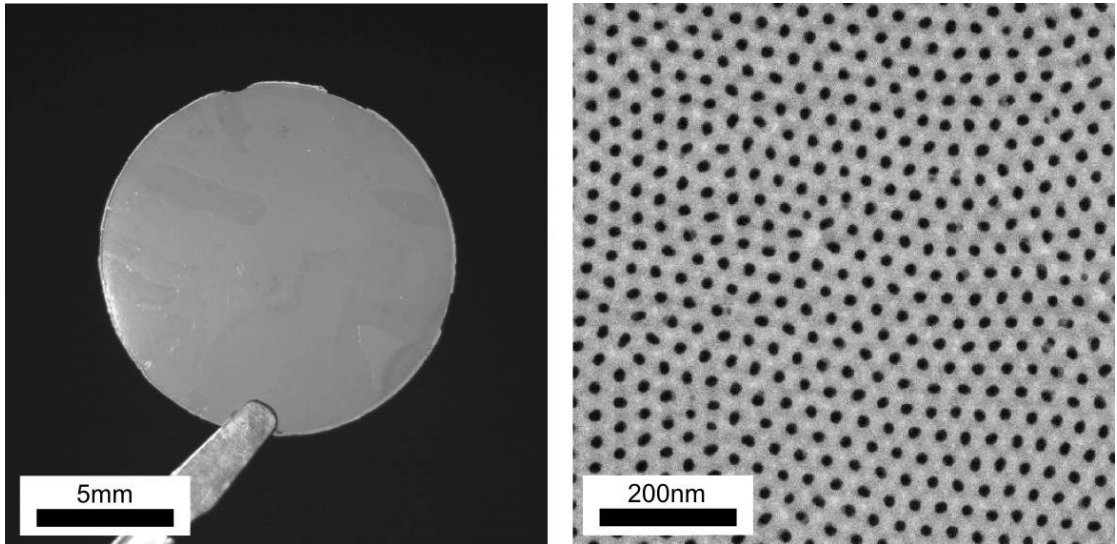


FIGURE 2.7: (left) Picture of a membrane with $100 \mu\text{m}$ thickness and 100 nm average pore diameter, (right) SEM picture of the surface of AAO with 60 nm pore diameter.

with fluorescing dye molecules but its lattice constant (105 nm) is small enough to prevent different scattering effects such as Mie scattering that would make the surface of AAO opaque (as is shown in Figure 2.7 left, for 100 nm AOO).

Mie scattering, or light scattering by a spherical particle is a classical problem of electrodynamics that was resolved in 1908 by Gustav Mie for spherical particles of arbitrary size [42]. The scattering depends on the ratio of the particle size and wavelength that falls on the particle. In case when the particle size is much smaller than the wavelength of the incident light, the scattering is a particular case of Rayleigh scattering. This effect would disturb the measurement because the membrane should be optically transparent (all the details can be found in the corresponding chapter 5). The thickness of $60 \mu\text{m}$ is optimal because of the technical limitations of used confocal microscope setups, this is also going to be discussed in details in chapter 5. The surface of a typical membrane that was used as host system for ethanol evaporation experiments is shown in Figure 2.7 on the right. One can see the well ordered pore morphology. The pore diameter is 60 nm . For FRAP experiments (Chapter 7) AAO membrane with 60 nm pore diameter and $30 \mu\text{m}$ thickness where chosen. The pore diameter should be wide enough to decrease infiltration time but narrow enough to prevent Mie scattering due to the smaller lattice constant. 60 nm is an optimal solution. $30 \mu\text{m}$ thickness allow to decrease infiltration time of polymers.

2.3 Controlled Porous Glass (CPG)

2.3.1 General information

Nanoporous borosilicate glasses [4], also called controlled porous glasses(CPG), hold a special place among the solid nanoporous materials, as they have many interesting and unique properties, such as high mechanical [43] and radiative endurance, high absorption capacity and chemical stability (which can be used for oil spills clean up [44]), high transparency in the visible and near-infrared regions of the spectrum [45], the possibility of implementing a wide range of pore sizes and porosities [46], the possibility of obtaining monoliths of various geometrical sizes [47], possibility of producing composite materials with a work material in the form of individual nanoparticles dispersed in macro volume [48]. CPG membranes are very special, unique in its kind tools for studying physicochemical processes in a limited volume, commensurate with the scale of the processes and the size of the studied objects: space constraints and effective contact with the pore walls cause significant features of state of the guest material compared with the case of its location in the bulk materials. This ability determines the increasing interest in nanoporous glass and is currently the subject of various studies. In the field of nanotechnology, especially that investigates several properties of the liquid phase of guest materials, special attention is attracted to the use of CPG for the study of hydrodynamic processes in nanoscale areas commensurate with the distance between the molecules and the spatial scale of the intermolecular forces. CPGs are often used as a substrate in studies of the thermodynamics of confined systems [49], especially liquid-vapor (capillary) equilibria [50] and liquid-liquid equilibria [51]. Physical processes on the nanoscale occur differently than in macroscopic scale, which leads to striking effects, the physical meaning of which is only partially understood: the condition of phase transition is modified, the viscosity of the liquid is changed and other interesting effects. More can be taken from the review article [4]

The starting material for the preparation of CPG is a two-phase sodium borosilicate glass, which is shown in Figure 2.8 that illustrates spherical templates with 0.3 - 0.5mm in diameter. The initial glass can have various compositions, for instance: SiO_2 - 70w%, B_2O_3 - 23w% and Na_2O - 7w%. This composition is typical of glass, which is formed by two interpenetrating phases. The first phase is chemically non resistant borate phase. The second one is the chemically stable silica phase.

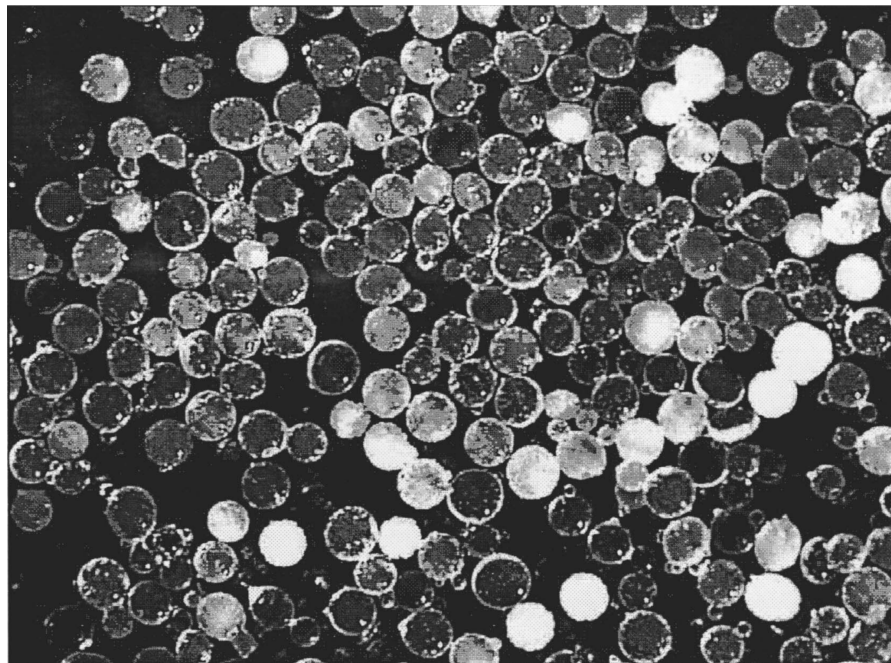


FIGURE 2.8: Spherical sodium borosilicate initial glass (70wt.% SiO₂, 23 wt.% B₂O₃, 7 wt.% Na₂O) 0.3–0.5 mm in diameter (0.3–0.5 mm in diameter) [52]

The borate phase is easily destroyed by the acid solution while the silica phase remains almost unchanged. The production of nanoporous glasses can be divided into several phases. The first phase is melting of the initial glass substrate and forming the desired shape. After that the temperature is hold above the annealing point but bellow the point that would cause physical decomposition. The molten glass is cooled down, the temperature is between 500 and 750 *circ*C, which leads to two continuous phases. The first one is almost pure silica and the second one is a mixture of borosilicate and alkali. The time in which the system is in the liquid state during the two phase stage (so the coarsening can happen) determine the average pore size. The next step is treatment with hot dilute acid solution that removes the borate phase and leaves the silica phase. The end product consists almost of pure silica with some colloidal silica nanoparticles. They are removed with a treatment with NaOH and water. More detailed information can be taken from the book written by J. Scheve [53]

Mechanism of formation of porous structure under the given conditions is called **near-critical spinodal decomposition** [54]. So called "spinodal" is a line or surface in the phase diagram which separates the metastable states (phases) of the unstable states. Quenching of a mixture of two liquids that are near their critical composition leads to a dynamic phase separation [55]. A forming of the two phases takes place. This is a highly connected network structure, its spacial

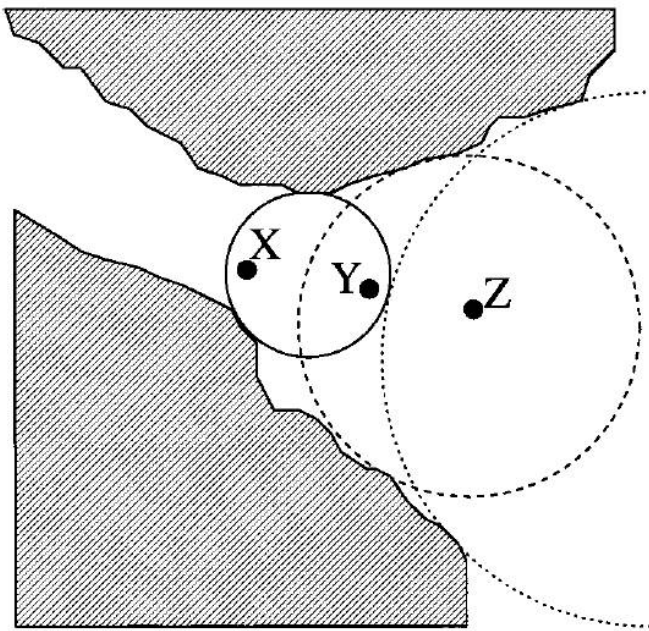


FIGURE 2.9: A model for the pore size distribution inside porous glass. Point x can be covered with the smallest circle, point y is covered by the smallest and midsize circles, and z can be covered with all three. The largest covering circle for every point in the void space is helps to determine the pore volume and pore radius. Taken from [59]

dimension growth in time according to a power law.

Using different experimental methods, such as positron annihilation lifetime spectroscopy (PALS) [56] or small-angle scattering [57] or gas absorption chromatography [58], one can identify several basic properties of porous glasses. The first is the average size of the pores, also called the **average diameter** in case of spherical approximation of the void. It should be noted that the pore size can be specified only in the averaged value, since the production process leads to a rather wide distribution of this quantity around the average value. Computer simulations, such as shown in this article [59] provide insight into the nature of the distribution of diameter values. A model for the pore size distribution inside porous glass is illustrated in Figure 2.9. This Figure shows a 2D model of an area of porous glass that can be covered with three circles with different diameters. Based on this model one can identify two parameters that characterize the size of the pores - the average pore diameter that is calculated by summing up all diameters, determined by a circle approximation and divided by the amount of the circles and the most probable diameter, which is the value (or better to say a short value range) that occurs most often. The second feature is the **porosity**. This value characterizes the sample volume that is not occupied with silica. This value determines the

absorption capacity of porous glass. Another feature is the **specific pore surface**. It characterizes the overall surface normalized to the weight or volume. Last important feature is the spectral transmittance of radiation.

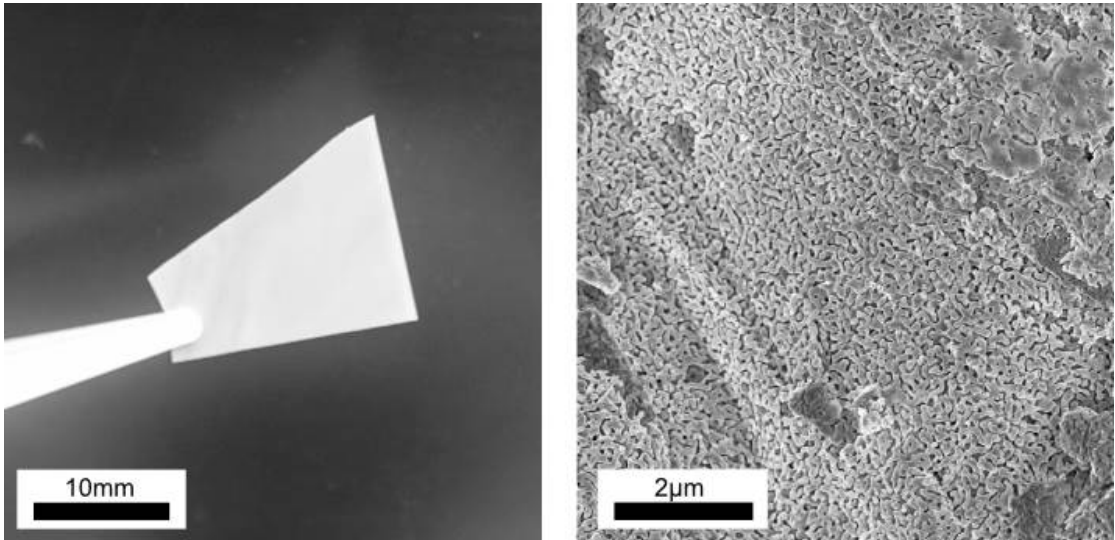


FIGURE 2.10: (left) picture of typical CPG membrane, the colour is white due to the large average pore diameter which is 110 nm (right) SEM picture of the surface of CPG membrane with 110 nm pore diameter.

Figure 2.10 shows a typical CPG membrane with 110 nm pore diameter and its surface under the SEM.

The sample with an average pore size up to 26 nm have been chosen because of their transparency to visible laser radiation. Samples with the average pore size more than 26 nanometers are opaque. This effect can be explained by Mie scattering. That is the reason, why CPG membranes with pore diameter close to 100 nm are not usable for optical experiments. The pore walls that play the role of the colloidal particles are so thick that the Mie scattering leads to an opaqueness of the sample.

A scanning electron microscopy study has been performed in order to understand the outer and inner morphology of the CPG membranes that have been used as host systems for the non destructive experiments performed in the framework if this thesis(Figure 2.12). There are two hierarchically placed structures that can be seen on a different level of magnitude. The first structure has dimensions of micrometer scale, which is the surface roughness. The irregularities that occur during production, storage and cutting the samples are clearly visible on Figure 2.12 a, b and c. This surface roughness does not depend on any specific feature of the sample because at this scale CPGs can be considered as bulk object. The

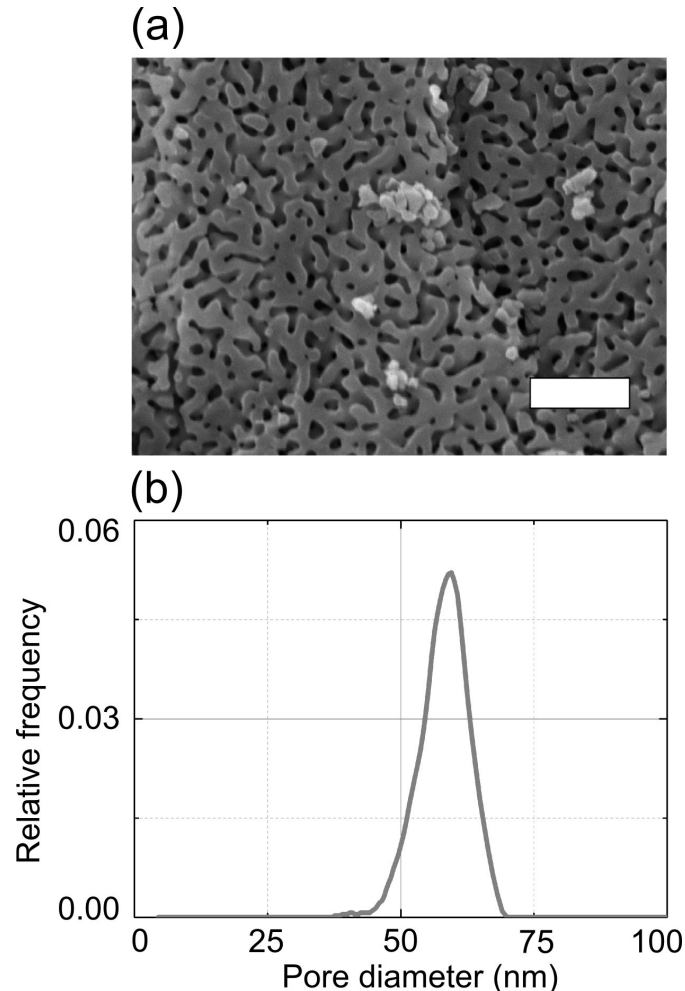


FIGURE 2.11: CPG membrane used for the TGA/CLSM experiments. a) the SEM picture of CPG with 57 nm average pore diameter (the scale bar corresponds to 200 nm) b) the frequency density

second structure has a size on the nanometer scale and is decisive for the porous glass. One can see it at higher magnification (Figure 2.12 d, e and f). The porous structure is formed by the interlacing of glass walls. As a result, empty spaces are formed with certain mean volume (or diameter in case of spherical approximation).

2.3.2 CPG membranes used for evaporation dynamics measurements

Controlled porous glass with pore diameter about 60 nm (see Figure 2.11) was used as host membranes.

Pore size distributions, porosities and specific surface areas were determined by mercury intrusion using Pascal 140 and 440 devices from Porotec (Thermo Finnigan). Prior to the measurements, the CPG membranes were dried at 120 °C for 8 h and degassed for 20 minutes. It was decided to control pore size distribution with the help of graphical analysis. For this purpose, images of both types of membranes were analysed for the average pore size. The results of this analysis can be seen on Figure 2.11 . The average pore size of CPG membrane used in the experiments is 57 nm.

2.3.3 CPG membranes used for the BLS experiments

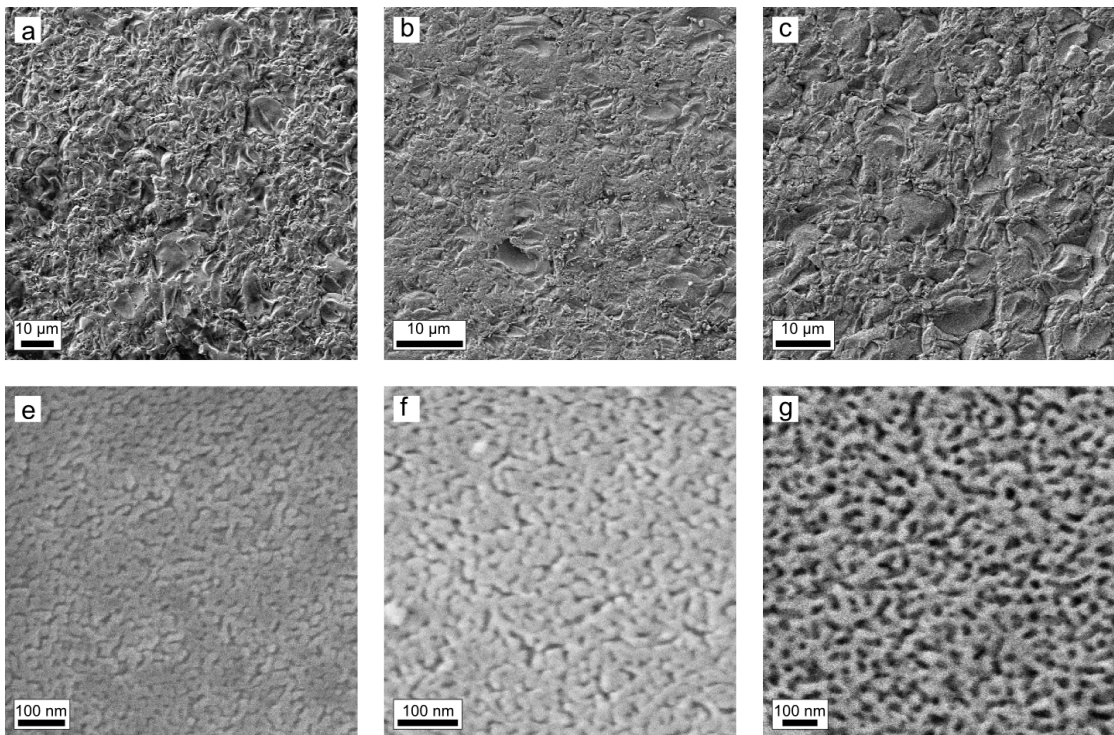


FIGURE 2.12: SEM pictures of 2 nm (a,d) , 9 nm (b,e) and 26 nm (c,f) CPG membranes that were used in the framework of this thesis. The top row shows the macroscopic roughness of each sample, the bottom row shows the porous structure.

Pore size distributions, porosities and specific surface areas were determined by nitrogen gas nitrogen physisorption using Quantachrome ASiQwin device. Prior to the measurements, the CPG membranes were dried at 120 °C for 8 h and degassed for 20 minutes. The scanning electron microscopy (SEM) images of the CPG membranes displayed in Figure were acquired with a Zeiss Auriga Scanning Electron Microscope using in-lens secondary electron detection at an acceleration

TABLE 2.1: Morphological properties of investigated samples. The pore size, the porosity and the specific area was determined by the nitrogen physisorption. The density was calculated after weighting the samples and measuring their dimensions.

Pore Size (nm)	Density ($\frac{g}{cm^3}$)	Porosity (%)	Specific Surface Area ($\frac{cm^2}{g}$)
2	2.098	21.7	247
9	1.548	38	161
26	1.081	51.7	73

voltage of 5.00 kV.

Chapter 3

Experimental methods

3.1 Confocal laser scanning microscopy (CLSM)

3.1.1 General information

Confocal fluorescence microscopy differs from the conventional fluorescence microscopy by significantly improved resolution along the z-axis [60]. This is achieved by using the principle of confocal fluorescence filtering emitted by the sample [61]. In standard configuration, a light source that excites fluorescence is a mercury [62] or xenon lamp [63]. The modern approach is to use a laser source. Advantages of lasers are obvious - monochromaticity and small divergence [64]. Monochromaticity of light enables to expand the spectral range of recorded fluorescence and improve the rejection of light scattering at the excitation wavelength. Small divergence facilitates more efficient operation of the microscope optical system, reduces the number of reflections, improves the accuracy of focusing the beam of light and reduces the volume in which the light can be focused on the sample. The laser beam is put on the sample using a selective mirror. The schematic construction of a CLSM setup that was used for the experiments conducted in this thesis is shown in Figure 3.1.

Laser beam does not illuminate the whole field of view on the sample and is focused only to a single point. Fluorescence emission excited by the laser is going to same objective. A selective mirror reflects laser light scattered by the sample, letting through only the fluorescence signal. Fluorescence that is emitted by layers above and beyond the focal point is unfortunately being registered together with

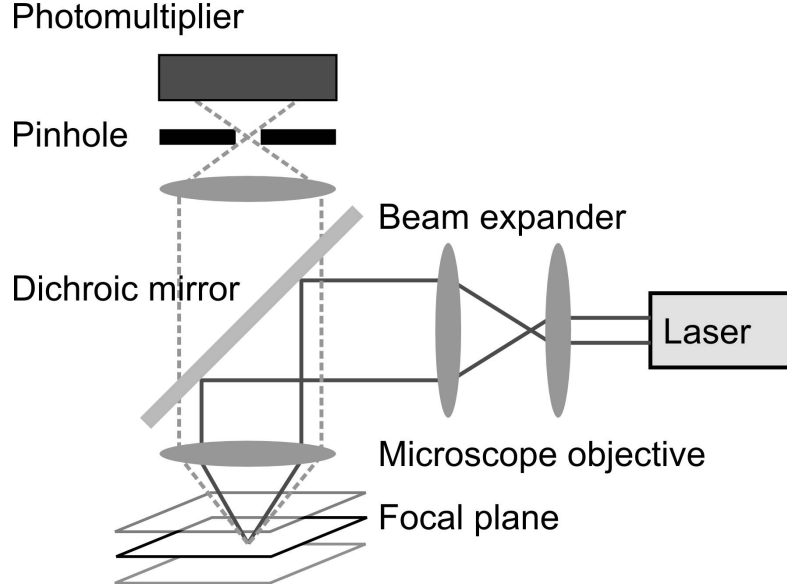


FIGURE 3.1: Schematic construction of a confocal laser scanning microscope.

a main signal which reduces the resolution of the optical system. To improve resolution a confocal aperture is used [65] which is placed in the conjugate focal plane of the objective that is in the plane where the microscope focuses fluorescence collected through the objective lens. Only small amount of fluorescence photons passes through the aperture - those that are excited in the immediate vicinity of the laser spot under the objective. Fluorescence above and beyond focal area is being defocused on the confocal aperture and is not allowed to the photo electrical multiplier. The diameter D of the aperture can be varied. This changes the thickness of the optical layer ∂Z near the focus of the objective from which the signal is measured. The ∂Z can be approximated using following equation([60]):

$$\partial Z = \left(\frac{0.88 \cdot \lambda_{fl}}{n - (n^2 - A^2)^{0.5}} + 2 \cdot n^2 \cdot \frac{(\frac{D}{\Gamma})^2}{A^2} \right)^{0.5}$$

with λ_{fl} - the wavelength of emitted fluorescence, A - numerical aperture of the objective, n - the diffraction number of the medium between the objective and the cover-slip of the sample, Γ - magnification of the optical system of the microscope between the objective and the focal plane conjugate to the focal plane, in which confocal aperture is located.

The higher is numerical aperture of the objective, the smaller is ∂Z . Immersion objectives have the biggest numerical aperture that is why they are widely used in the high resolution CLSM. Reduction of D also lowers the value of ∂Z but it also leads to an increase of the the fluorescence intensity that is collected on the

photomultiplier. The positions of the absorption and emission maxima are very unfavourable in biological samples. It is therefore necessary to find a compromise between the diameter of the aperture and signal / noise ratio in confocal images. In the study of strongly fluorescent systems, such as artificially dyed with synthetic dyes molecules, this problem does not arise.

The CLSM method was used in the framework of this thesis mainly for the detection of the fluorescence signal in the studied host systems. The equipment used allows the detection of both static images and the dynamics of distribution of fluorophores in the X-Y and the X-Z plain. In addition, the method of confocal microscopy is the launching pad for such experimental techniques as fluorescence lifetime measurement and the fluorescence recovery after photobleaching, which will be discussed below. More can be taken from an overview article [66].

3.1.2 Fluorescence mapping in porous media

Fluorescence mapping is widely used in biology, however this method is mostly applied to observe the dynamics within flat regions in the virtual x-y plane [67]. Direct observation of evaporation or diffusion also implies observing processes along the x-z plane. The stack of these mapping pictures along x-z plane as a function of time is what is called time resolved fluorescence mapping. Indirect observation was made with the help of fluorescent molecules that are dissolved in the corresponding volatile or non volatile liquid. The choice fell on rhodamine 6G in case of volatile liquid like ethanol, since this dye has established itself as a stable at relatively high quantum yields [68], and there is no fluorescence quenching in ethanol at reasonably small concentrations [69]. Thus it can be assumed that if in the process of evaporation fluorescence is observed in the test volume, the dye molecules are dissolved in a solvent, and we observe the dynamics of the solvent by monitoring the fluorescence of the dye. In other words - bright regions on a mapping picture indicate the presence of a solvent, dark regions indicate its absence.

For non-volatile liquids, when it comes to the investigation of diffusion, a dye-labelled (perylene) polymer is used. A schematic arrangement of the key elements of the experiment shown in Figure 3.2. The main elements of the investigated system are:

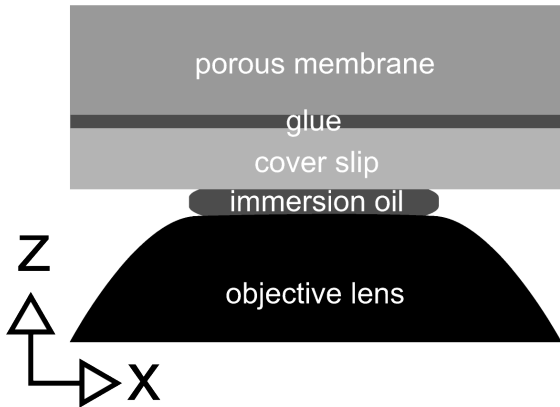


FIGURE 3.2: Schematic representation of the elements included to the investigation with confocal microscopy.

- *A piece of porous membrane* that is sufficiently small to be placed on a glass slide
- The porous membrane is fixed on a glass slide with *small amount of hot glue* that does not fluoresce in the same interval as R6G or perylene.
- *Transparent round cover slip* that is fixed on an objective.
- *Immersion oil* is used to average the refractive index between the objective glass and the glass slide.

Each scan in the $x - z$ plane covers certain distance in (usually not more than 250 μm) z direction and certain distance (also not more than 250 μm , which is the limitation of controlling piezo) in the x direction. The choice of $x - z$ representation is obvious - evaporation dynamics is a process that should be observed in the parallel direction to the normal axis of a setup, since the air phase leaves the system mainly from the top.

3.1.3 Experimental setup

For the acquisition of fluorescence intensity an Olympus LSM FV1000 confocal laser scanning microscope was used equipped with a He Ne laser (excitation wavelength 515 nm) and with a 60x oil immersion objective. This confocal laser scanning microscope set-up consists of a fully motorized microscope, the CLSM unit FV1000 from Olympus and a the compact Lifetime and FCS upgrade kit from Picoquant to measure fluorescence lifetimes using two picoseconds pulsed laser

diodes and single photon Avalanche detectors. Regarding the humidity standard conditions were accepted.

3.2 Time resolved 3D orientation spectroscopy

3.2.1 General information

Time resolved 3D orientation spectroscopy is experimental method that allows to determine the angular distribution of dipole moments of fluorescing molecules. Due to the defined orientation of the absorption/emission dipole with respect to the molecular frame, three-dimensional (3D) orientation resolved single-molecule detection (SMD) in principle allows for determination of molecular orientations and thus of conformational dynamics in macromolecules ([70], p1). Figure 3.3 shows a schematic arrangement of the elements used in the construction of the

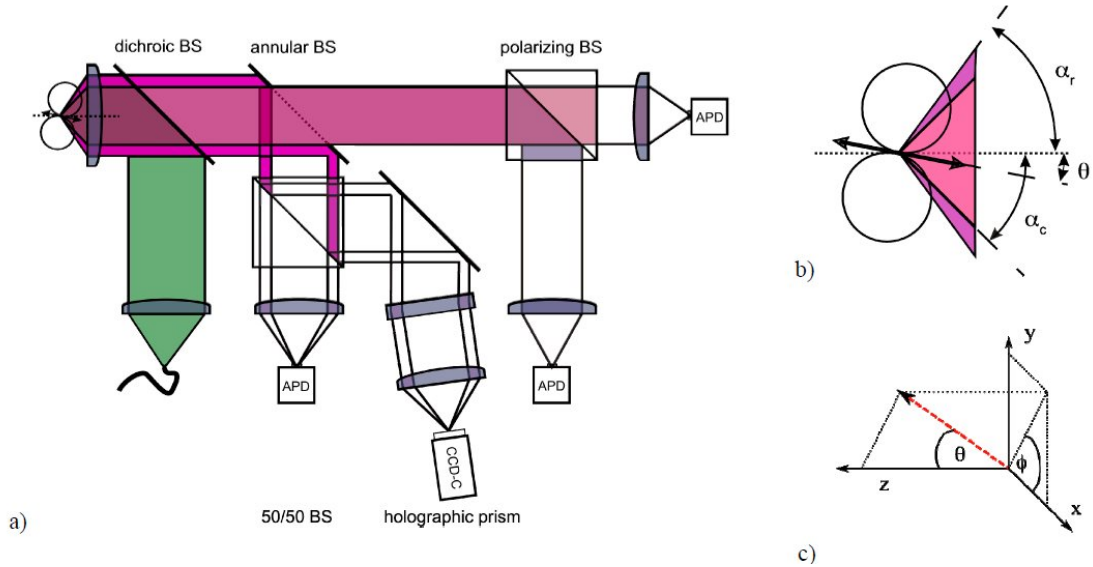


FIGURE 3.3: "Outline of the excitation/detection scheme based on a confocal microscope. After the dichroic beam splitter, the annular and polarizing beam splitters are used to detect three orientation-dependent components of fluorescence dipole emission from single molecules. Furthermore, a 50/50 beam splitter is introduced in the rim intensity pathway for the measurement of the emission spectra. (b) Sketch of a dipole located in the focus indicating the angles used in the text, the polar angle Θ with respect to the optical axis z , the cutoff angle α_c given by the annular beam splitter, and the rim angle α_r given by the numerical aperture of the used microscope objective. (c) Used coordinate system. Optical axis is set to z , while the x - y -plane represents the confocal plane. The red arrow indicates the orientation of the dipole." Description and Figure taken from [70]

experimental apparatus. In the framework of conducted experiments this method was used to determine the spacial and angular distribution of dye molecules inside porous alumina. This method in its actual form does not allow to determine the exact angle, instead it is possible to divide the angles into two classes - the outer and inner angle. Thus, the only useful information is not a static angle distribution, but a dynamic change of the angles during the observation. The direct use of this method and analysis of the results is described in Chapter 4.

3.2.2 Experimental setup

The experiments were performed on a home-built scanning confocal optical microscope. The light of a 470 nm pulsed laser diode (repetition rate of 20 MHz, LDH-P-C-470, PicoQuant, Berlin, Germany) was fed through a polarization conserving optical fiber (SMC-400-3, Schaefter and Kirchhoff, Hamburg, Germany), collimated by an apochromatic microscope objective (UplanApo 4x/0.16, Olympus, Tokyo, Japan) and directed by a dichroic mirror (Z488RDC, Chroma Technology Corporation, Bellows Falls, US) into the back aperture of the oil-immersion microscope objective (100x Plan Apochromat, NIKON, Melville, NY) with a numerical aperture of 1.4, corresponding to a detection cone featuring an aperture angle of $\alpha_{r,oil} = 67^\circ$. A quarter and a half wave plate in front of the optical fiber enables complete control of the polarization state of the excitation light, which was set to circular polarization throughout all experiments. The fluorescence light was collected by the same objective and passed the dichroic mirror as well as a 500 nm long pass filter (HQ500LP, Chroma Technology Corporation) to block the backscattered and -reflected laser light (description of the experimental setup taken from [70]).

3.3 Brillouin Light Scattering Spectroscopy

3.3.1 General information

Brillouin light scattering is a scattering process based on adiabatic density fluctuations of condensed matter [71]. Adiabatic density fluctuations can be represented

as consequence of an interference of propagating elastic waves along all possible directions with different frequencies with random phases and amplitudes. A plane light wave that propagates in such a medium is scattered in all directions due to these elastic waves. The theory of elasticity of solids is described in detail in the work of Landau and Lifshitz [72]. This theory is used to describe the scattering of laser light [73] in solid bodies. The electromagnetic field in a non homogenous medium with permittivity $\epsilon = \epsilon_0 + \delta\epsilon$ can be represented in following form [74]:

$$\vec{E} = \vec{E}_0 + \vec{E}' \quad (3.1)$$

$$\vec{H} = \vec{H}_0 + \vec{H}' \quad (3.2)$$

with \vec{E}_0, \vec{H}_0 - field components of the incident light and \vec{E}', \vec{H}' - field components of the scattered light.

In the case of a weak inhomogeneity of a medium it is possible to write following equations:

$$\nabla \times \vec{H}' - \frac{\epsilon_0}{c} \frac{\partial \vec{E}'}{\partial t} = \frac{4\pi}{c} \frac{\partial}{\partial t} \delta \vec{P} \quad (3.3)$$

$$\nabla \cdot \epsilon \vec{E}' = -4\pi \nabla \cdot \delta \vec{P} \quad (3.4)$$

$$\nabla \times \vec{E}' - \frac{1}{c} \frac{\partial \vec{H}'}{\partial t} = 0 \quad (3.5)$$

$$\nabla \cdot \vec{H}' = 0 \quad (3.6)$$

with $\delta P = \frac{\delta\epsilon}{4\pi} \cdot \vec{E}_0$

These equations show that the medium can be considered as homogenous with the permittivity ϵ_0 . The influence of the existing inhomogeneities is equivalent to the presence of additional sources of electromagnetic waves. Each volume element dV of the medium is a source for additional radiation as a Hertz-dipole with dipole moment $\delta \vec{P} dV$. We denote this additional radiation as scattered light.

The equations 3.3, 3.4, 3.5 and 3.6 are linear and homogenous regarding the fields \vec{E}' , \vec{H}' and $\delta\epsilon$. Therefore, $\delta\epsilon$ can be represented as a sum of smaller elements:

$$\delta\epsilon = \sum \delta_i \epsilon \quad (3.7)$$

This representation means that the scattered electromagnetic radiation, in the case of linear approximation, can be obtained as by a simple superposition of the fields that are scattered by the local inhomogeneities $\delta_i \epsilon$.

Thus, we can first consider the case with only one irregularity $\delta_i \epsilon$ where $\delta\epsilon$ is a simple superposition of the entire set of $\delta_i \epsilon$.

Let us first deal with a case, where $\delta\epsilon$ consists of only one elements:

$$\delta\epsilon = a \cdot \exp(-i\vec{K}\vec{r}) \quad (3.8)$$

with a , \vec{K} - constants.

The incoming wave is a plane wave with:

$$\vec{E}_0 = \vec{A} \exp(i(\omega t - \vec{k}\vec{r})) \quad (3.9)$$

$$\vec{H}_0 = \vec{B} \exp(i(\omega t - \vec{k}\vec{r})) \quad (3.10)$$

We divide the medium in equidistant planes that are perpendicular to the vector \vec{K} . The distance between planes is:

$$\Lambda = \frac{2\pi}{K} \quad (3.11)$$

Figure 3.4 illustrates this concept. The medium is divided into four layers with a distance Λ , the wave-vector of the incident light is \vec{k} and the wave-vector of the scattered light is \vec{k}' . The angle Θ is a scattering angle between the incident and scattered field.

The phases of the secondary sources of the equidistant planes are the same. If the inhomogeneity would be only in the layer 1, than the incident wave would experience a partial reflection from this layer and would partially pass on. Having the inhomogeneity only in the second layer would lead to another reflected wave

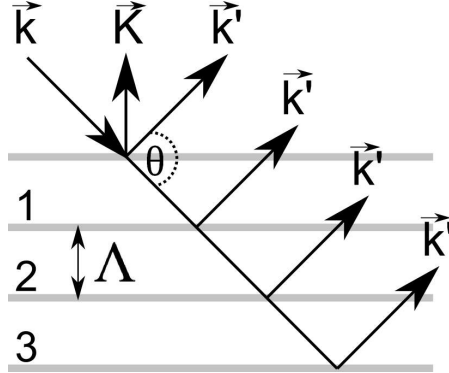


FIGURE 3.4: A schematic representation of a light scattering in a medium divided into four layers with a layer distance Λ .

with the same amplitude but a different phase. The same applies for the layer 3 and so on. In the linear approximation the scattered field is a simple superposition of the reflected waves.

The Bragg condition must apply so the waves are enhanced:

$$2\Lambda \cdot \sin \frac{\Theta}{2} = m\lambda \quad (3.12)$$

where Θ is a scattering angle and m - the order the diffraction spectrum.

All plane waves reflected on different layers create an additional wave:

$$\vec{E}' = \vec{A}' \exp(i(\omega t - \vec{k}\vec{r})) \quad (3.13)$$

where \vec{k}' defines the propagation direction of the scattered wave. And additional polarization of the medium can be expressed as:

$$\delta\vec{P} = \frac{\vec{E}_o}{4\pi} \delta\epsilon = \frac{a\vec{A}}{4\pi} \exp(i(\omega t - (\vec{k} + \vec{K})\vec{r})) \quad (3.14)$$

Substituting these expressions into the equation 3.4 one can easily get an expression $\vec{k}' - \vec{k} = \vec{K}$ that leads to:

$$2\Lambda \cdot \sin\left(\frac{\Theta}{2}\right) = \lambda \quad (3.15)$$

The mechanism of light scattering on the inhomogeneities in the permittivity is similar to the mechanism of x-ray scattering on the crystal lattice.

Up to now we only considered the spatial change of the function $\delta\epsilon$, but not

the temporal change. Taking the temporal change into account leads to a new important factor in the light scattering process.

Let ϵ be only the function of the density ρ . One can write in the linear approximation:

$$\Delta\epsilon = \left(\frac{d\epsilon}{d\rho} \Delta\rho \right) \quad (3.16)$$

Every fluctuation in the density of a medium is a source of acoustic waves. $\Delta\rho$ can be expanded in Fourier series and one should take only those acoustic waves that are important for wave scattering in an observed region. Every inhomogeneity of a medium can be represented as a superposition of plane sinus inhomogeneities in different directions, according to the Fourier theorem. The sinusoidal inhomogeneities scatter the light independently. Assuming the fixed direction of scattered radiation, not all sinusoidal irregularities are effective, but only those, which wave vector \vec{k} is directed along the bisector of an angle additional to Θ up to 180° . Now, we can define the acoustical frequency Ω that corresponds to the wave vector \vec{K} . There are two possible directions of the acoustic wave distribution: along \vec{K} and against \vec{K} . The inhomogeneity $\delta\epsilon$ that causes the light scattering in the observed direction can be presented as a sum:

$$\delta\epsilon = \delta\epsilon_1 + \delta\epsilon_2 \quad (3.17)$$

where $\delta\epsilon_1$ and $\delta\epsilon_2$ are plain acoustic waves:

$$\delta\epsilon_1 = a_1 \exp(i(\Omega t - \vec{K} \cdot \vec{r})) \quad (3.18)$$

$$\delta\epsilon_2 = a_2 \exp(-i(\Omega t + \vec{K} \cdot \vec{r})) \quad (3.19)$$

The corresponding vectors of additional medium polarization are:

$$\delta\vec{P}_1 = \frac{\vec{E}_0}{4\pi} \delta\epsilon_1 = \frac{a_1 \vec{A}}{4\pi} \exp(i((\omega + \Omega)t - (\vec{k}\vec{K}) \cdot \vec{r})) \quad (3.20)$$

$$\delta\vec{P}_2 = \frac{a_2 \vec{A}}{4\pi} \exp(i((\omega - \Omega)t - (\vec{k}\vec{K}) \cdot \vec{r})) \quad (3.21)$$

Thus the source of a scattered light and therefore the scattered light itself modulate in time with frequencies $\omega + \Omega$ and $\omega - \Omega$. That is the modulation of electromagnetic radiation by an acoustic wave.

In the spectrum of scattered light one should observe a doublet with those frequencies. This phenomenon is called the fine structure of a Rayleigh scattering or the Brillouin scattering. The frequency shift is:

$$\Omega = K \cdot v = \frac{2\pi}{\Lambda} \cdot v \quad (3.22)$$

with v - sound velocity in a medium, Λ - sound wavelength. Based on the equation 3.15 one can write:

$$\Omega = \frac{4\pi v}{\lambda} \cdot \sin \frac{\Theta}{2} = 2\omega n \frac{v}{c} \cdot \sin \frac{\Theta}{2} \quad (3.23)$$

with c - speed of light in vacuum, n - refraction index of a medium.

There are several approaches how to interpret the presence of the frequency shift. The first approach is to assume that this effect is caused by a Doppler effect: when the acoustic wave is propagating along the light wave, an increase in a frequency occurs.

Relative shift of the photon frequency in BLS spectroscopy ($10^8 - 10^{11}$ Hz) is very small compared to the initial light frequency of 10^{14} Hz (six orders of magnitude). Thus an extremely precise method of measurement is required, which in this case is Fabri Perot interferometer. We use a system of two Fabri-Perot interferometers with multipass.

Fabry-Perot interferometer is a spectral device with high resolution and is widely used in various applications. It is mainly used for investigating the fine structure of spectral lines and is also an important component of almost every laser, where it plays a role of an optical resonator.

Fabry-Perot interferometer ([75], [76], [77] and [78]) consists of two glass or quartz plates P_1 and P_2 . The inner surface of those plates is highly polished with a accuracy of $10^{-2}\lambda$ and are installed plane parallel to each other. The polished inner surface is covered with a highly reflective material such as Ag , Al (reflectivity is about 0.9) but also modern artificial layers which reflectivity as above 0.99.

This type of interferometer can be considered as a plane parallel air plate on which occurs multiple reflections and interference of light. The interference pattern that is observed in the focal plane of a lens L consists of concentric circles with constant inclination.

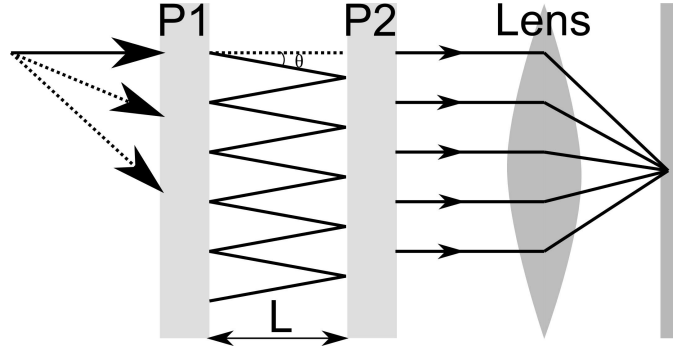


FIGURE 3.5: Two parallel mirrors with reflectivity R and distance L . The distance can be varied.

Two parallel beams that are propagating between the mirrors of the interferometer at an angle Θ have the path difference determined by the expression:

$$\Delta = 2L\cos\Theta \quad (3.24)$$

where L is a distance between mirrors. The equation 3.24 is a special case of a well known equation for a plane parallel plate with a refractive index n :

$$\Delta = 2Lncos\psi \quad (3.25)$$

where ψ is the refraction angle of the light beam inside the plate.

Let r and t be the coefficients of reflection and transmission of the interferometer mirrors. The amplitude of a falling wave is A_0 . Then the amplitude of the first beam that passed through the interferometer is A_0t , the second beam has the amplitude A_0tr , the third A_0tr^2 and so on. In the complex representation the amplitudes of these beams build an infinite geometrical progression:

$$A_0t, A_0tr e^{ik\Delta}, A_0tr^2 e^{i2k\Delta}, A_0tr^3 e^{i3k\Delta}, \dots, \quad (3.26)$$

where $k = \frac{2\pi}{\lambda}$. Ratio of the progression equals $re^{ik\Delta}$. In the focal area of a lens all beams are summed up. The resulting amplitude equals:

$$A = \frac{A_0t}{1 - re^{ik\Delta}} \quad (3.27)$$

The intensity of the passed light beam is than:

$$I = AA* = \frac{I_0 t^2}{1 + r^2 - 2rcos(k\Delta)} \quad (3.28)$$

with $I_0 = A^2_0$ - the intensity of the incident light beam.

When the reflection coefficient is large enough ($r \geq 0.9$) the interference pattern consists of thin bright circles, divided by large dark intervals. This is a consequence of multiple beam interference. When the reflectivity is small ($r \leq 0.1$) one can observe a poorly visible alternation of maxima and minima, which is characteristic for the two beam interference pattern that strongly differ in the amplitude.

Let us investigate the diameters of the diffraction pattern assuming for simplicity that the angle Θ is quite small. We take to interference rings which have the order of interference Δ/Λ - m_i and m_j . The bright circle of the order m is build when the following relation is true:

$$\Delta = 2L \cos(\Theta) = m\lambda \quad (3.29)$$

where m is an integer number. The order of interference increases with interference rings with smaller diameter which mean smaller Θ . Assuming small Θ we can write:

$$2L \left(1 - \frac{\Theta_i^2}{2} \right) = m_i \lambda \quad (3.30)$$

$$2L \left(1 - \frac{\Theta_j^2}{2} \right) = m_j \lambda \quad (3.31)$$

We subtract the second equation from the first one and assume that the order of interference has a difference of 1 between two neighboring interference rings. That one can write:

$$L(\Theta_j^2 - \Theta_i^2) = (m_i - m_j)\lambda = (j - i)\lambda \quad (3.32)$$

The numbers of interference patterns i and j are counted from the center.

The diameter D of the interference ring in the focal area of the lens is related to its focal distance f due to following relation:

$$D = 2f\Theta \quad (3.33)$$

Therefore one can write:

$$\lambda = \frac{L}{4f^2} \frac{D_j^2 - D_i^2}{j - i} \quad (3.34)$$

This equation is used for measuring the wavelength of light with Fabri-Perot interferometer or for elucidating the constant L with known value of λ .

Lets assume that we observe a system of two circles for two spectral lines that are very close to each other: λ and $\lambda + d\lambda$. Differentiating the equation 3.29 for small Θ we can write:

$$-2L\Theta d\Theta = md\lambda \quad (3.35)$$

that leads to the following expression:

$$d\lambda = -\frac{2L\Theta}{m}d\Theta \approx -\lambda\Theta d\Theta = -\frac{\lambda\bar{D}}{4f^2}dD \quad (3.36)$$

\bar{D} is the mean diameter of the interference rings, dD is the difference of interference rings diameters for spectral lines with wavelength λ and $\lambda + d\lambda$ for the same order of interference.

There are three important factors that define the usability of interferometer for the given application - the dispersion, the dispersion region and spectral resolution. The dispersion of the interferometer or the linear dispersion $D*$ is the relation of the distance dl between spectral lines in the plane of a spectrum and the difference $d\lambda$ of those lines. The linear dispersion can be easily transformed into angular dispersion:

$$D* = f \frac{d\Theta}{d\lambda} = \frac{dD}{2d\lambda} = \frac{2f^2}{\lambda D} \quad (3.37)$$

High dispersion value is the main advantage of the Fabri-Perot interferometer.

The dispersion region of a spectral device is a maximal wavelength interval $\Delta\lambda$ where there is no overlay of interference patterns of adjacent order. The width of this area is defined by the overlapping condition of the ring with the order $m + 1$ for the wavelength λ with the ring of the order m with the wavelength $\lambda + \Delta\lambda$:

$$m(\lambda + \Delta\lambda) = (m + 1)\lambda \quad (3.38)$$

which leads to:

$$\Delta\lambda = \frac{\lambda}{m} \approx \frac{\lambda^2}{2L} \quad (3.39)$$

The order of interference is very high for Fabry Perot interferometer. That means that the spectral interval that can be analysed with this kind of interferometer is quite small. One possible solution is to place a colour filter or any other spectral device that cuts out the spectral area that do not exceed $\Delta\lambda$.

The spectral resolution of any spectral device is defined by the following equation:

$$R = \frac{\lambda}{\delta\lambda} \quad (3.40)$$

with $\delta\lambda$ is a minimal difference of wavelengths that is visible with a spectral device near the wavelength λ . A conditional criterion defined by Rayleigh is used to define $\delta\lambda$ and it is based on a distance between two lines - they are visible if their maxima are spaced apart by half of their width. Defining the width of the line on the level full width on half maximum one can obtain following equation:

$$R \approx \frac{2\pi L \sqrt{r}}{\lambda(1-r)} \quad (3.41)$$

The definition of Q -factor or the quality factor of an oscillating system as analogous to the resolution factor R of the spectral device:

$$Q = \frac{\omega}{\delta\omega}; R = \frac{\lambda}{\delta\lambda} = \frac{\omega}{\delta\omega} \quad (3.42)$$

It is generally known that

$$Q = 2\pi \frac{W}{\Delta W_T} \quad (3.43)$$

with W - stored energy of the oscillating system, ΔW_T energy loss during the period of oscillation.

We shall find the value Q for Fabri-Perot interferometer considering this as an optical resonator device. For this purpose we observe the scattering of optical energy in an excited resonator.

Consider the moment of time when some electromagnetic energy W is stored between two mirrors of interferometer. The radiation inside the interferometer has the character of two waves traveling in opposite directions. Due to the limited transparency of the mirrors the energy of the waves is attenuated $(1-r)$ times during the time $\tau = \frac{L}{c}$. Therefore:

$$\Delta W_\tau = (1-r)W \quad (3.44)$$

And the loss during the time $T = \lambda/c$ is:

$$\Delta W_T = \frac{T}{\tau} \Delta W_\tau = \frac{\lambda(1-r)}{L} W \quad (3.45)$$

Thus we can write the Q -factor as:

$$Q \approx \frac{2\pi L}{\lambda(1-r)} \quad (3.46)$$

One can come to a conclusion that the Q -factor is almost infinite for $r \rightarrow 1$. In the real case the limiting factor is a light scattering due to the inhomogeneities of the mirror surface.

As already mentioned in the text above, the relative shift of the photon frequency in BLS spectroscopy ($10^8 - 10^{11}$ Hz) is very small compared to the initial light frequency of 10^{14} Hz (six orders of magnitude).

As discussed by Still [79], the single pass FP delivers non sufficient contrast for resolving signals with low intensity and in general leads to complicated spectra due to the interference between neighbouring spectra. Sandercock [80] has solved these problems by developing a system that is based on the multi-pass tandem FP.

For adequate resolution of closely spaced spectral lines it is necessary that the mirrors are placed far from each other. In this case, the free spectral range between adjacent interference order is very small. Lines of adjacent orders may overlap. Therefore, a technique is required that allows the sufficient free spectral range with a high resolution. "Two FP's with slightly different FSR are connected in series (tandem). An intelligent use of additional mirrors assures that the light passes each FP several times (multi-pass). In the tandem operation, both FP's must transmit the same wavelength simultaneously by an appropriate scanning technique. Due to the differing FSR's of both individual FP's, always one of the FP's blocks the neighbouring interferences." [79] p.39.

As discussed by Sato [81], the change of optical length ΔL of two interferometers with spacings L_1 and L_2 that are arranged in series and transmit simultaneously is

$$\frac{\Delta L_1}{\Delta L_2} = \frac{L_1}{L_2} \quad (3.47)$$

That would also be the case for the FP interferometer shown in Figure 3.6, the axes are inclined at an angle Θ .

Therefore one can write

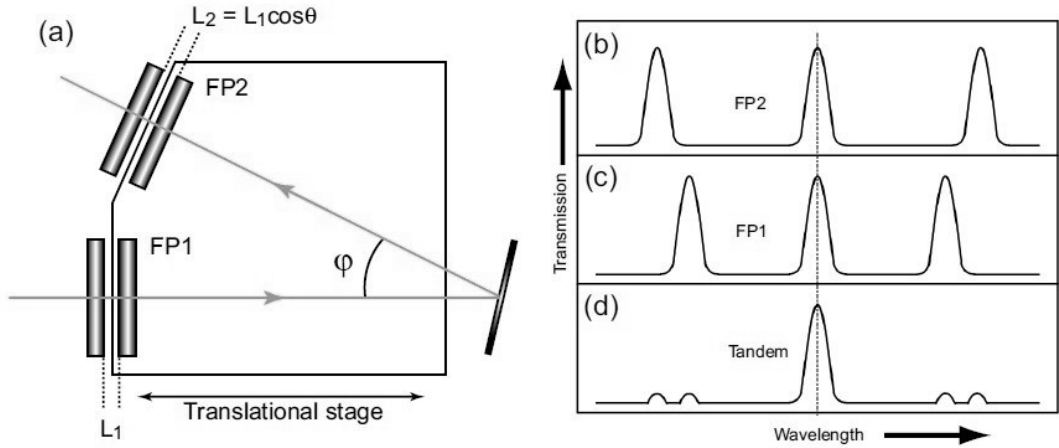


FIGURE 3.6: Tandem interferometer with mechanical coupling of the movable plate. Figure taken from [81]

$$\frac{L_1}{L_2} = \frac{\Delta L_1}{\Delta L_2} = \frac{1}{\cos \phi} \quad (3.48)$$

The wavelength transmitted by two FP arranged in series must satisfy following conditions:

$$L_1 = \frac{1}{2}m_1\lambda \quad (3.49)$$

$$L_2 = \frac{1}{2}m_2\lambda \quad (3.50)$$

for integral values of m_1 and m_2 .

FP1 and FP2 are spaced slightly different as shown in Figure 3.6 therefore they must have different free spectral range. The neighboring transmission peaks do not coincide, which leads to the combined transmission of light that is illustrated in Figure 3.6d.

Since many investigated samples can be considered as films (for instance the CPG membranes), there are two possible scattering geometries - the transmission and reflection geometry, their sketch is shown in Figure 3.7. Therefore, the q-parallel means the Brillouin shifts are measured in transmission mode, q-perpendicular - in reflection mode.

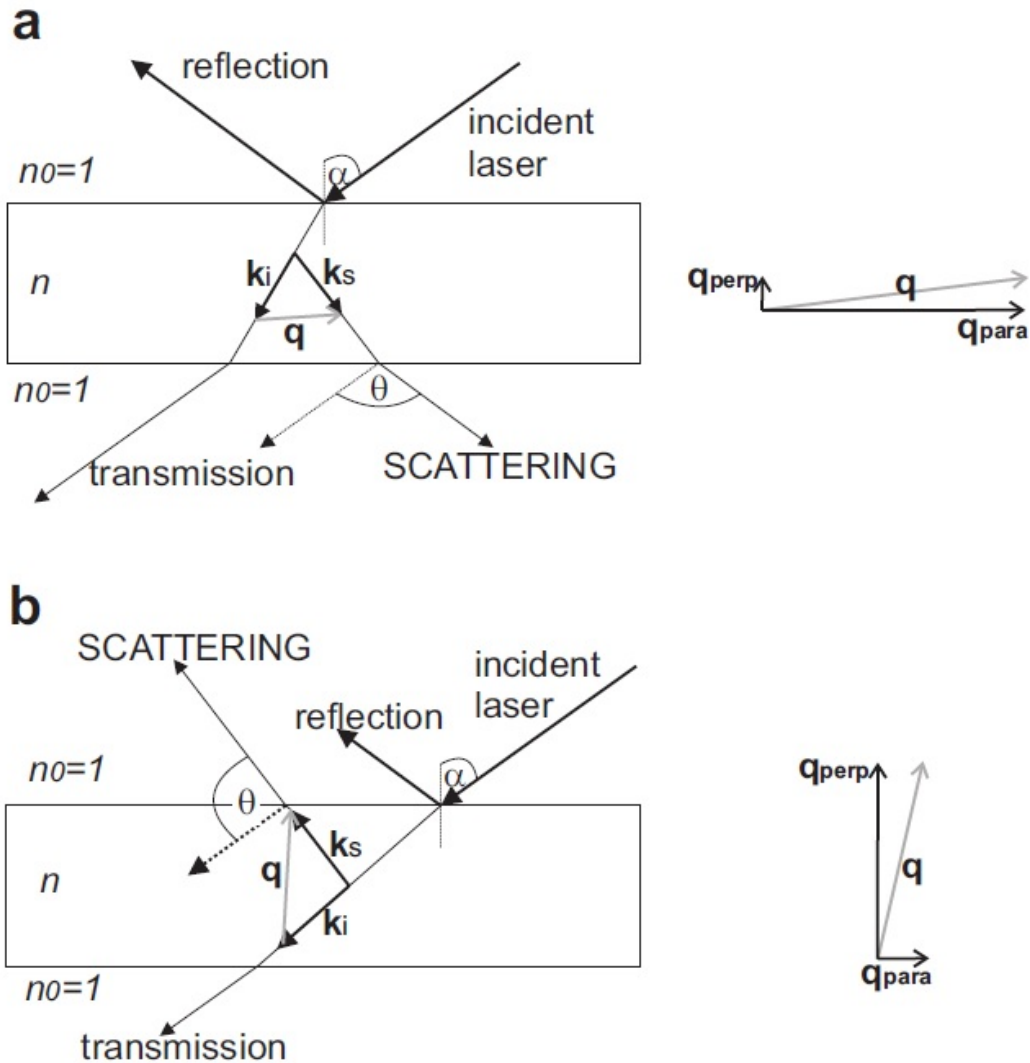


FIGURE 3.7: "‘Principle BLS scattering geometries for a film sample (view atop the scattering plane). a - Transmission geometry b - Reflection geometry. On the right side the vector decomposition for the wave vector q in its components perpendicular (q_{perp}) and parallel to the film plane (q_{para}).’" [79]

The magnitude of the scattered wave-vector q in transmission mode is:

$$q = \frac{4\pi n}{\lambda} \sin \left[\frac{1}{2} \left(\sin^{-1} \left(\frac{1}{n} \sin(\theta - \alpha) \right) + \sin^{-1} \left(\frac{1}{n} \sin \alpha \right) \right) \right] \quad (3.51)$$

where α and θ are given in Figure 3.7a.

There is a special transmission geometry, when q equals q_{para} for $\theta = 2\alpha$:

$$q = q_{para} = \frac{4\pi}{\lambda} \sin \frac{\theta}{2} \quad (3.52)$$

This special geometry is very useful because the refractive index n has not to be taken into account.

For the case, when n has to be figured out, it is possible to use the function for reflection geometry, which is:

$$q = \frac{4\pi n}{\lambda} \cos \left[\frac{1}{2} \left(\sin^{-1} \left(\frac{1}{n} \sin \alpha \right) + \sin^{-1} \left(\frac{1}{n} \sin(\theta + \alpha) \right) \right) \right] \quad (3.53)$$

There is a special case for:

$$\alpha = \frac{180^\circ - \theta}{2} \quad (3.54)$$

In this case the scattering vector is identical to its component perpendicular to the membrane, which means $q = q_{perp}$. This is used to determine the refractive index in further experiments with porous glasses.

Another important parameter is the polarization of incident light. Before passing the sample, the light beam passes a so called Glan polarizer (with an extinction ratio 1E-5). The polarization is vertical (V). That ensures the fully polarized incident light. After passing the sample, the V polarized beam is collected by the aperture and is focused into the tandem Fabry-Perot. A Glan-Thompson analyser with an extinction ratio of 1E-8 selects the polarization of this beam. The polarization can be vertical (V) or horizontal (H). Vertical means it is perpendicular to the scattering plane, horizontal means it is parallel to the scattering plane. The VV configuration measures longitudinal waves, the VH configuration measures transversal waves.

3.3.2 Experimental setup

During the experiments conducted in the framework of this thesis a six pass tandem Fabry-Perot interferometer was used. The optical path of the interferometer is illustrated in Figure 3.8 taken from [79]. Transmission geometry takes place when the light passes through the sample and is scattered from the other side, than the incident light. The reflection geometry takes place, when the light is scattered from the same side as the incident light. The Nd:YAG laser (COHERENT, 100 mW, $\lambda = 532$ nm) was used as the light source. The laser beam, which is vertical (V polarization) relative to the scattering plane adjusted by a polarizer, was focused with a lens to a spot size of about $200 \mu\text{m}$ on the sample. The scattered light

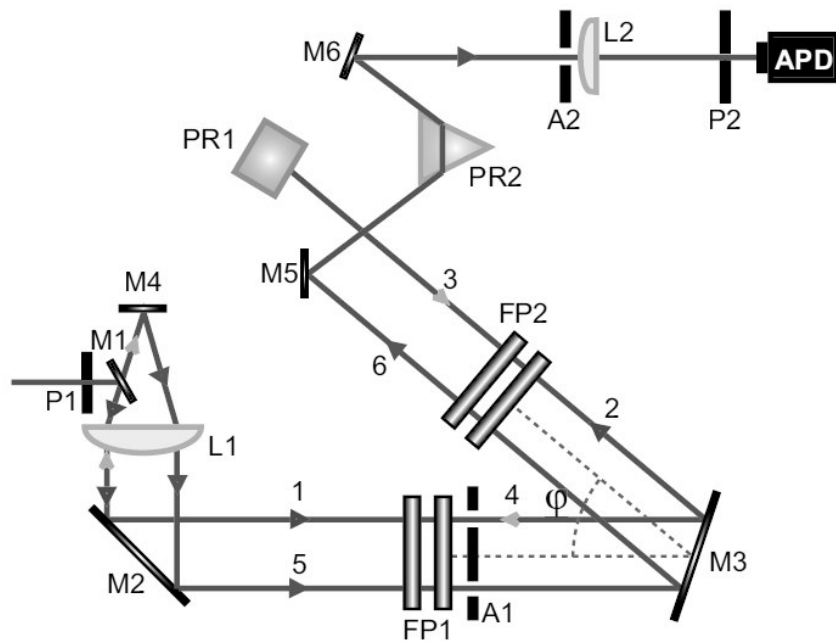


FIGURE 3.8: Schematical representation of six pass Fabri-Perot interferometer used in the experiments. Original picture taken from [81] p.23

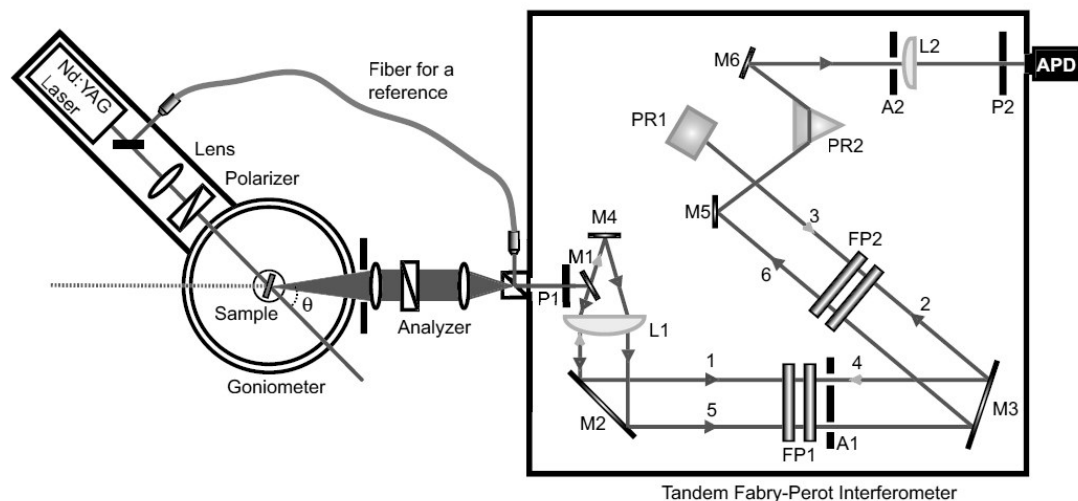


FIGURE 3.9: Schematical representation of the BLS experimental setup. Original picture taken from [81]

was collected and focused by two lens into the pinhole ($P1$) of the Tandem Fabry-Perot interferometer. The plane of polarization of the scattered light, which is either vertical (V polarization) or horizontal (H polarization) relative to the scattering plane, is adjusted with an analyzer. A single-photon Avalanche photodiode (APD) detected the scattered light passing through the Tandem Fabry-Perot interferometer. The scattering angle Θ is changed by rotating the goniometer on which the light source is mounted. Scattering angles from 25° to 150° could be measured.

3.4 Thermal Analysis

3.4.1 General information

3.4.1.1 Differential Scanning Calorimetry (DSC)

Differential scanning calorimetry (DSC) is an experimental method which allows to measure the heat flow that is needed to change the temperature of a test-sample and reference-sample as a function of temperature and/or time. During the experiment the test-sample and reference-sample are maintained at the same temperature. Normally, during the experiment the temperature increases linearly as a function of time, however in the framework of the conducted DSC/TGA experiments the temperature was kept constant. The heat capacity of the reference-sample should be well known. The principle behind this experimental method is that when the studied material experiences a physical change such as phase transitions, more or less heat will need to flow to it than to the reference, so both of them can have the same temperature. Whether less or more heat must flow to the sample depends on whether the process is exothermic or endothermic.

If a solid sample melts there is a need for more heat flowing to the sample to increase its temperature at the same rate as the reference. Differential scanning calorimeters are able to measure the amount of heat absorbed or released by observing the difference in heat flow between the sample and reference. The result of a DSC experiment is a curve of heat flow vs. time or temperature. Only isothermal experiments were conducted in the framework of this thesis, because isothermal conditions are normally used for desorption, vaporization and drying

experiments. Isothermal DSC curves are easier to interpret because the investigated effect can be observed almost in isolation (since other effects are observable at other temperatures). More information can be found in [82].

3.4.1.2 Thermogravimetric analysis (TGA)

Thermogravimetry or Thermogravimetric analysis (TGA) is a method of thermal analysis, wherein the change in mass of the sample is recorded as a function of different parameters. TGA method is based on the observation of the mass of test substance when changing its temperature or while the temperature is constant as a function of time. The result of this analysis are so called TG-curves - the dependence of the mass (or weight changes) form temperature or time. To interpret the results of the TG analysis one requires the processing of TG curves. In particular, the derivative of the TG signal (rate of mass change) represented by a curve, allows to determine the time or temperature at which the weight change occurs most rapidly. Thermal analyzer consists of a precision balance with the crucible (usually platinum), which are placed in a small chamber furnace. In the vicinity of the sample, for example, under the bottom of crucible, a control thermocouple is placed to accurately measure the temperature. Usually one uses a controlled atmosphere [83], for instance argon or controlled air (a controlled mixture of oxygen and nitrogen). To control measuring equipment and readout a computer is used. In the process of analyzing the temperature rises at a constant rate. The change in mass is recorded as a function of temperature. The upper temperature limit is limited only by the capabilities of the device and may reach 1500C or more. High resolution is achieved due to the presence of feedback loops between the weight of the sample and its temperature. Heating slows down as the sample weight change, and thus, the temperature at which the weight changes can be set with high accuracy. Thermogravimetalical analysis has a wide range of applications in the metallurgy, mineralogy, organic and inorganic chemistry, and so on [84], [85], [86] . Some of the many applications of this method are: thermal decomposition of organic, inorganic and multimineral substances, a solid phase reaction, calcining minerals, moisture determination and investigation of the reaction kinetics.

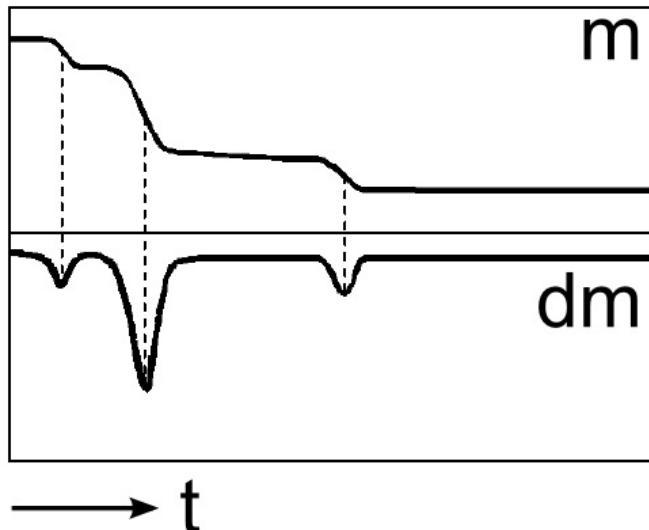


FIGURE 3.10: An example for the measured mass loss and velocity as function of time with thermogravimetical set up.

3.4.2 Experimental setup

Figure 3.11 shows a photography of the simultaneous thermal analyzer NETZSCH STA 449 F3 Jupiter that was used for the combined TGA DSC experiments on evaporation dynamics in porous glasses. Experiments were performed with a Netzsch STA 449C Jupiter device. A piece of a CPG membrane was weighed and then located in an aluminium crucible. $10 \mu L$ of pure ethanol were dropped onto the sample surface using an Eppendorf syringe. The $m(t)$ and $\dot{Q}(t)/m_0$ traces were acquired at a constant temperature of $25^\circ C$ while the samples were purged with a mixture consisting of 20% oxygen and 80% nitrogen at a flow rate of 65 ml/min . The TGA measurements started about 30 s after ethanol deposition as soon as the covering of the TGA device had closed; m_0 corresponded to the sample mass at the start of the TGA measurement.

Comparisons of the initial total amount of ethanol inside the CPG membrane pieces and the progress of mass loss apparent from the $m(t)$ profiles allowed estimating the point of time beyond which the CPG membranes were no longer submerged in ethanol and evaporation of ethanol out of the membrane occurred. The time resolution of the TGA measurements was 100 ms (10 data points per second), the mass resolution 0.0005 mg , the heat flow resolution 0.00243 mW/mg and the enthalpy resolution 0.0005 mJ .



FIGURE 3.11: The simultaneous thermal analyzer NETZSCH STA 449 F3 Jupiter used for the combined TGA DSC experiments on evaporation dynamics in porous glasses.

Chapter 4

Evaporation of volatile guests from hosts with sponge-like continuous pore systems

4.1 Introduction

The evaporation of ethanol, which is the model system for the volatile guest substance, has been investigated inside CPG (Section 2.3.1) membranes that play the role of the solid guest system, using two different experimental methods - confocal fluorescence microscopy (Section 3.1.2) and combined TGA/DSC method (Section 3.4). These methods have been applied that way that the physical structure of the investigated systems has not been damaged, which makes the applied methodology non destructive. In the framework of this thesis it was shown that the evaporation process can be divided into two different modes - the first is the linear evaporation that happens isothermal and the second that is characterized by burst-like jumps that have adiabatic nature. The results of this investigation were published (see Ichilmann et. al. [87]).

Evaporation of the liquid guest phase from the porous host [88] (also called drying) is a key factor in different mechanisms for instance in the sol-gel process that is connected with the drying of gels [89] or during the production of nanoporous polymer membranes [6]. In general, the process of drying can be described as a process of removing the liquid phase from the solids, gases, or other liquid phases [90]. The classic process, in which the liquid phase is removed, is

evaporation. Evaporation is the process of phase transition of a substance from a liquid state to a vapour or gas that occurs on the surface of the substance. The evaporation process is the reverse process of condensation (transition from liquid to vapor state). In the evaporation from the surface of the liquid or solid body fly (detached) particles (molecules, atoms), with their kinetic energy should be sufficient to carry out the work needed to overcome the forces of attraction of other molecules of the liquid. The particles (molecules, atoms) are emitted (detached) at the time of evaporation from the surface of the liquid or solid body, their kinetic energy should be sufficient to carry out the work needed to overcome the forces of attraction of other molecules of the liquid. Evaporation from different porous materials has been studied on different scales, from the **macropores**, for instance the study of moisture movement in porous materials under temperature gradient [91], the study of evaporation of water from soil [92] or study of evaporation driven process of growth of large crystallized salt structure in macroporous medium [93], to the **nano pores**, like the study of evaporation induced self assembly for the creation of nanostructures [94], or the process of solar evaporative cooling in context of well ordered nanoporous materials for low temperature water phase changes [95].

Despite its apparent simplicity because of the constant observation of this process under home conditions, the mechanisms behind the evaporation especially in terms of nano confinement has not been understood completely. There are many theoretical and experimental studies that consider different effect that occur during evaporation of volatile liquids from porous model system, for instance the study of evaporation from porous media that is based on the capillary model of a penetrating front [96], the study of evaporation in capillary porous media with the main focus on drying rates [97] or phase distributions [98].

Classic model, which describes the drying of porous materials is invasion percolation [99]. When modelling of invasion percolation one usually uses the concepts of immiscible displacements in porous media that is driven by mass transfer, like Tsimpanogiannis et. al. does in his manuscript [100], the calculations are mostly performed for 2D models. The direct imaging of process in 3D model systems is rare due to the difficulties that are combined with the direct imaging of porous systems. Instead of direct measurements, one uses different indirect methods, such as ultrasonic attenuation and light scattering [101] or electrical resistance during mercury injection [102]. It is possible to deduce important information from the

results obtained with these indirect methods, however it is not possible to investigate such phenomena, like flow patterns, abrupt bursts and redistribution of the liquid, for instance the Haines jump which require a method for direct non destructive investigation of the evaporation processes of volatile substances in 3D porous materials. **Haines jumps** [104] are rapid reconfigurations of invasion fronts during drainage process on time scales typically ranging from 1ms to 10ms [105].

Haines jumps (as illustrated in Figure 4.1) in the course of drainage processes are initiated as soon as the Laplace pressure of the invading non-wetting fluid exceeds the breakthrough value at the largest morphological restriction. Then, the configuration of the air invasion front gets unstable.

The Laplace pressure is the pressure difference between the inside and the outside

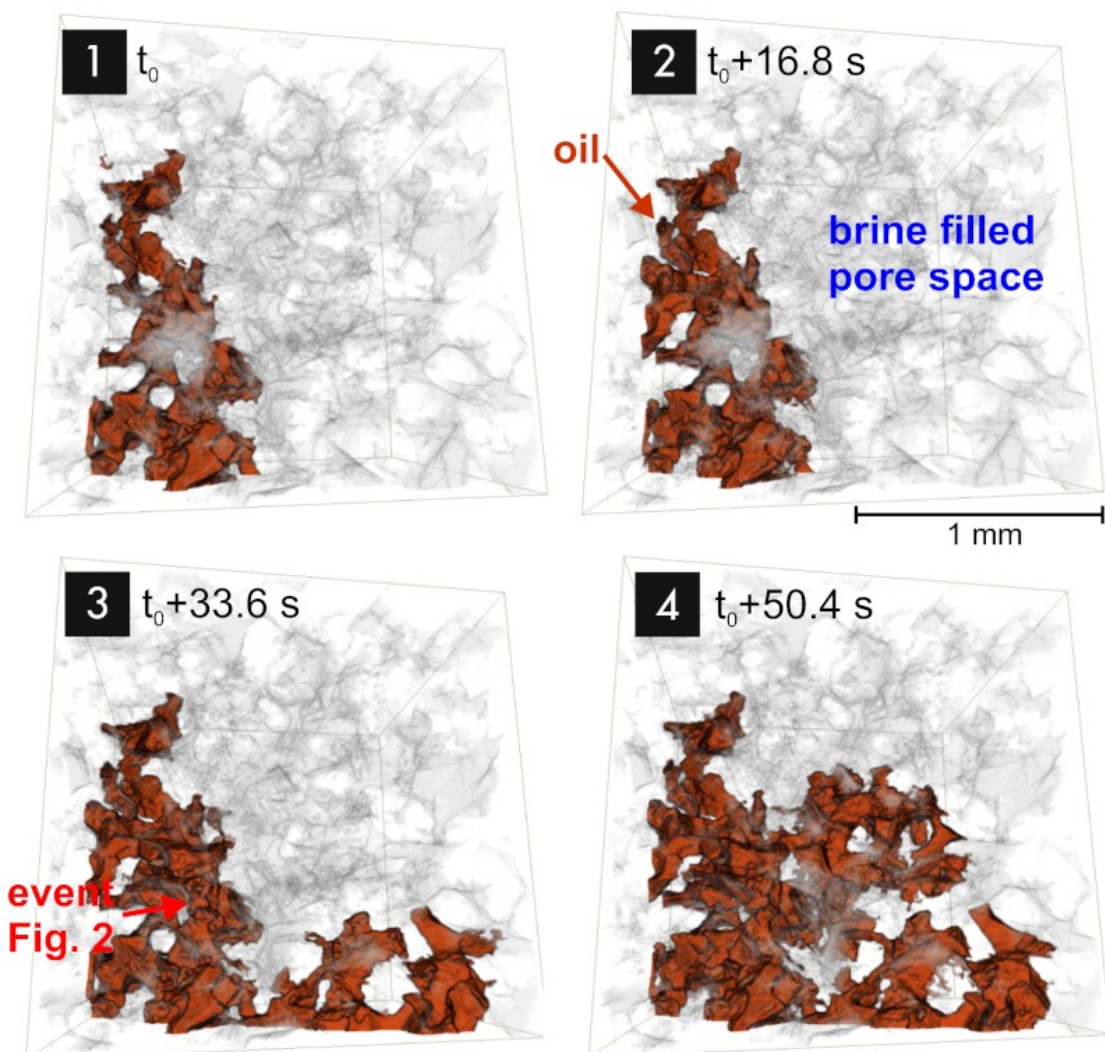


FIGURE 4.1: "Sequence of scans during drainage, at time intervals (Δt) of 16.8 s and with a voxel size of $3 \mu\text{m}$. The volume change (ΔV) from time steps 3 to 4 was 14 nL." (Figure taken from [103])

of a curved surface. The pressure difference is caused by the surface tension of the interface between liquid and gas.

Rapid redistribution of the receding wetting liquid by local liquid flow through hydraulically coupled pores displaces the menisci at the invasion front from narrower pores to wider pores where they have smaller curvatures [106]. The capillary pressure rapidly decreases following by spacial redistribution of the liquid. The process comes to an equilibrium after reaching the new stable configuration of air invasion front. Figure 4.1 taken from [103] illustrates Haines jump observed with high-speed, synchrotron-based X-ray computed microtomography. One can see the redistribution of the fluid inside porous membrane, but the fluid does not leave the porous host, it just redistributes. Haines jumps do not involve burst-like mass transfer of the evaporating guest species out of the porous host medium.

4.2 Evaporation dynamics of ethanol in Controlled Porous Glass observed with confocal microscopy

The CPG samples that are used in this experiments are characterized in Section 2.3.2. The experimental method is described in Section 3.1.2. R6G exhibits an absorption maximum 530 nm and an emission maximum at 552 nm (cf. PhotochemCAD package, version 2.1a). 50 μL of a 20 μM solution of R6G in ethanol were dropped onto the surface of the CPG membrane while the CLSM was already scanning. To capture fluorescence intensity mappings, the focal volume of the CLSM was displaced along the x direction for every z position starting at the bottom of the image field below the CPG membrane/glue/cover slide interface. The scanned area extended 250 μm (481 pixel) in z direction perpendicular to the CPG membrane/glue/cover slide interface and 52 μm (256 Pixel) in x -direction parallel to the CPG membrane/glue/cover slide interface. The duration of a scan and, therefore, the time resolution was 2 s. Sets of thus-obtained fluorescence intensity mappings were processed using the program ImageJ. Different phases of evaporation are shown in Figure 4.2. The first picture shows the distribution that occurred 20s after the infiltration. The bottom half is almost completely bright, the upper half shows a non homogeneous distribution of R6G molecules and therefore a non homogeneous distribution of ethanol molecules. Because the structure of porous glasses in many ways resembles the structure of sponge, it is logical to expect uneven local distribution of liquid and thus uneven evaporation process

that can be seen on the first frame of 4.2. Second and third frame from Figure 4.2 shows the inhomogeneity of evaporation. Last three frames show how suddenly fast the evaporation process may occur in the CPG. The 4th and 5th slides show a quick loss in of the intensity signal in the observed region. Since it is assumed that the presence of the intensity signal is correlated with the presence of ethanol, one can say that the 4th and 5th slides illustrate quick evaporation process. This quick evaporation process is defined as **burst event**, because the evaporation happens burst like, compared to the slow linear evaporation process observed in the first three slides. There are two seconds between them, however the mass loss is significantly higher than between the first two frames. The evaporation process is non homogeneous, we observe jumps, burst like mass losses. The air invasion front moved by about $100 \mu\text{m}$ towards the CPG membrane/glue/cover slide interface. Right after the jump between the 4th and the 5th frame, the R6G molecules are located at the bottom of the CPG membrane in the immediate vicinity of glass slide.

Evaporation process has ended and the system has reached equilibrium in which the dye molecules have reached the bottom of the membrane and settled on it.

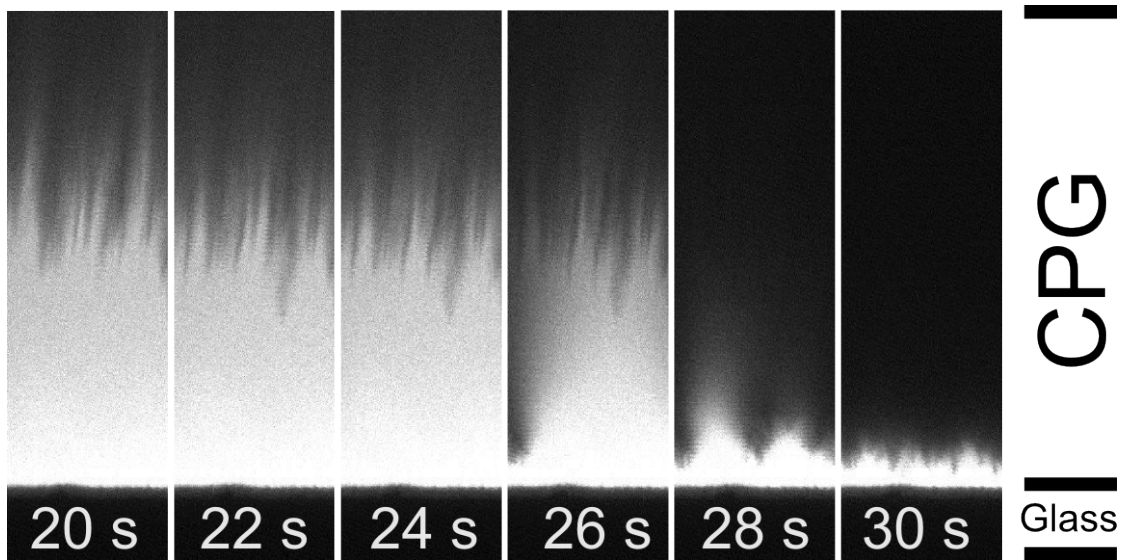


FIGURE 4.2: Different phases of evaporation of R6G-ethanol solution from CPG.

4.3 Spatio-temporal mapping of fluorescence intensity/evaporation using stacks of CLSM images

In order to demonstrate the dynamics of the process of evaporation complete burst events is visualized by averaging each frame to one 1D pixel array. The fluorescence intensity is integrated along x -direction parallel to the CPG membrane/glue/cover slide interface for every single z value. Thus one-dimensional intensities profiles are obtained where the fluorescence intensity codes a colour of single pixel along the z direction. Free-ware software imageJ (version 1.47v) is used for extracting the data from stack pictures. A Macro-script (Listing 4.1) is used to read the data automatically and save it as a stack of 2D data - measured averaged intensity along the x -axis vs z -axis. If you add these profiles along the time axis in chronological order an evaporation mapping profile is obtained, as demonstrated on Figure 4.3a. This is called spatio-temporal profile, because it shows simultaneously three parameters - the **spacial distribution** of fluorescence intensity along z -axis and averaged along x -axis and **chronological development** of this process. The spacial distribution is the y -axis on Figure 4.3, the time evolution is the x -axis and the fluorescence intensity is coded with a colour. Figure 4.3b shows the numerically calculated derivative of the average z position of the invasion front with respect to t , which is mean displacement rate (in $\mu\text{m}/\text{s}$). Since the position of evaporation front is known for each moment of time during the observation process, one can

```

for (i=1; i<=endFrame; i++) {
    run("Clear Results");
    setKeyDown("alt");
    profile = getProfile();
    for (k=0; k<profile.length; k++)
        setResult("Value", k, profile[k]);
    updateResults;
    Plot.create("Profile", "X", "Value", profile);
    if (i<10) {
        nr = "000"+i;
    } else if(i<100) {
        nr = "00"+i;
    } else if(i<1000) {
        nr = "0"+i;
    }
    filename = "..\\T"+nr+".xls";
    saveAs("Measurements", filename);
    run("Next Slice [>]");
}

```

LISTING 4.1: imageJ automation script for converting a stack of jpg data (fluorescence mapping pictures) into a stack of 2d intensity vs. distance profiles

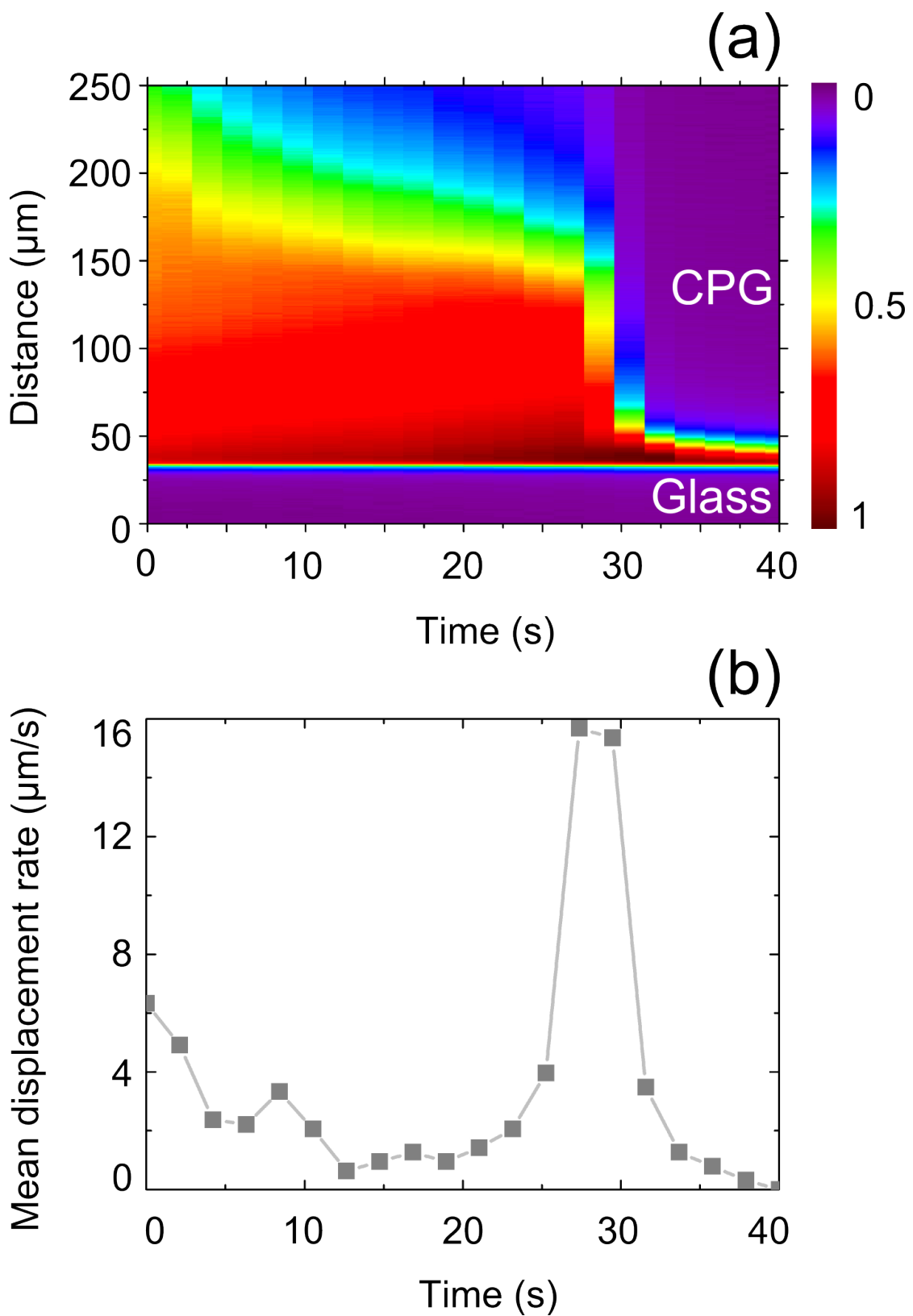


FIGURE 4.3: (a) Evaporation mapping of R6G/ethanol from CPG (b) First derivative of the average z position of the invasion front.

easily calculate the current displacement rate for each moment of time as $\frac{\Delta z}{\Delta t}$ with $\Delta z = z_{i+1} - z_i$ and $t = t_{i+1} - t_i$ and plot this as a function of t.

The graphs of first derivative show how significantly the evaporation speed, which is the same as the change of z position of the air invasion front, changes as a function of time in very short time period. A process of slow air invasion is interrupted by a blasting process at 25s that is shown on Figure 4.3b as a peak in the mean displacement rate profile. Taking into account the isotropic nature of the CPG pore system, it is reasonable to assume that the membrane volume affected by a burst-like mass loss event has similar extensions in all space directions. Hence, a CPG membrane volume of at least $10^6 \mu m^3$ was affected by the captured burst-like mass loss event. The CPG membrane volume affected by the burst-like mass loss event may extend beyond the scanned area.

4.4 Investigation with thermal analysis (combined TGA/DSC)

The combined TGA/DSC method is discussed in the corresponding Section 3.4. In order to understand the nature of observed burst-like evaporation profiles detected with confocal microscopy, the evaporation process was monitored with combined TGA/DSC methods under constant temperature $T = 25^\circ C$ (isothermal conditions). It is possible to measure the mass $m(t)$ and the heat flow \dot{Q} that is required to keep temperature constant, independently from each other. There are no fluorescent markers used, because it is not a microscopy method.

Figure 4.4 shows the mass as function of time $m(t)$ and heat flow $\dot{Q}(t)/m_0$ for an infiltrated CPG membrane for the whole period of evaporation. The last phase of evaporation is highlighted by in Figure 4.4a. Inside the highlighted rectangle you can see several step transitions. The heat flow curve does not show this behaviour (Figure 4.4b). Figure 4.5a shows enlarged marked sector of Figure 4.4a, stepwise mass losses can be interpreted as blast evaporation observed with CLSM method. Figure 4.5b shows the first derivative curve $dm(t)/dt$ of the mass loss observed in Figure 4.5a. Linear evaporation profile is replaced with a stepwise evaporation.

Figure 4.4 shows the mass as function of time $m(t)$ and heat flow $\dot{Q}(t)/m_0$ for an infiltrated CPG membrane for the whole period of evaporation. The last phase of evaporation is highlighted by in Figure 4.4a. Inside the highlighted square

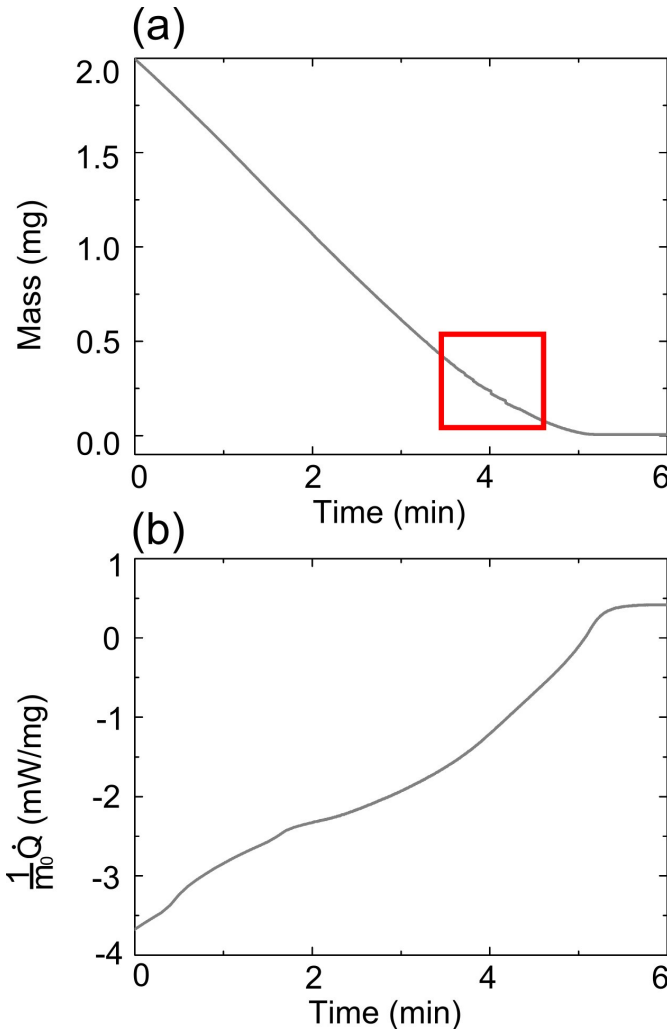


FIGURE 4.4: a)The result of TGA analysis of burst like mass loss events during evaporation of ethanol from CPG b) The result of DSC analysis during evaporation of ethanol from CPG

you can see several step transitions. The heat flow curve does not show this behaviour(Figure 4.4b). Figure 4.5a shows enlarged marked sector of Figure 4.4a, stepwise mass losses can be interpreted as blast evaporation observed with CLSM method. Figure 4.5b shows the first derivative curve $dm(t)/dt$ of the mass loss observed in Figure 4.5a. Linear evaporation profile is replaces with a stepwise evaporation, huge amounts of mass are lost within milliseconds.

The burst like mass losses where not accompanied by burst like heat flow changes, as can be seen on Figure 4.5c and d, showing the $\dot{Q}(t)/m_0$ and $\ddot{Q}(t)/m_0$ profiles. m_0 corresponds to the sample mass at the start of the TGA treatment.

$dm(t)/dt$ is considered as a more realistic measure of the burst velocity than the displacement rate of the air invasion front derived from the CLSM mappings because the time resolution of the TGA device used here is one order of magnitude

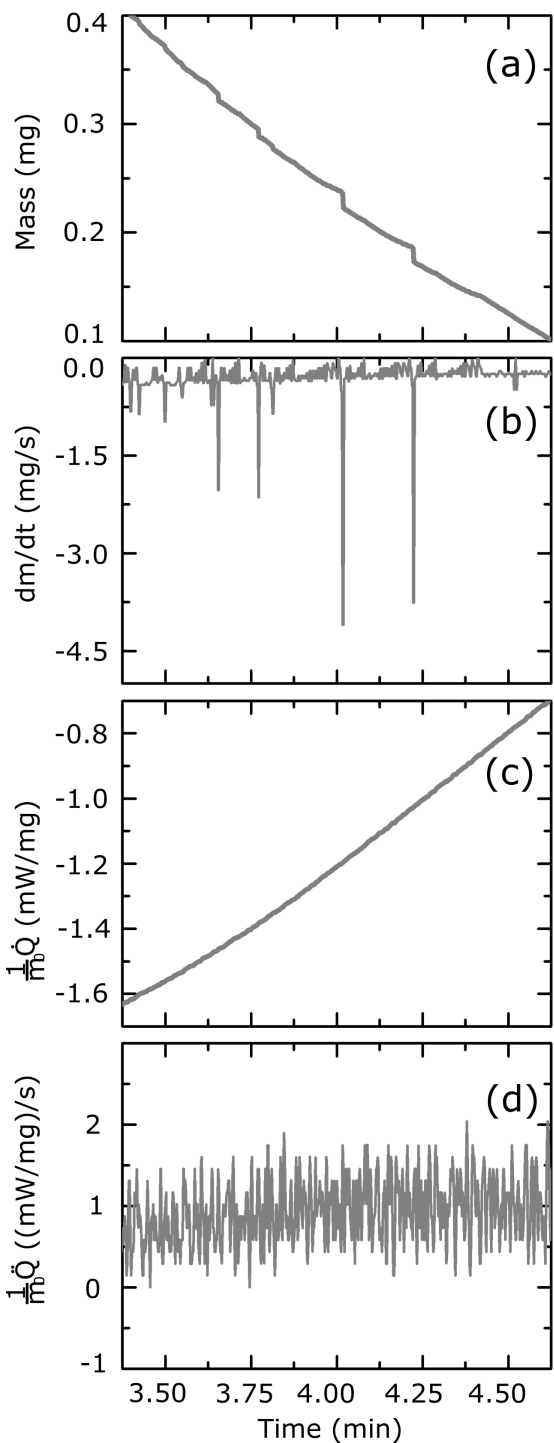


FIGURE 4.5: TGA and DSC analysis of burst-like mass loss events during evaporation of ethanol from CPG a) Sample mass m as a function of evaporation time t . The constant sample mass after evaporation of ethanol finished was set to 0 mg b) dm/dt as function of time t , result of numerical differentiation of $m(t)$ profile from panel (a) c) Heat flow profile as function of t measured at the same time as mass loss d) Change in heat flow, calculated by numerically differentiating the heat flow profile from (c) with respect to t as a function of time t

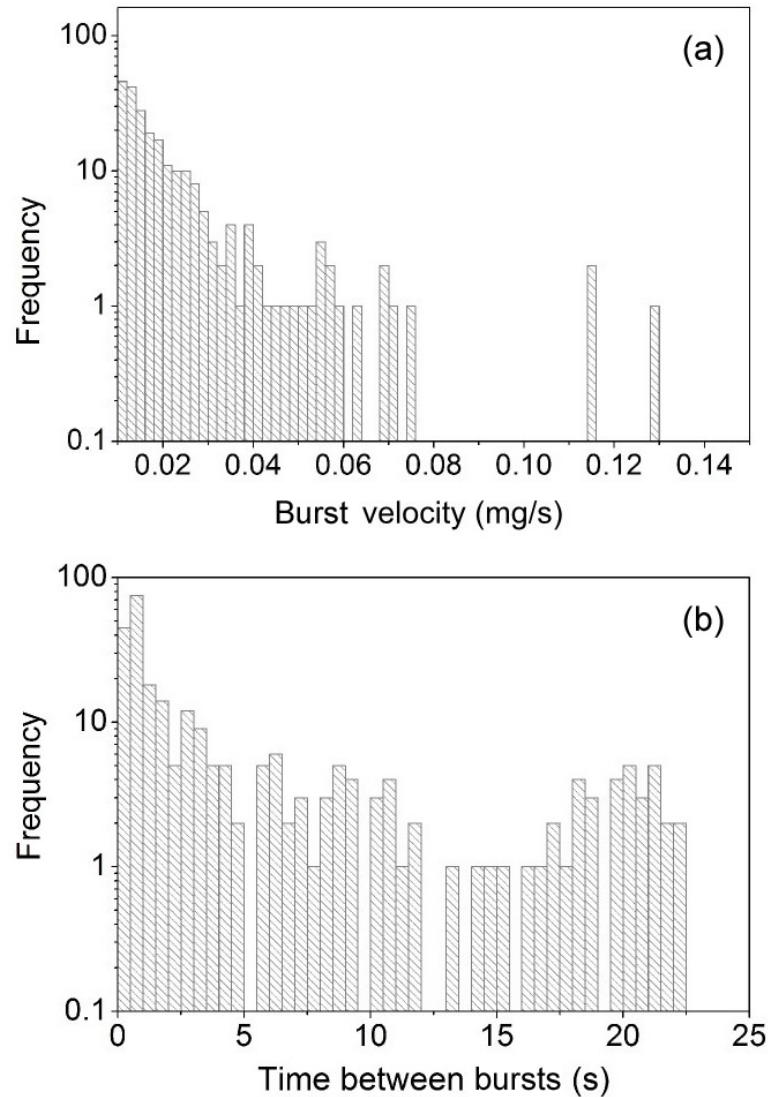


FIGURE 4.6: Statistical evaluation of adiabatic evaporation bursts captured in 10 independent TGA experiments. The cut-off size to separate adiabatic evaporation bursts from noise was set to 0.01 mg/s. a) Frequency density of the velocities dm/dt (mass loss per time interval) of overall 298 adiabatic evaporation bursts. b) Frequency density of time intervals between burst-like mass loss events during evaporation of ethanol from CPG. Overall 297 time intervals were considered.

better than the time resolution of the CLSM measurements and because the CLSM scans only capture a fraction of the CPG volume affected by a jump of the air invasion front.

The evaluation of 298 burst-like mass loss events 4.6a captured in 10 independent TGA experiments revealed that the frequency density f of v can be fitted by a power law of the type

$$f = a \cdot v^b$$

with the pre-exponential factor $a=0.003$ (s/mg) and scaling exponent $b = -2.6$.

The largest burst-like mass loss event we captured was associated with a burst velocity of 0.1275 mg/s. This evaporation velocity corresponds to 27 μg liquid ethanol in the volume of $3.4 \cdot 10^7 \mu\text{m}^3$ that is converted to gas phase. The frequency density of time periods between burst-like mass loss events is shown in 4.6b. Frequency maximums occur at 2-3 s and at around 20 s.

4.5 Calculation of enthalpy of evaporation

The enthalpy of evaporation, also known as the (latent) heat of vaporization or heat of evaporation, is the enthalpy change that is needed to transform substance from a liquid state into a gas state at certain pressure value.

The experiment was conducted under conditions in which the temperature is kept constant and the volume changes during evaporation so one can define an isothermal and non isochoric system.

The molar enthalpy of evaporation of ethanol is 42.32 kJ/mol at 25°C [107]. The \dot{Q}/m_0 profile that was directly measured, was compared with the \dot{Q}/m_0 profile calculated from the mass change data between 3.5 and 4.5 minutes that is shown in Figure 4.5a. Figure 4.7 shows calculated \dot{Q}/m_0 profile and time derivative \ddot{Q}/m_0 . If the evaporation of ethanol from CPG was purely endothermic, than the heat flow diagram would reproduce the same curve course as the mass diagram, because the curve course of the endothermic process is basically the function of mass change multiplied with enthalpy of evaporation. Therefore one would expect the same spikes in the heat flow diagram as calculated and shown on Figure 4.7 that are measured in the mass change curve. These spikes can not be seen in the measured heat flow curve as can be seen in Figure 4.5c and d. The heat flow is therefore not directly correlated with the mass change. The process of evaporation is not purely endothermic. Hence, the burst like mass loss events must be

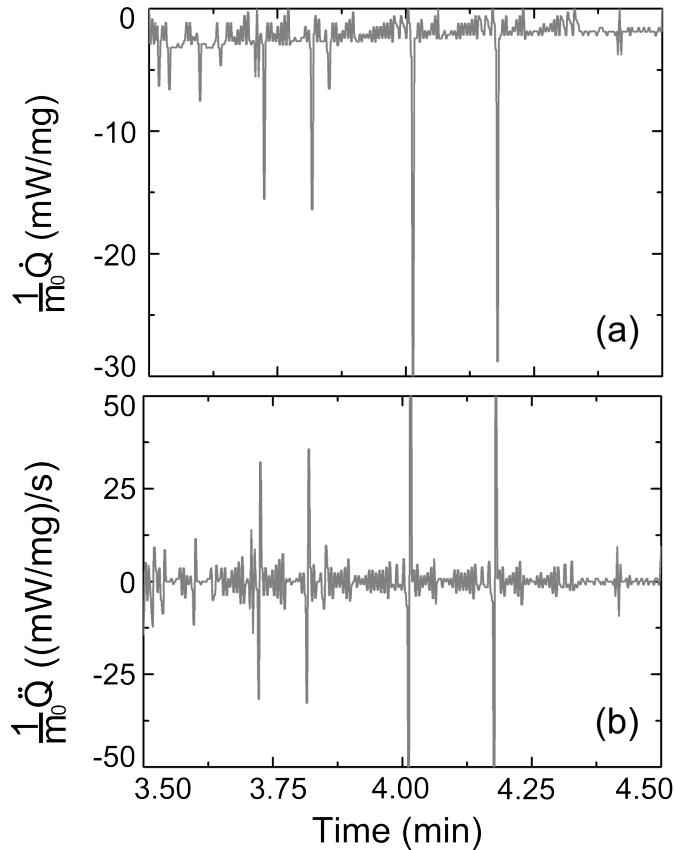


FIGURE 4.7: Simulation of purely endothermic evaporation based on the $m(t)$ trace of 4.5a. a) Heat flow \dot{Q} normalized to the initial sample mass m_0 as function of evaporation time calculated for the experimental $m(t)$ profile displayed in 4.5a using the molar enthalpy of vaporization of ethanol at 25°C. b) Change in heat flow \ddot{Q} normalized to m_0 calculated by differentiating the $Q(t)/m_0$ profile of panel a) with respect to t .

adiabatic since they were not accompanied by spikes in the heat flow.

The absolute enthalpy of vaporization expected for evaporation exclusively occurring in the classical endothermic evaporation mode between $t = 3.50$ minutes and $t = 4.50$ minutes amounted to 275.6 mJ and was calculated by numeric integration of the \dot{Q}/m_0 profile seen in Figure 4.7a. In striking contrast, numerical integration of the directly measured \dot{Q}/m_0 profile displayed in Figure 4.5c between $t = 3.50$ minutes and $t = 4.50$ minutes yielded an actual evaporation enthalpy of only 143.2 mJ.

4.6 Discussion

Three main points should be discussed based on the obtained results to understand the nature of of **adiabatic** and **non endothermic** evaporation bursts:

- the nature of the liquid phase in the porous media with a pressure below the pressure range of thermodynamic stability;
- the reasons, why the observed jumps are not the classical Haines jumps;
- discussion of the mechanisms that initiate the observed adiabatic evaporation jumps.

4.6.1 Adiabatic conversion of an unstable liquid phase into a gas phase

Since there is there is a presumption that the observed quick mass losses with TGA/DSC or correlated intensity jumps with CLSM have adiabatic and not endothermic nature, it should first be discussed, how these processes differ and what is the nature of adiabatic evaporation.

A classical endothermic evaporation is a process, where the partial pressure of the evaporating species in the gas phase is below the value in the equilibrium phase. The partial pressure of the gas is measured as the thermodynamic activity of gas molecules. Thus, those molecules of ethanol, which carry a higher mean value of the kinetic energy, leave the liquid phase and pass into the gaseous phase. Liquid phase loses molecules with high kinetic energy, and thus loses temperature. Under isothermal condition, the described scenario would be accompanied by the heat flow from the surrounding environment to the liquid that is driven by non-equilibrium partial pressure of the evaporating species.

During the TGA/DSC experiments described in the section 4.4 evaporation of ethanol from CPG membranes where observed by measuring the weight and the heat flow simultaneously. According to a classical evaporation scenario that is purely endothermic, one would expect that whatever happens with a mass of ethanol during the evaporation process and detection of $m(t)$, this would have direct influence on the heat flow curve. Which means, the observed spikes in Figure 4.5a and b would also be some sort of spikes in Figure 4.5 c and d. Interestingly,

this is not the case that means the heat flow is not a linear function of the mass change. The calculated evaporation enthalpy(value 275.6 mJ) that correspond to the theoretical heat flow displayed in Figure 4.7 differs from the real measured evaporation enthalpy(value 143.2 mJ) that correspond to the heat flow from Figure 4.5c. Almost the half of ethanol evaporates without heat transfer from the surrounding, which means adiabatically. Adiabatic conversion of the liquid phase into a thermodynamically stable gas phase may happen when the pressure of the liquid phase is below the range in which the liquid would be thermodynamically stable.

There are experimental results, showing that the liquids confined to nanoporous systems indeed have very low pressure, for instance for water in nano-channels [108], [109], [110]. Theoretically this effect was confirmed in a simulation for capillary-pressure-induced cavitation probability in nano-channels [111].

The reason for a very low pressure of liquid confined to the nanopores can be rationalized as follows. The air invasion front consists of menisci that are concave with respect to the receding wetting liquid and convex with respect to the invading non-wetting gaseous fluid.

According to the Young-Laplace equation, the pressure in the receding wetting liquid must be lower than the pressure in the invading non-wetting gas phase. The capillary pressure P_C is the resulting difference across a meniscus according to [112]. Changing curvature of the meniscus leads to an increase in the capillary pressure. The structure of controlled porous glass is inhomogeneous (see section 2.3.1), it is possible to define average pore diameter, however this value scatters around average value(Figure 2.9), therefore there are narrow pores and larger pores. When having the same contact angle, it must be that way that menisci in the narrow pores are more curved than in wider pores. Therefore the capillary pressure P_C is larger in narrow pores. Pressure differences in the receding wetting liquid caused by different meniscus curvatures draw the receding wetting liquid from wider pores into narrower pores [113], [114, 115]. That leads to further increase in capillary pressure and decrease in liquid pressure.

Finally, the air invasion front gets unstable and relaxes. The observed burst-like mass loss events can be considered as adiabatic evaporation bursts, which push the system towards equilibrium along an adiabatic but non-isochoric route.

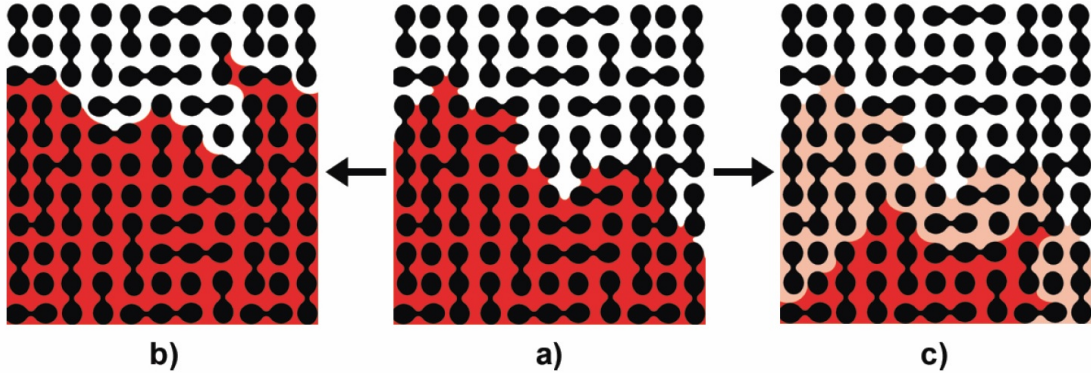


FIGURE 4.8: Relaxation mechanisms of an unstable air invasion front (black, porous host; red, evaporating liquid). a) In the course of drying, the menisci at the air invasion front are drawn in narrow pore segments (pore necks). As a result, the curvatures of the menisci and the Laplace pressure across their interfaces increase. Eventually, the air invasion front gets unstable. b) Hydraulic relaxation of the unstable air invasion front by classical Haines jumps involves local liquid flow at the air invasion front so as to realize meniscus configurations characterized by lower meniscus curvatures and lower Laplace pressures. However, no mass transport away from the air invasion front takes place. c) In narrow nanopores, the curvature of the menisci is so pronounced that the liquid in the vicinity of the menisci has a pressure below the pressure range in which the liquid would be stable. Relaxation of the air invasion front thus occurs by adiabatic burst evaporation converting unstable liquid to gas. The conversion front propagates avalanche-like into the liquid-filled volume of the nanoporous host until a new stable air invasion front characterized by low meniscus curvatures and low Laplace pressures forms. The beige area indicates the liquid volume converted to gas. As adiabatic burst evaporation is associated with volume expansion, the formed gas is pushed out of the porous host that correspondingly loses the mass of the converted liquid in a burst-like mass loss event.

4.6.2 Evaporation bursts vs. classical Haines jumps

In general, one can consider the evaporation process of liquid from a nanoporous host as drainage of air phase into the liquid phase. Rapid reconfiguration of the liquid phase in porous medium on the time scale from 1ms to 10ms [105] is well known from the literature and is called after the discoverer - Haines jumps [104]. If one assumes that the observed evaporation bursts are based on the Haines jumps, it is still not clear, why the evaporation velocity is so high. One possible explanation for enhanced evaporation rate would be the presence of thin wetting layer of evaporated liquid after the Haines jump occurred. The increased air/liquid interfacial area related to the presence of the thin wetting layer could be considered as possible origin of enhanced evaporation rates. However, while the thin wetting

films would have been generated by a jump-like event, evaporation of thin wetting films as such would not be burst-like. The thin wetting layer would evaporate in the classical endothermic mode. Which leads to a conclusion that adiabatic mass losses can not be explained by at least classical haines jumps.

4.6.3 Initiation mechanisms of adiabatic evaporation jumps

Analysis of the TGA/DSC experiments has shown that the adiabatic evaporation process has discrete nature, which means there must be a mechanism that initiates this process. A common mechanism for the formation of gas menisci within liquids is cavitation [116], which is initiated by homogeneous or heterogeneous nucleation. Cavitation occurs as a result of local reduction of pressure in the fluid, which can occur either by increasing its speed (hydrodynamic cavitation), or by passing the acoustic waves of high intensity during the half-period of rarefaction (acoustic cavitation), there are other causes of the effect. Moving with the flow in the area of higher pressure or during the half-cycle compression, cavitation bubble collapses, with emission of a shock wave.

However, it is reasonable to assume that adiabatic evaporation bursts are not initiated by classical nucleation of a gas phase within a liquid phase due to a fact that cavitation initiated by classical nucleation in the liquid phase while confined to pores leads to a meniscus pinning, as shown in [117]. Consequently, the standard situation would be the presence of large gas bubbles that are surrounded by infiltrated liquid accompanied by pinning of the menisci at the air invasion front. The series of CLSM images did not show any evidence of meniscus pinning, instead, CLSM monitoring indicated that adiabatic evaporation bursts start at air invasion fronts and propagate away from the initial positions of the air invasion fronts into initially liquid-filled regions of porous media. At the air invasion front there is a sufficient amount of gas bubbles that topologically correspond to a semi sphere or a "half bubble". In contrast to homogeneous nucleation, heterogeneous formation of bubbles on the outer surfaces [118] reduces the required amount of free energy, which must be overcome in order to form a thermodynamically stable nuclei.

Analogous to external surfaces initiating heterogeneous nucleation, the meniscus interfaces at the air invasion front may facilitate initiation of adiabatic evaporation bursts. However, as meniscus interfaces are permanently present, initiation of adiabatic evaporation bursts by heterogeneous nucleation should be a sporadic

process. This is evidently not the case.

The statistic analysis of time intervals between burst-like events seen in Figure 4.6b shows the presence of two frequencies, there are two process which occur on average at two different time intervals. The initiation of adiabatic burst evaporation must be coupled to another process that determines the duration of these time intervals. The build up of capillary pressure that destabilizes the meniscus configuration at the air invasion front corresponds to this process. Menisci at the air invasion fronts of microporous and mesoporous media as well as of media with small macropores just above the mesoscopic size range are strongly curved. Thus, the corresponding capillary pressures are high and the liquid pressures close to the menisci are so low that the liquid may be metastable. Under these conditions, jump-like relaxations of air invasion fronts will occur by adiabatic burst evaporation rather than by Haines jumps.

The burst evaporation events and the avalanche like intrusion of the air into the pores are coupled events. The air invasion front moves due to the vaporization of metastable infiltrated ethanol and not due to the redistribution of the liquid inside the porous system as it is reported in case of Haines jumps. The rapid adiabatic conversion of receding wetting liquid to gas is a non-isochoric process associated with significant volume expansion. The evaporated liquid is pushed out of the porous system as a gas which reduces the total mass of the porous system-liquid composite stepwise in a jump-like process. Hence, Haines jumps and adiabatic burst evaporation are competing mechanisms for the reconfiguration of unstable air invasion fronts, and it is straightforward to assume that in nanoporous media adiabatic evaporation bursts prevail. However the stopping criterion for the rapid jump-like evaporation might be the same as for the Haines jumps process - the process stops as soon as liquid pressure prevails over the capillary pressure which leads to stabilization of a new configuration of the air invasion front.

4.7 Conclusion and outlook

Using ethanol as evaporating model liquid and controlled porous glass as nanoporous model matrix, it was possible to show that adiabatic burst evaporation significantly contributes to the evaporation of volatile liquids from nanoporous media

with nano-pore diameters of a few 10 nm and sponge-like bi-continuous morphology. The comparison of experimentally measured vaporization enthalpies and vaporization enthalpies expected for exclusively endothermic evaporation calculated from liquid mass loss revealed that nearly half of the liquid evaporated adiabatically. Adiabatic burst evaporation is accompanied by burst-like mass loss events during which liquid volumes of up to $10^7 \mu m^3$ are converted to gas.

Adiabatic burst evaporation occurs because liquid in the vicinity of strongly curved menisci inside nanopores has low liquid pressures and is, therefore, metastable. Burst-like conversion of metastable liquid to gas is triggered by unstable meniscus configurations at air invasion fronts caused by the build-up of high capillary pressures. Adiabatic evaporation bursts propagate avalanche-like through sponge-like nanopore systems until a new stable configuration of the air invasion is reached. The experimental results indicate that in nanoporous media adiabatic evaporation bursts prevail over Haines jumps, another mechanism for the relaxation of unstable air invasion fronts that involves reconfiguration of the menisci at the liquid-air interface by local liquid flow without mass transfer away from the air invasion front. These insights may improve the understanding of drying processes in bottom-up syntheses of nanoporous materials based on sol-gel chemistry or spinodal decomposition in solution, of solution impregnation of porous media with functional materials and of desorption processes in nanoporous media.

Chapter 5

Evaporation of volatile guests from hosts with straight cylindrical pores

5.1 Introduction

In the previous chapter it was shown that the dynamics of evaporation from porous glass (which was chosen as model system for a sponge like porous host systems) observed with fluorescence microscopy using fluorescence mapping and combined TGA/DSC method has avalanche-like features that could be interpreted as adiabatic evaporation bursts, which largely occur due to the geometric properties of investigated porous membranes. In order to prove this statement, porous hosts where chosen, which geometrical properties are in striking contrast to CPG - the porous alumina membranes, also called AAO, with aligned, straight, cylindrical pores uniform in diameter with closed pore bottoms. Figure 2.2 illustrates the main schematic differences between CPG and AAO. The evaporation dynamics of ethanol is studied in the absence of effects related to the local variations in the Laplace pressure. In addition to the dynamics of evaporation, the behaviour of dye molecules inside the pores of AAO should be studied as a function of time and space revealing possible effects due to the presence or absence of the solvent and the internal structure of the pore walls of AAO.

Evaporation from AAO is of particular interest from the point of view of practical application and fundamental knowledge. Penetration of the polymer melts and

solutions in the porous alumina is a preliminary step necessary for the production of nanoporous composite materials [23]. The infiltration of polymer solutions into AAO can be done directly with polymer melts or using the polymer solution in an appropriate solvent [119]. Each method has its advantages. The first, direct method makes it possible to skip the process of dilution but is very slow and depends on the viscosity value of the investigated matter. The second process that is based on a dilution process makes the infiltration process much faster, but it needs to be repeated many times, because every time only small amount of polymers is infiltrated after the solution has completely diluted.

The properties of R6G in different solvents (in this case it is R6G/ethanol) have also been studied extensively over decades. Fluorescence quantum yield of rhodamine 6G in ethanol as a function of concentration [120] was studied with thermal lens spectrometry and it was shown that the quantum yield is independent of concentration in certain interval. The fluorescence quenching of rhodamine 6G was studied in methanol at high concentration [69]. The main reason for the rapid reduction of fluorescence lifetime above 10^{-2} mol/l is mainly due to energy transfer to quenching centres. Absorption behaviour of methanolic rhodamine 6G solutions at high concentration [121] was measured and it was found that there is huge deviation from the Beer's law at high concentrations, which is explained by the mutual interaction of neighbouring molecules.

5.2 Evaporation dynamics of ethanol in AAO observed with confocal microscopy

The AAO membranes that are used in this experiment are characterized in Section 2.2.2. The evaporation dynamics from AAO, which is a model system for a guest membrane with discrete cylindrical pores, in contrast to CPG that was a model system for sponge-like porous membrane, was detected with the same method that was used in a previous chapter - fluorescence mapping with CLSM. The description of this methodology can be taken from 3.1.2. Three different phases of evaporation are shown in Figures 5.1 and 5.2. Figure 5.1 shows three phases of fluorescence intensity mapping of R6G distributed along the volume of AAO. Figure 5.2 shows corresponding fluorescence intensity as function of space (more specifically, as function of distance z, see Figure 3.2). The fluorescence mapping

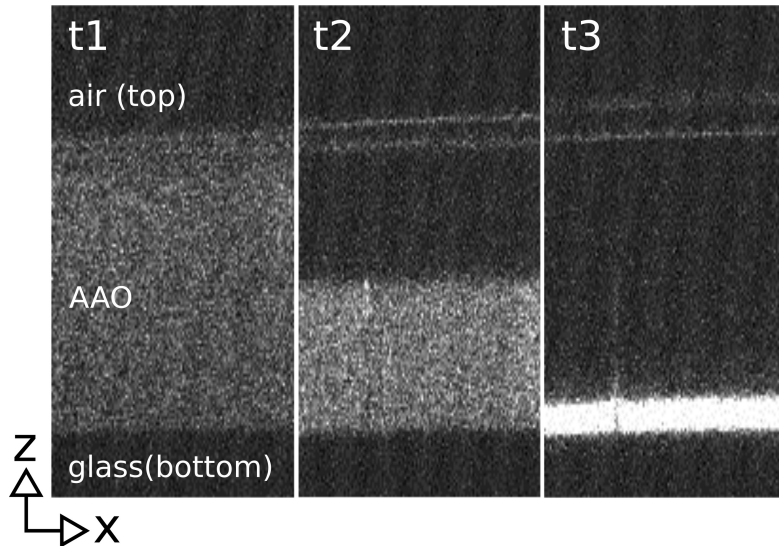


FIGURE 5.1: Intensity mapping of R6G molecules distributed in the volume of AAO membrane. The position of AAO membrane is shown that way that the pore openings border on the air that is on top (top) and the pore bottom borders with glue layer/glass slides (bottom). Three different phases of evaporation of ethanol from AAO are shown t1) The moment of time when the evaporation front reached the surface of AAO and all the evaporating ethanol is completely inside the membrane t2) The moment of time when the evaporation front reaches the middle of the AAO pores t3) The moment of time when the evaporation process is almost completely over since all R6G molecules are on the bottom of AAO pores

pictures are displayed that way that the pore openings are on the top and border the air phase and the pore bottom are on the bottom and border the glue/glass. The evaporation front is straight in x-direction as can be seen in Figure 5.1. This is due to the straight aligned and separated nature of the pores.

Three different phases of evaporation of ethanol from AAO are shown.

- The point of time when the evaporation front reached the surface of AAO and all the evaporating ethanol is completely inside the membrane is marked as t1. One can see linear profile in x-direction, which is due to well ordered morphology of the pores. The corresponding intensity mapping from Figure 5.2t1 shows linear intensity distribution along the z-axis. Since all the R6G molecules are uniformly distributed inside AAO membrane except the small amount that is on to of the membrane, there is no reason for any density gradient of R6G molecules, which is confirmed by the intensity graph.
- The moment of time when the evaporation front reaches the middle of the AAO membrane is marked with t2. One can see that the surface is marked

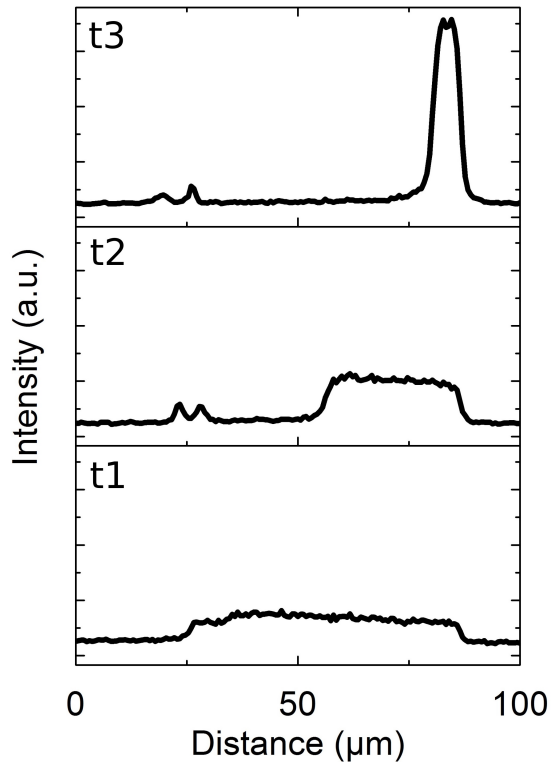


FIGURE 5.2: Intensity vs. distance diagram that is spatially correlated with the intensity distribution shown in 5.1. Three different phases of evaporation of ethanol from AAO are shown t1) The moment of time when the evaporation front reached the surface of AAO and all the evaporating ethanol is completely inside the membrane t2) The moment of time when the evaporation front reaches the middle of the AAO pores t3) The moment of time when the evaporation process is almost completely over because all R6G molecules are on the bottom of AAO pores

with two straight lines. The first line might really be the layer of R6G molecules that are on top of the AAO membrane, the second line is due to the optical effects because of the differences in refractive index between AAO and air. There is still no intensity gradient and therefore no density gradient of R6G molecules, as can be seen in corresponding intensity distribution on Figure 5.2t2.

- The last moment of evaporation, when all the ethanol almost completely evaporated and the intensity reaches its maximum, as can be seen in the corresponding intensity profile in Figure 5.2t3.

The position of evaporation front and numerically calculated displacement rate or evaporation velocity is shown in Figure 5.3. The position of evaporation front

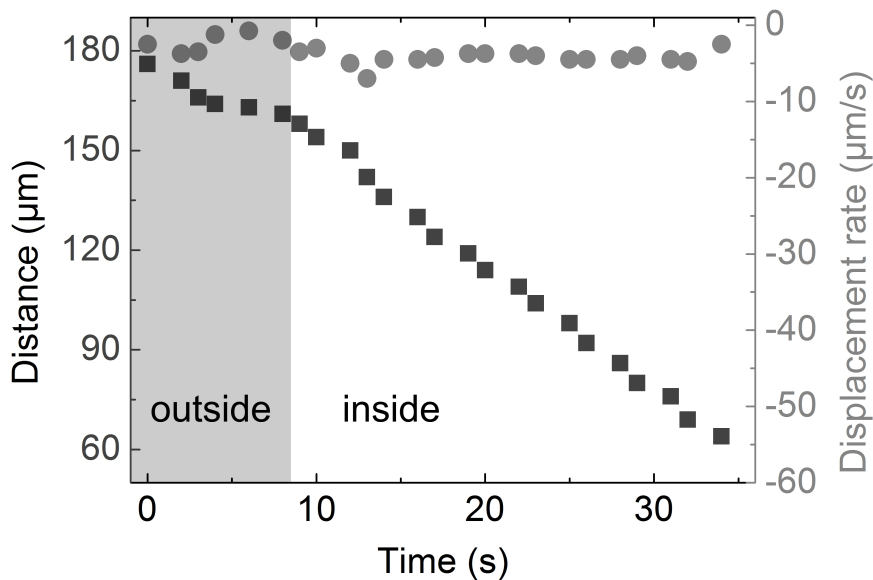


FIGURE 5.3: Position of evaporation front and numerically calculated displacement rate of ethanol in AAO based on the fluorescence intensity data shortly above the AAO membrane and completely inside. The area outside the AAO membrane is marked grey. Squares is the data for distance, circles represent displacement rate.

was determined for each moment of time from the moment when the evaporation front reached the focal are to the end of evaporation and plotted as function of time. One can see linear nature of evaporation process, which occurs without any unpredicted displacements or jump, as was observed and discussed in the previous chapter for CPG membranes. The evaporation velocity was determined by numerically integrating the distance vs. time curve and also shows linear nature with some fluctuation around the mean value. The slope inside AAO membrane is $v_{in} = 3.772 \mu\text{m}/\text{s}$, the slope outside AAO membrane, or better to say in a droplet, is $v_{out} = 1.794 \mu\text{m}/\text{s}$. The apparent evaporation velocity inside AAO membrane is therefore almost twice as fast as outside, even though no evaporation jumps could be observed (if the fluorescence redistribution really corresponds with the actual presence or absence of ethanol molecules).

5.3 Intensity redistribution of R6G molecules in AAO as function of time and space

Now the behaviour of R6G molecules should be considered directly since their presence or absence is a direct indication for the presence or absence of ethanol.

First, two quantities should be defined - the **maximal fluorescence intensity** and the **integral fluorescence intensity**.

The **maximal fluorescence intensity** (I_{max}) is, as the name suggests, the maximal intensity that is measured in a single fluorescence mapping picture, like in Figure 5.1. When the intensity is plotted vs. distance (the z-position) like in corresponding Figure 5.2, the maximal intensity is the maximal plotted value. This value characterizes the density of R6G molecules in a given area but it also might characterize the fluorescence efficiency of R6G molecules in a given area.

The **integral fluorescence intensity** (I_{int}) is an integral value of the intensity, it is calculated by summing up all measured intensity values along the x direction. It characterized the fluorescence efficiency of R6G in the whole scanned area independent of their density.

Figure 5.4 shows the whole dynamics of R6G distribution inside AAO membrane from the moment when the evaporation front reaches focal area (like in Figure 5.2t2), to the moment when the evaporation front reached the bottom of AAO (like in Figure 5.2t3) and several seconds after.

Like it was done for CPG membranes in Section 4.3, the fluorescence intensity was integrated along the x-direction parallel to the AAO/glue/cover slide interface (which is shown in Figure 3.2) for every single z-value. This way it was possible to condense every CLSM image into a one-dimensional array of pixels that is oriented parallel to the z axis and normal to x axis and experimental set-up. It is possible to average the intensity along the x-direction because of the homogeneity of the fluorescence signal in AAO membrane along the x axis, due to the homogeneous evaporation profile along this direction.

Figure 5.4 shows horizontally oriented one-dimensional pixel arrays. The time line is directed upwards. Thick dotted vertical line divides the image into two regions - on the left is a glass substrate, the right side shows AAO membrane and the processes occurring in it. The right side is subdivided conditionally into three periods of time by two thin horizontal dashed line. These time periods are marked with Roman digits.

It should be mentioned that this is a representative result. All experiments show the same results. **Phase I** shows the infiltration and evaporation process before the evaporation front reaches the focal volume. The intensity is relatively low because of the low initial concentration of R6G and high amount of ethanol in the membrane.

Phase II shows the evaporation process right after the evaporation front entered

the focal volume up to the moment when ethanol completely evaporated. The amount of solvent in the pores decreases at a higher rate.

Phase III shows the unexpected behaviour of the fluorescence signal after all the solvent has evaporated. The observed profile of evaporation signal after the 3rd phase has a half of a maximal intensity of the last pixel array of the 2nd phase, but much higher average or integral intensity than during the whole evaporation process.

It should be mentioned that since the pores of AAO are closed, the R6G concentrates within the membranes.

While there is nothing unusual in the evaporation process, which resembles the evaporation from a glass substrate and shows linear nature(5.3), the fluorescence signal shows quite unexpected behaviour and should be taken into the details.

As one can see from Figure 5.4III, there is a change in the fluorescence profile after the solvent has completely evaporated. The fluorescence signal becomes higher

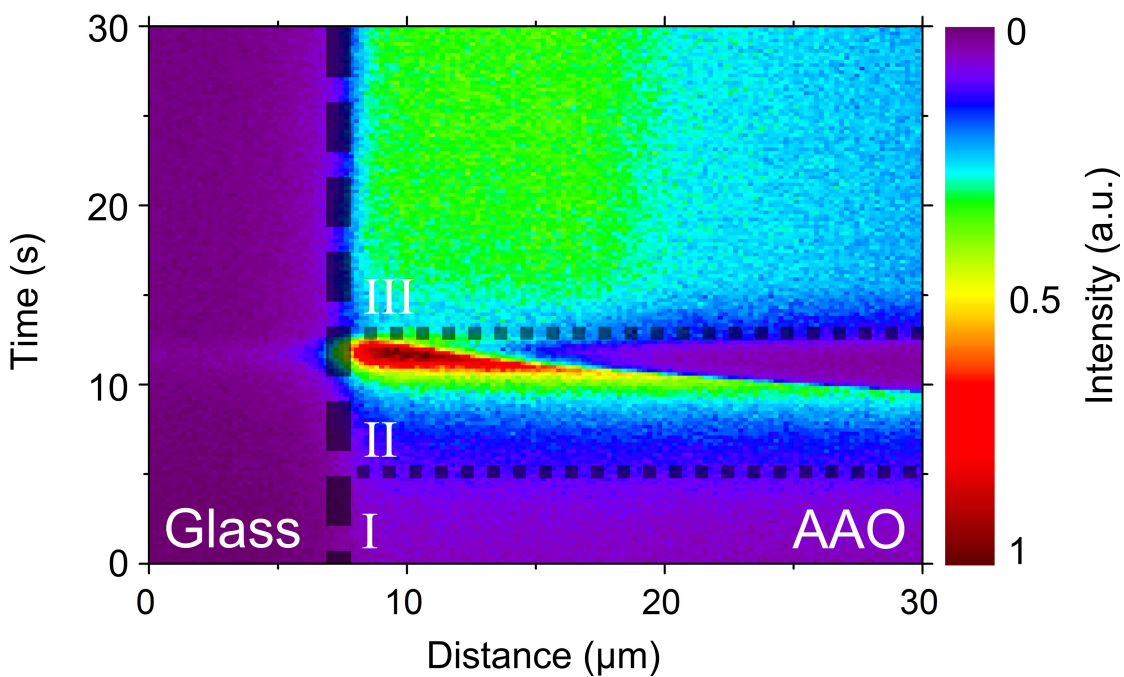


FIGURE 5.4: Representative result of evaporation dynamics of ethanol/R6G from AAO summed up to a stack of 1D pixel array (see Section 4.3). Vertical line separates the glass from the porous alumina. The two horizontal lines indicate the three phases of the experiment. First (I) - First phase of evaporation, the evaporation front is not yet visible. The second (II) - evaporation front is visible in the investigated area, evaporation occurs in a few seconds. The third phase (III) - the "broadening" of the fluorescence signal after ethanol completely evaporated.

and is distributed along the whole imaged area in contrast to the processes observed during the 5.4II, when only area with present R6G molecules fluoresce.

Time resolved 3D orientation spectroscopy (see Section 3.2) experiment was performed in order to understand the dynamics of angular distribution of R6G molecules during the evaporation.

The angular distribution of the dipole emission of R6G was analysed defining the angular distribution of the two classes - the outer and inner angle. In this experiment had to show if there is a dominant emission dipole distribution in one of the observed systems.

The results are shown on Figure 5.5 for both systems - ethanol/R6G solution on glass and inside AAO membrane. Figure 5.5 (a) shows signal intensity for exterior and interior angles of R6G on glass, one can see that during the evaporation process, the exterior angle (black) slightly dominates, but right after the disappearance of the solvent, the ratio of exterior to interior angle (red) changes with the strong dominance of the exterior angle (the intensity ratio is almost 1:2). Figure 5.5 (b) shows signal intensity for exterior and interior angles of R6G inside AAO. Here we see the same dynamics as on glass - almost no difference during the evaporation process and strong dominance with the ratio of almost 1:2 of the exterior angle. The overall enhancement of the fluorescence signal and therefore the amount of counts happens occurs uniformly for both, exterior and interior signals.

Therefore it can be concluded that the spacial and angular distribution of the emission dipoles of R6G molecules shows the same ratio of signal intensities in both investigated systems. That means that the angular distribution of dipoles has seemingly no effect on the fluorescence enhancement. In order to understand the observed broadening of the signal and increase of the integral intensity a control experiment with drying of dye solution on a glass substrate was performed. The experimental set-up is the same as described on Figure 3.2 with only exception that the glue and AAO membrane were removed. Each mapping picture was reduced to an 1D pixel array. The integral and maximal intensities of every pixel array were plotted as a function of time (figure 5.6a). One can see that the integral and maximal intensities show similar behaviour. They both grow up to a certain normalized value and then rapidly fall after the solvent completely evaporated. The same evaluation method was applied to the experiments with AAO (figure 5.6b). During the first phase of evaporation that takes almost 25 seconds the dynamics resembles the one from a control experiment with a glass plate. After that

the integral intensity drops to almost zero and immediately regenerates to a value almost twice as high as right before the drop. The maximal intensity shows similar dynamics but different absolute values. There is a drop at the same moment of time as in the integral intensity.

5.4 Discussion

Based on the collected experimental data from the evaporation dynamics and dye distribution dynamics following conclusions can be made:

- The evaporation profile inside and outside (on top) of the AAO membrane is linear as shown in Figure 5.3.

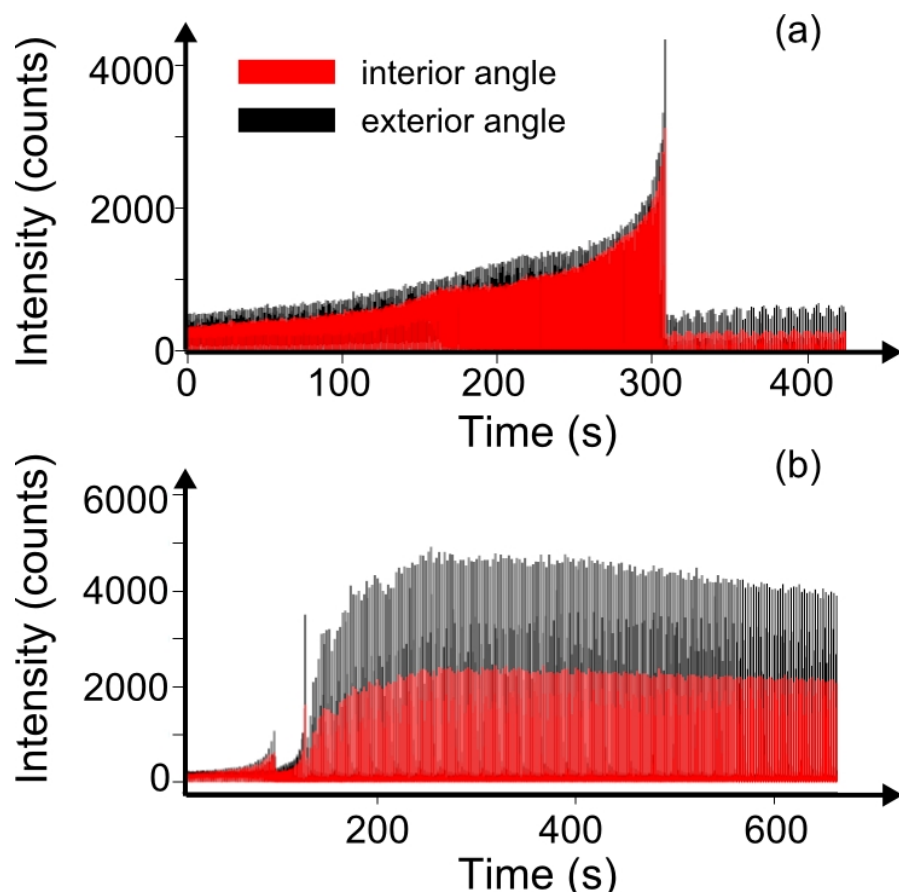


FIGURE 5.5: The distribution of the angles location of the dye molecules during the experiment. As part of the experiment you can define two types of polarization - polarization signals can be detected in the internal and external volume of the sensingseparating polarization into two classes.

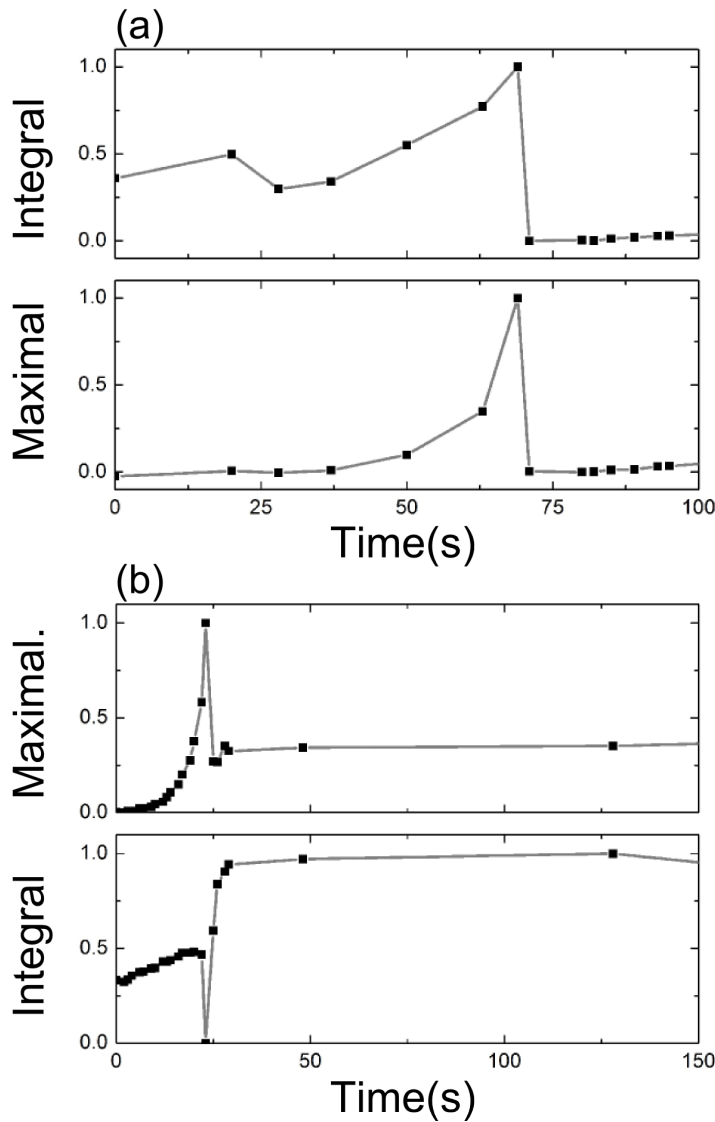


FIGURE 5.6: Normalized maximal and integral intensity during the evaporation of ethanol-R6G solution from a glass surface(a) and AAO membrane(b).

- The measured displacement rate inside AAO is almost twice as high as outside
- The behaviour of R6G inside AAO shows common features with the dynamics observed on the glass up to the moment, when the solvent evaporates completely. The maximal and integral intensities grow during the evaporation from glass surface due to the increase of the molecules density.
- The signal intensity reaches its maximum shortly before the disappearance of the solvent and falls to almost zero right after.

- There is a strong signal suppression and regeneration shortly after ethanol evaporates completely.
- Dipole orientation measurements show that there is no difference between R6G molecules on a glass surface and inside AAO. That means, 3D orientation of R3G molecules has no influence on the observed magnification of integral intensity and regeneration of the signal.

Figure 5.4III shows that there is a fluorescence signal distributed along the whole scanned area, which is not the case for region II that takes place while the solvent evaporates. At first glance it seems like the fluorescing molecules are redistributed along the whole volume of the pores with decreasing particle density (when interpreting the fluorescence signal literally) after the disappearance of the solvent. However, it is necessary to understand that the design of the experiment and the location and the role of the key elements play an important role. Figure 5.7 illustrates what might happen inside an AAO membrane during the phase III illustrated on Figure 5.4. After ethanol completely evaporates, all the R6G molecules are placed on the bottom of AAO. Being illuminated, they emit fluorescence signal that goes to a detector, which is placed below the AAO membrane, glass slice and glue layer. The position of a pixel that corresponds to a fluorescing point of a system, depends on the position of mechanical elements that move the focal area. In this case, the elements are placed that way that the focal area is focused on the bottom of AAO in z-direction, therefore one detects strong fluorescence signal from this layer.

One possible explanation to what happens in the case, when the focal area is above R6G molecules, on the top of the sample, is what can be called the "fluorescence echo", which is illustrated on Figure 5.7 c and d. The focal volume is located in the AAO membrane in such a way that AAO pore sections away from the pore bottom are illuminated that do not contain R6G molecules. The laser light is focused on the top of the membrane. Since the refractive index of AAO is above 1, the light is scattered by pore walls, so the scattered light propagates along the pores. AAO membrane acts as a waveguiding medium. The light reaches the bottom of the pores of AAO and excites R6G molecules, however the intensity of this excitation is much smaller than that from direct illumination, when light is focused directly on the bottom. This weak fluorescence signal reaches the detector. The position of mechanical element that moves the system in z-direction and the fluorescence signal from an actual bottom of the membrane is interpreted

by a software as if the top of the AAO membrane would emit fluorescence and is displayed that way (figure 5.7d) and Figure 5.4, phase III).

In case when the AAO membrane is filled with EtOH, like for instance on Figure 5.4 (phase II), there is no scattered radiation except that from the focal volume because of the lateral Propagation of the scattered light, which is caused because of the interface between air and evaporating EtOH. During the phase III there is no such interface and the scattered light moves radially into every possible direction. It is not possible to observe this process directly on a glass surface because there is no modulation of refractive index and therefore no internal reflection.

Let us consider in details to maximal and integral intensities that are displayed

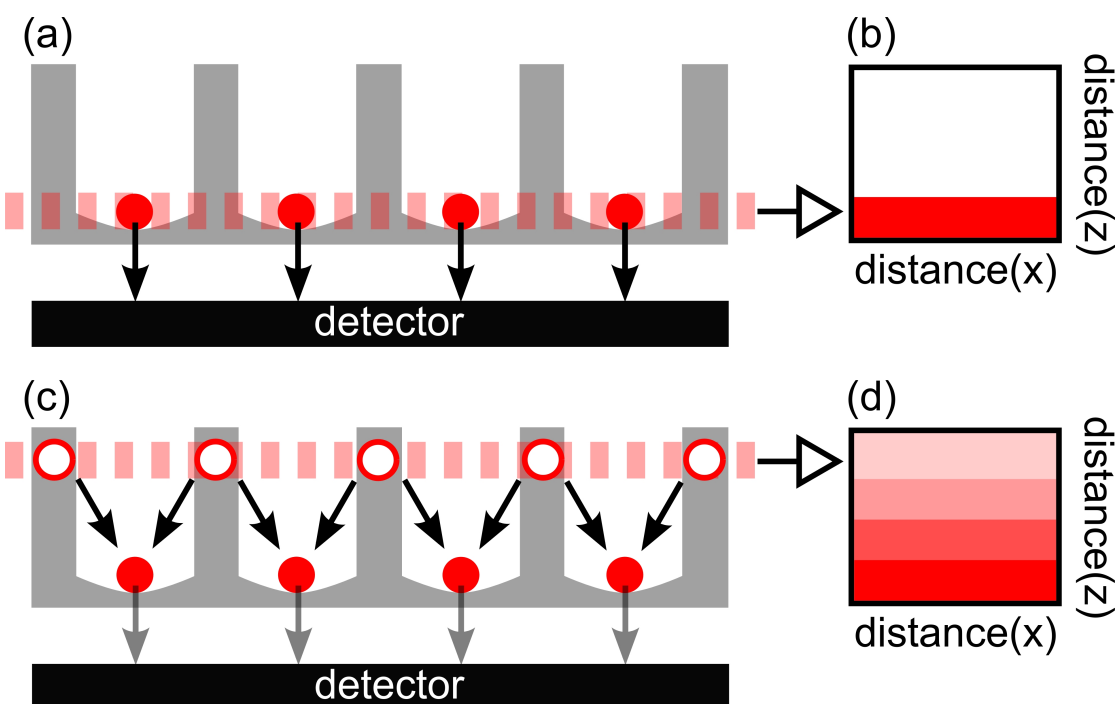


FIGURE 5.7: Illustration of the processes that takes place inside an AAO membrane after the solvent completely evaporated (not up to scale). (a) The red points on the bottom of AAO are R6G molecules. When they are directly illuminated with a laser light, so that a focal plane (red dashed horizontal line) is focused on the bottom of the membrane, they emit fluorescence signal that is registered by a detector, which is placed below. (b) The measured data is interpreted by software and fluorescence signal is displayed as function of the position of mechanical elements that move the system and change the focal plane in x- and z-direction. (c) The focal plane (red dashed horizontal line) has changed its position and is now above the bottom of AAO. The walls of AAO scatter laser light, the scattered light reaches the R6G molecules on the bottom, they emit fluorescence signal, which is then detected. (d) The position of mechanical element in z-direction is above the bottom of AAO, the software interprets the measured signal from the bottom of AAO, as if it came from the top and displays it on a wrong position as fluorescence "echo".

on Figure 5.6b.

In the case of maximal intensity, there is a growth up to a moment, when the solvent completely evaporates. This process is associated with the concentration of R6G molecules, which gets higher with decreased amount of ethanol, therefore there are more and more fluorescing molecules per volume. Then it is possible to observe a slight drop (which nature has not yet been understood) and regeneration of the signal to almost half of the maximal value. The integral intensity shows similar behaviour. It slightly grows up to a moment when the solvent disappears, which can be explained by better fluorescence conditions when the density gets higher. After the drop the integral intensity reaches much higher value, than before ethanol evaporated. This is linked to the "fluorescence echo" effect. When the intensities along the z-direction are summed, it is like one would multiply the fluorescence intensity from the bottom layer which leads to an increase in the overall intensity.

The last open question is the nature of the drop and regeneration of the signal that is observed several seconds after the complete evaporation. R6G, as every fluorescing substance, shows best fluorescence in surrounding medium, such as water or ethanol. When in a dry state, laser light is strongly scattered on the R6G crystals. Right after the disappearance of ethanol, the infiltrated R6G molecules are in a dry state, therefore it is possible to observe short drop that occurs in the transition from phase II to phase III on a Figure 5.4 and on a Figure 5.6b. It might be water that is absorbed from the surrounding air that plays a key role in the regeneration process, however this has to be proven in the further research. A. Penzkofe and W. Leupache [122] show that the fluorescence quantum efficiency drops significantly with a higher concentration, however it is still higher than that in the dry state.

5.5 Conclusion and outlook

Evaporation dynamics in AAO was studied with fluorescence mapping method, the same method that was applied to the evaporation dynamics from CPG. In contrast to CPG, the evaporation profile from AAO is linear, without any jumps and irregularities.

Besides it was possible to demonstrate the "fluorescence echo" effect that leads to a seemingly higher integral intensity during the evaporation experiment, after

the solvent completely evaporates. The "echo" effect is based on a fact that pore walls scatter laser light that reaches to bottom of AAO, where R6G are placed during the last phase of experiment. This secondary light leads to a fluorescence signal from the bottom that goes directly to a detector that is placed below the membrane. The system interprets this signal as if it came from the focal point and not from the real source, which is the bottom, and falsely displays this signal on a wrong position. Therefore, integral intensity after the disappearance of the solvent is in real multiplied fluorescence intensity from one single fluorescing layer, where R6G are physically placed.

An important conclusion that can be taken from this experiment, is the fact that each single CLSM experiment that is based on a fluorescence and scattering effect must be analysed very carefully, because the physical appearance of fluorescing substance and measured position of fluorescence signal do not always correlate, as had been shown in this experiment.

It is still necessary to understand the nature of fluorescence quenching and regeneration right after the complete evaporation of the solvent.

Chapter 6

Non-volatile liquid guests in nanoporous hosts: characterization by BLS spectroscopy

6.1 Introduction

While morphological and structural properties of bi-continuous hosts as well as the surface chemistry of their pore walls have extensively been probed by porosimetry, inverse gas chromatography and analytical spectroscopy, much lesser efforts have been devoted to the study of wave propagation through such disordered media. This lack of interest is mainly caused by the perception that, even if adsorption can be neglected, wave propagation is either hampered by Mie scattering (if the wavelength matches the characteristic feature size of the nanoporous medium) or by the fact that the wave simply probes an effective medium (if the wavelength is larger than the characteristic feature size of the nanoporous medium). The propagation of sound waves through nanoporous media and nanocomposites might be even more relevant than propagation of electromagnetic waves because phonon management underlies heat management as well as vibration management, thus determining the extent to which a material is noise-insulating or thermally insulating [123]. On the other hand, information acquired by probing sound propagation through a disordered medium may be complementary to information accessible by

classical characterization methods [124].

Within the framework of this thesis it has been shown that elastic waves may propagate through an isotropic nanoporous medium with bicontinuous morphology along different pathways even if the characteristic structural feature size of the porous medium is more than order of magnitude smaller than the phonon wavelength. In the case of isotropic nanoporous materials with characteristic features sizes smaller than the phonon wavelength the propagating phonons should probe an apparently homogeneous, effective medium. Hence, in phononic band diagrams a single acoustic mode should appear. As revealed by Brillouin light scattering (BLS) spectroscopy, hypersonic band diagrams of controlled porous glass (CPG) employed as nanoporous model medium and of CPG/poly(dimethylsiloxane) (PDMS) employed as model nanocomposite may show several acoustic modes even though all structural feature sizes were at least one order of magnitude smaller than the phonon wavelengths. Since the slopes of the acoustic modes correspond to sound velocities, the occurrence of more than one acoustic mode in the phononic band diagrams indicates that the medium trough which the phonons propagate provides a number of propagation pathways with differing elastic properties corresponding to the number of acoustic modes.

The PDMS infiltrated CPG membranes are a good model to investigate the nature of so called polymer interphases, the nature of which inside a porous matrix or surrounded by filler particles has been studied extensively with different experimental methods during the last two decades. The inter-phase is, as a name suggests, the phase or mostly the layer of PDMS that has strikingly different properties than the bulk material. It is a structure that exhibits restricted mobility and therefore different mechanical properties due to the interaction of the polymer molecules with the pore walls or surrounding filler particles.

Litvinov et. al. [125] has shown using ^2H NMR study that there is restricted motion near the surface of the filler particles for PDMS polymer chains. The thickness of restricted layer is considered to be about 0.8 nm. Kirst et. al. [126] investigated the linear trimethylsilyl terminated PDMS with broad band dielectric spectroscopy and was able to show, there are different degrees of interaction between PDMS chains and the filler surface. The kind of interaction can be divided into directly bound state, interfacial and nanoadsorbed layer. The thickness of nanoadsorbed layer that covers the surface uniformly is considered to be about 1nm, the thickness of a non uniform layer is 2.6 nm due to dense packing of filler particles. Tsagaropoulos et. al. [127] investigated PDMS filled with very fine silica

particles with dynamic mechanical study and was able to show that the interaction of polymer chains with very fine silica particles of high surface area restricts the mobility of the polymer chains and leads to the formation of tightly bound and loosely bound polymer, which leads to a new glass transition. Cosgrove et. al. [128] studied the adsorption of PDMS on silica with NMR relaxation and diffusion and showed, similar to the results from [126] that the structure of adsorbed polymers can be divided into three different states, such as bound polymer, free bulk polymer and the layer that is restricted by the surface. Evmenenko et. al. [129] used synchrotron X-ray reflectivity method to confirm the formation of immobilized layer of PDMS near silica surfaces. Fragiadakis et. al. [130] used thermally stimulated depolarization currents, broadband dielectric spectroscopy and differential scanning calorimetry to investigate the thickness of immobilized interfacial PDMS layer and found out that the thickness of this layer is between 2.1 and 2.4 nm with correlates with the results from other groups discussed above. Horn and Israelachvili [131] investigated the force between two molecularly smooth mica surfaces immersed in liquid PDMS and found out that the polymer has a viscosity equal to its bulk value, however there is a layer next to each surface only about one radius of gyration thick that does not slow, is completely immobilized.

All these experiments lead to two important conclusion - there is always an immobilized layer of PDMS in the presence of an oxidic surface and this layer is between 0.8 and 2.4 nm.

Up to now mostly silica was investigated, however, Sato et. al. studied phononic phenomena at gigahertz frequencies in self-ordered anodic aluminum oxide containing hexagonal arrays of cylindrical nanopores with submicron periodicity. Using high-resolution Brillouin spectroscopy Sato reported the first realization of directional flow of elastic energy parallel and perpendicular to the pore axes, phonon localization, and tunability of the phononic band structure [132]. As reported by Sato, a new phononic branch was observed in the PDMS filled AAO that seems to relate to the presence of thin interphase with enhanced elasticity, which is about 2 nm thick.

6.2 Results

The experimental setup is described in Section 3.3.2. Empty (filled with air) and PDMS infiltrated CPG membranes with average pore diameter of 2 nm, 9 nm and

26 nm where investigated. The CPG membranes are characterized in the corresponding Section 2.3.3. Figure 2.12 shows these membranes. PDMS was ordered from Sigma Aldrich, Mn=550 and is OH terminated.

The Brillouin spectra were measured for different scattering angles. In order to get maximal information about the structure, both, \mathbf{q} -parallel and \mathbf{q} -perpendicular configurations were measured (transmission and reflection geometries, see Figure 3.7). The same dispersion relations were observed in both configuration since there is no preferable direction in the CPG membranes because of the isotropic distribution of the porous network. Rayleigh scattering that occurs between -5 and 5 GHz was filtered out since it does not deliver any useful information for understanding the spectra. Only Stokes shifts are shown, because the Brillouin spectra are absolutely symmetrical due to the nature of the phenomenon. To determine the exact position of each peak Lorentzian approximation was used that was applied to the raw data.

Figure 6.1 shows **Brillouin shifts** for non infiltrated CPG membranes with average pore diameter of 2 nm, 9 nm and 26 nm. The exact position of each shift is marked with a semitransparent circle. The letter L denotes that the marked shift is longitudinal mode. More than one shift was measured, each is marked with a corresponding number. Both, \mathbf{q} -parallel and \mathbf{q} -perpendicular orientations are shown, but since there is no preferable or defined direction in the investigated samples, both orientations lead to the same dispersion diagram. The difference of intensities of L1 and L2 for CPG2 and CPG26 is more intense in the \mathbf{q} -perpendicular orientation. So is the resolution of L1 and L2 peaks for CPG26 - in \mathbf{q} -parallel orientation it seems like a one bright peak, in \mathbf{q} -perpendicular orientation one can see a peak and a hump. L2/3 looks like one bright peak in \mathbf{q} -parallel for CPG9 but one can differ to peaks in \mathbf{q} -perpendicular configuration. The intensity of L1 is higher than L2 for CPG2 and CPG26. Figure 6.2 illustrates the Brillouin shifts for infiltrated CPGs with average pore diameter of 2 nm, 9 nm and 26 nm. There are two peaks for 2 nm sample, the one that never changes its position (flatband, marked with gray area), and one that is dependent on the scattering angle (acoustic mode). The first peak can be considered as back scattering energy. The \mathbf{q} -perpendicular configuration shows only one peak for CPG2 and CPG9, however one can see two shifts for CPG26.

As one can see on both Figures 6.1 and 6.2, the \mathbf{q} -parallel spectra differ significantly from the \mathbf{q} -perpendicular spectra even for the same scattering angles. As explained in the end of Section 3.3, \mathbf{q} -parallel corresponds to a transmission mode

and \mathbf{q} -perpendicular to a reflection mode. The reason for such a discrepancy of the spectra regarding their maximal intensity and the overall appearance might be the fact, that the initial intensity of the incident light is reduced in the reflection mode due to reflection and scattering of light on the rough surface of CPG. The roughness of studied CPGs is shown in Figure 2.12 a, b and c. Figure 6.3a shows dispersion relations for non-infiltrated 2 nm, 9 nm and 26 nm CPGs. The presence of more than one longitudinal mode for each empty sample leads respectively to more than one dispersion curve. Based on the dispersion diagram it is possible to calculate the sound velocity, therefore each longitudinal or transversal branch is designated as C_L or C_T . The measured Brillouin shifts for transversal modes are not shown. There is only one transversal mode for CPG2 but two modes for CPG9 and CPG26. The calculated longitudinal sound velocities, transversal sound velocities and refractive indices for each measured mode for CPG2, CPG9 and CPG26 are shown in Table 6.1. Figure 6.3b shows the dispersion diagrams for filled CPGs. There is only one longitudinal sound velocity for 2 nm and 9 nm samples and two sound velocities for 26 nm sample. There is also one transversal sound velocity for CPG2 and CPG26, it was not possible to measure transversal sound velocity for CPG9.

TABLE 6.1: Longitudinal and transversal sound velocities and calculated refractive indices (longitudinal mode) for investigated non infiltrated CPGs.

Sample Name	Longitudinal Velocity $\frac{m}{s}$	Transversal Velocity $\frac{m}{s}$	Refractive Index
CPG2	$C_{L1} = 3940$ $C_{L2} = 2900$	$C_T = 2360$	$n_1 = 1.41$ $n_2 = 1.22$
CPG9	$C_{L1} = 4120$ $C_{L2} = 3180$ $C_{L3} = 2920$	$C_{T1} = 1980$ $C_{T2} = 1810$	$n_1 = 1.37$ $n_2 = 1.23$ $n_3 = 1.19$
CPG26	$C_{L1} = 3910$ $C_{L2} = 3470$	$C_{T1} = 2420$ $C_{T2} = 2140$	$n_1 = 1.22$ $n_2 = 1.19$

TABLE 6.2: Longitudinal and transversal sound velocities and refractive indices (longitudinal mode) for investigated infiltrated CPGs.

Sample Name	Longitudinal Velocity $\frac{m}{s}$	Transversal Velocity $\frac{m}{s}$	Refractive Index
CPG2	$C_L = 4280$	$C_T = 2440$	$n = 1.37$
CPG9	$C_L = 3000$	C_T n.a.	$n = 1.27$
CPG26	$C_{L1} = 3460$ $C_{L2} = 2780$	$C_T = 1780$	$n = 1.35$

The calculated longitudinal sound velocities, transversal sound velocities and refractive indices for infiltrated 2 nm, 9 nm and 26 nm samples are summed up in Table 6.2

6.3 Discussion

6.3.1 Mode-guiding vs. effective medium

The phonon band structures of empty CPG membranes show common features for all examined pore diameters, both longitudinal (hard and soft mode) and transversal (two modes with increasing distance when pore diameter increases). Experiments on blank CPGs revealed the presence of two phononic modes in the BLS spectra for 2 nm and 26 nm samples and three modes for 9 nm spectra (see Figure 6.1). That leads to the conclusion that there are simultaneously different ways, how the sound wave propagates through the empty membranes, which leads to multiple measured sound velocities (Figure 6.3a). The measured phononic modes are called **the hard mode L₁** (higher frequency, higher sound velocity) and **the soft mode L₂** (lower frequency, lower sound velocity). In case of 9 nm samples, an optimal correlation between raw data and fitting curve is found, when suggesting the presence of two soft modes, even though their distance in the frequency space is minimal. The model that would explain the presence of soft mode and hard mode is based on an assumption that two different ways of how the sound propagates through the sample are observed at the same time (Figure 6.5) - the guiding of the sound waves selectively through the pore walls and therefore the higher sound velocity for the hard mode L₁ and the passing of the sound wave through the whole sample as an effective body including the air filled empty spaces and therefore the averaging of the sound velocity, which leads to a smaller value for the soft mode L₂. This is possible since there is a significant difference between the speed of sound in air, which filled the empty membrane, and the speed of sound directly inside the walls of the porous glass.

CPGs with 2 nm and 26 nm average pore diameter have a clearly outlined hard mode (peaks at higher frequency) and weakly outlined soft mode (peak at lower frequency). 9nm CPG shows an opposite behaviour - the intensity of the hard mode is lower than the intensity of the soft mode. For some reason the presence

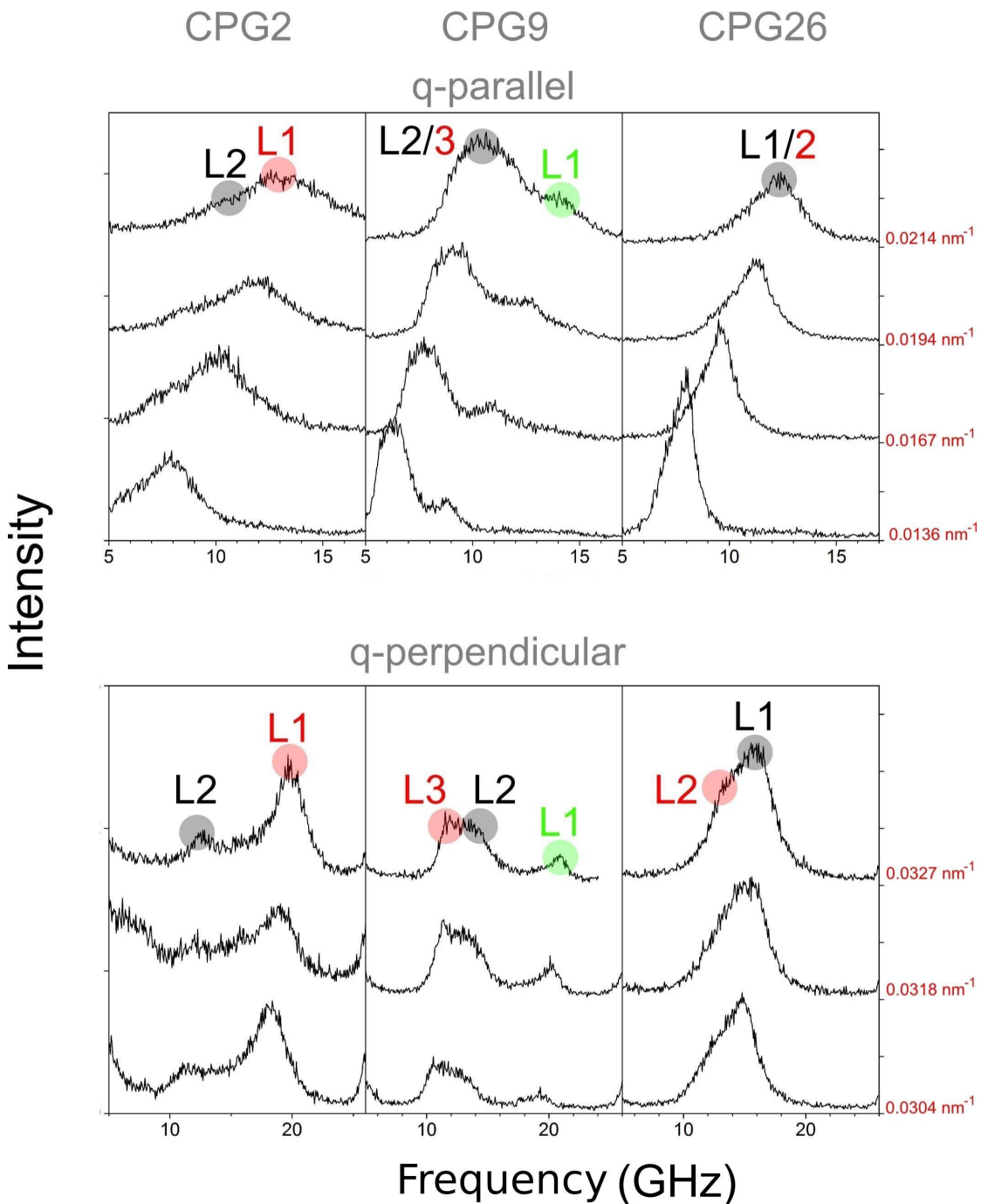


FIGURE 6.1: Measured Brillouin shifts for empty 2 nm, 9 nm and 26 nm CPG samples. The letter L denotes a peak that corresponds to a longitudinal mode. Spectra are shown for parallel (top) and perpendicular (bottom) orientation of \mathbf{q} -vector. Semitransparent circles illustrate the location of the maxima that are determined with the Lorentzian approximation. Rayleigh scattering is filtered out and only Stokes shift is shown due to the symmetry of the BLS effect. The spectra are taken with VV polarization and represent the longitudinal mode. The corresponding value of \mathbf{q} -vector of each spectrum is shown in red on the right side. The frequency corresponds to the Brillouin Shift.

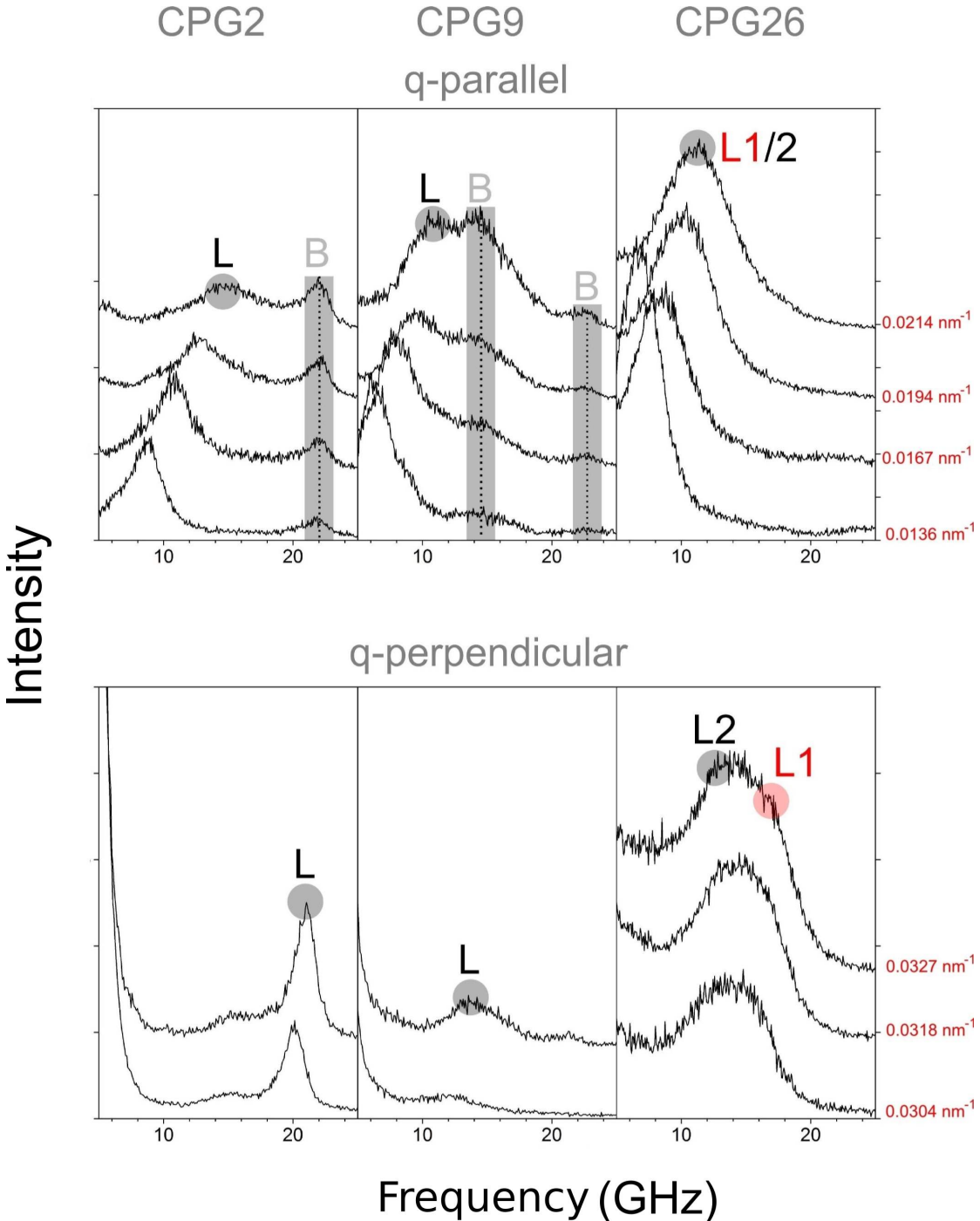


FIGURE 6.2: Measured brillouin shifts for infiltrated 2 nm, 9 nm and 26 nm CPG samples. The letter L denotes a peak that corresponds to a longitudinal mode. The letter B denotes the backscattering peak that does not change its position with the changing angle configuration. Spectra are shown for parallel (transmission geometry) and perpendicular (reflection geometry) orientation of \mathbf{q} -vector. Semitransparent circles illustrate the location of the maxima that are determined with the Lorentzian approximation. Rayleigh scattering is filtered out and only Stokes shift is shown due to the symmetry of the BLS effect. The spectra are taken with VV polarization and represent the longitudinal mode. The corresponding value of \mathbf{q} -vector of each spectrum is shown in red on the right side. The frequency corresponds to the Brillouin Shift

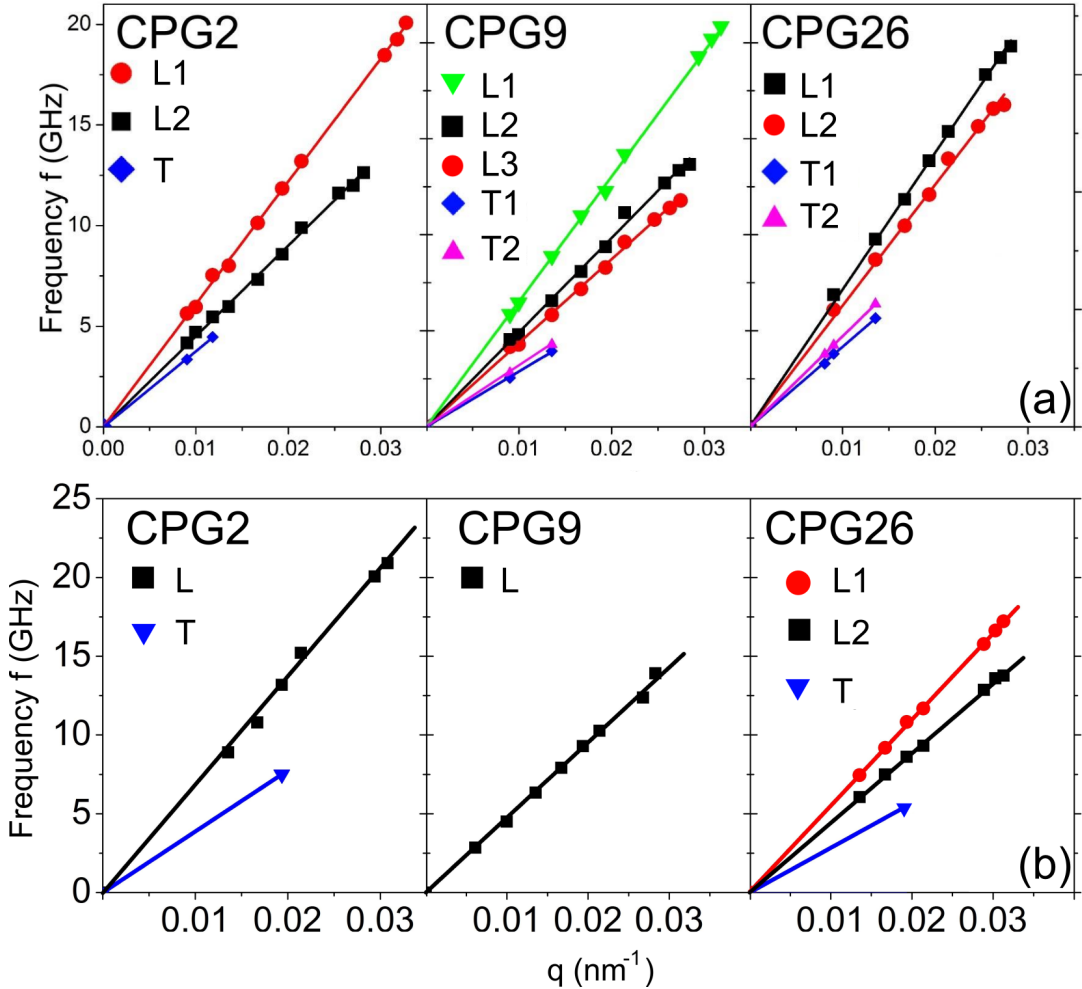


FIGURE 6.3: Dispersion relations for non infiltrated and infiltrated 2 nm, 9 nm and 26 nm CPG samples. (a) Longitudinal (C_L) and transversal(C_T) modes are presented. Each sample has several longitudinal modes. CPG2 and CPG26 have two transversal modes respectively. (b) Longitudinal (C_L) and transversal(C_T) modes are presented. Each sample has several longitudinal modes. CPG2 and CPG26 have two transversal modes respectively.

of weak modes for 2 nm and 26 nm samples is particularly noticeable in the \mathbf{q} -perpendicular configuration when directly compared with the data obtained from the \mathbf{q} -parallel configuration, even though CPG is an isotropic medium and there should be no difference. Figure 6.4 shows that the intensity ratio of the hard modes and soft modes as a function of scattering angle is constant for all three samples. The intensity ratio was calculated as I_1/I_2 where I_1 is the intensity of the hard mode and I_2 the intensity of the soft mode. The constancy of the ratio of intensities means that it does not depend on the scattering angle and that it is a fundamental property of the samples related to their internal structure. The fact that the CPG9 has more intense soft mode and less intense hard mode leads

to a lower value of I_1/I_2 compared to the samples with 2 nm and 26 nm average pore diameter. This does not correlate with the porosity values listed in Table 2.1, which grow with increasing pore diameter. For PDMS infiltrated CPG2

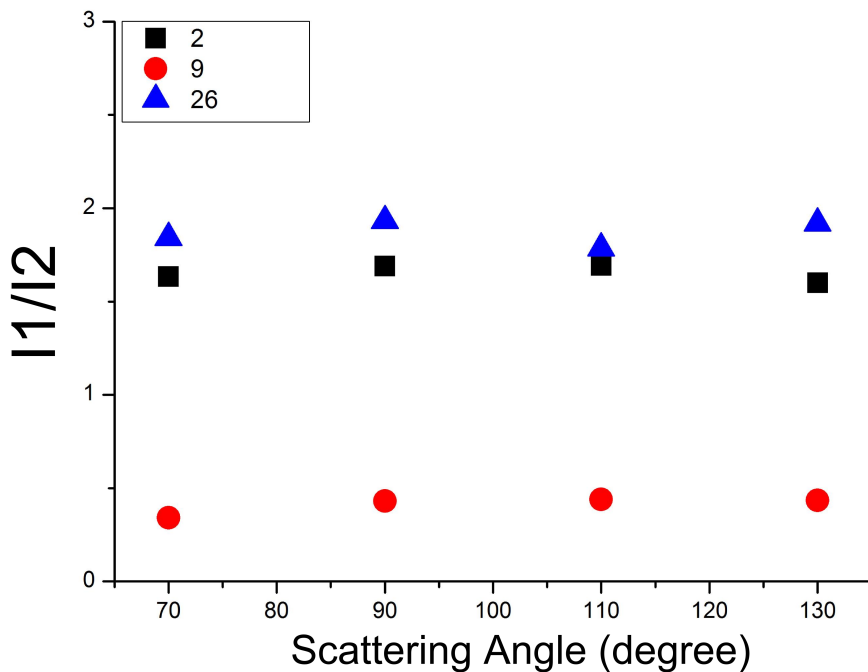


FIGURE 6.4: Ratio of measured values for longitudinal Brillouin shifts L_1 and L_2 for empty CPGs as function of the scattering angle reveals certain stability. CPG2 nm and CPG26 nm exhibit the stable dominance of the L_1 over L_2 whereas the CPG9 nm shows exactly the opposite result - there is a stable dominance of L_2 over L_1

and CPG9 samples there is only one sound velocity, which means that only the effective sound velocity is observed - the whole CPG membrane acts like an effective medium and there is no mode-guiding effects like it was observed inside empty CPGs due to the low elastic contrast between the pore walls and infiltrated polymers. Figure 6.6 illustrates the idea of selective propagation and low elastic contrast. When elastic contrast is to high, like in case with glass-air, there is a component of the sound wave that prefers pathways with higher elastic modulus and propagates strongly along the glass walls, which leads to a hard mode L_1 observed for empty CPGs. When a medium is present, like observed in the case of filled membranes with 2 nm and 9 nm pore diameter, the body acts like a bulk, there is no preferable direction and the sound waves propagate along the whole body.

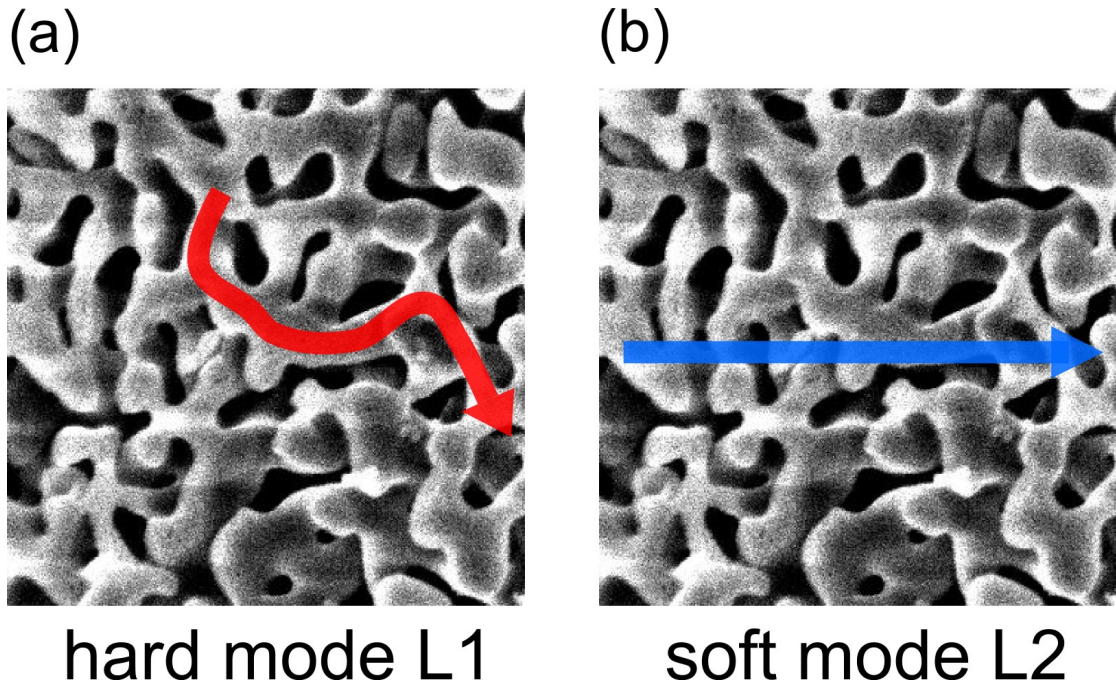


FIGURE 6.5: Modeguiding vs. Effective Medium model, (a) the propagation of the sound wave selectively through the pore walls leads to a higher sound velocity for the hard mode L1 and (b) the passing of the sound wave through the whole sample leads to the averaged sound velocity of an effective medium which leads to a lower value for the soft mode L2. The length of the edge is 350 nm

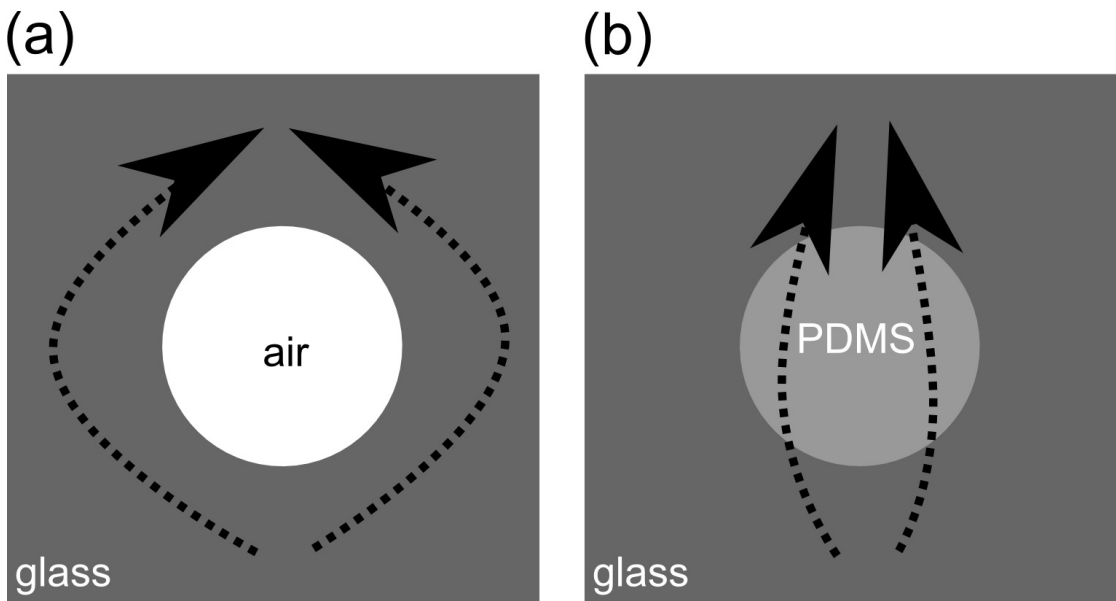


FIGURE 6.6: Illustration of the principle of selective propagation of sound waves in non-infiltrated(a) and infiltrated(b) CPG membranes. The sound wave prefers selectively material with a higher elastic modulus.

6.3.2 Sound velocity inside pore walls

Polian et. al. [133] investigated SiO₂ with BLS spectroscopy for different temperatures and have shown that the longitudinal sound velocity of bulk silica glass at room temperature is $v_l(SiO_2) = 5953 \frac{m}{s}$. Assuming that the hard mode is the sound that propagates through the pore walls, one would suggest that the sound velocity might not differ significantly from that in bulk, however, maximal measured longitudinal sound velocity for CPG sample is $4120 \frac{m}{s}$ for CPG9 nm. There must be something that slows down the sound velocity that propagates through the pore walls. An ad hoc assumption implies that the inner structure of the pore walls can be described with a density gradient. CPG membranes used in the experiments consist 96% of SiO₂ and the rest are residual boron atoms (see [4]). Dawidowicz et. al [134] has shown that when heating the sample up to 400° boron atoms start to diffuse to the surface, however their spacial distribution in the non heated sample is unknown. As Ryabov et. al. summarizes in his work [135], it has been also shown with neutron diffraction study [136] that there are three types of adsorbed water inside silica glasses. The first type is physisorbed layer, the second type is a chemically stable chemisorbed layer that is characterized by spatially distributed water molecules on the inner surface of porous silica glass and the third type is a strongly bonded chemisorbed layer that consist of water clusters made of 40-60 molecules that are connected with hydrogen bonds and are forming an ordered array of water molecules.

The chemical structure of the surface of the porous glass is characterized by the presence of hydroxyl groups [137]. In addition, the chemical composition of the surface can vary considerably depending on the conditions under which the thermal pre-treatment was carried out [4]. Thus it appears that the internal structure of pore walls of the porous glass is a chemically complex structure consisting of two main layers -the silica glass layer with some inhomogeneities, like boron atoms and the rest, and uniformly distributed water layer of three different types.

6.3.3 Comparison of sound velocities of infiltrated and non-infiltrated CPGs

Now after discussing the possible origin of multiple sound velocities in empty CPG membranes, one can directly compare the longitudinal and transversal components of PDMS infiltrated and empty CPGs.

6.3.3.1 CPG2

The longitudinal sound velocity of the empty CPG sample is L1=3940 m/s and L2=2900 m/s, and the sound velocity of the PDMS filled CPG sample is 4280 m/s. That means, longitudinal waves propagate inside PDMS filled CPG2 340 m/s faster than in the empty CPG2 membrane when compared to the hard mode L1 and 1380 m/s faster than in the empty CPG2 membrane when compared to the soft mode L2 . The empty **transversal** sound velocity is 2200 m/s, the filled **transversal** sound velocity is 2440 m/s. That means, transversal waves propagate inside PDMS filled CPG2 220 m/s faster, than in the empty CPG2 membrane. One possible explanation of this effect is the immobilization of the PDMS layer that will be discussed below .

6.3.3.2 CPG9

The longitudinal sound velocities of the empty CPG9 sample are L1=4120 m/s, L2=3180 m/s and L3=2920 m/s, the **longitudinal** sound velocity of the PDMS filled CPG9 is 3000 m/s. The transversal component of PDMS filled CPG9 was not measured, direct comparison is not possible.

Let us assume, based on the mode-guiding model that L1 is the strong mode, which means this is the sound velocity inside the pore walls and L2 and L3 are two soft modes, which means these are the sound velocity of the effective medium. Comparing L_{1empty} with L_{filled} leads to a difference of 1120 m/s. The sound waves propagate more than 1000 m/s faster inside the walls of the empty samples than in the effective medium of the infiltrated one.

Comparing L_{2empty} with L_{filled} leads to a small difference of 180 m/s, the sound inside the empty membrane is still faster.

Comparing L_{3empty} with L_{filled} leads to a difference of 80 m/s, the sound inside the empty membrane is **slower**. It is a similar result to the CPG2 filled. There might be a thin layer of immobilized PDMS molecules near the pore walls, leading to the increase of the sound velocity of the effective medium (L_{filled}) compared to the sound velocity of empty effective medium L_{3empty} .

6.3.3.3 CPG26

The longitudinal sound velocities of the empty CPG26 sample are L1=3910 m/s, L2=3470, the longitudinal sound velocities of the PDMS filled CPG26 sample are L1=3460 m/s, L2=2780. The empty **transversal** sound velocity is T1=2110 m/s, T2=2140, the filled **transversal** sound velocity is 1780 m/s.

This time there are two longitudinal components in the infiltrated sample. Even in the infiltrated state it was possible to measure both components.

Comparing L1_{empty} with L1_{filled} leads to the difference of 450 m/s. The sound inside the walls of the empty membrane is faster.

Comparing L2_{empty} with L2_{filled} leads to the difference of 690 m/s. The sound inside the effective medium of the empty membrane is much faster than that in the infiltrated one. In contrast to CPG2 and CPG9, every measured longitudinal sound velocity in infiltrated state is lower than in non-infiltrated. The same is valid for the transversal sound velocity T_{filled} compared to T1_{empty} and T2_{empty}.

6.3.4 Restricted mobility of PDMS infiltrated in CPG

The measured longitudinal sound velocities of PDMS infiltrated CPG2 and CPG9 are higher than longitudinal velocities of empty CPG2 and CPG9 (hard modes). In case of CPG26, every measured sound velocity in the empty samples is higher than in the PDMS infiltrated.

As discussed in the state of the art, it was shown with different experimental methods that there is a restricted motion of PDMS molecules near different surfaces, like the surface of the filler particles or on different surfaces. The thickness of this layer varies between 0.8 and 2.4 nm.

The molar mass of one monomer unit of PDMS is $M = 74,15 \text{ g/Mol}$. The number average molar mass of PDMS used in the experiments is $M_n = 550 \text{ g/Mol}$. That means, there are $550/74,15 \approx 7$ monomer units in a chain.

Assuming the length of a monomer unit as 4 Å one can easily calculate the average length of a chain as $L = N * l = 2,8 \text{ nm}$.

The length of a chain is about 3 nm and the pore diameter of CPG2 is 2 nm so it is most probably that every single polymer chain will have at least one adsorption site, which reduces the mobility of the chains.

The speed of sound can be given by Newton Laplace equation([138]), which is:

$$c = \sqrt{\frac{K_s}{\rho}} \quad (6.1)$$

where K_s is the stiffness coefficient and ρ is the density. One can assume that since PDMS is immobilized due to the massive increase of adsorption sites, its resistance to uniform compression also increased, leading to a higher value of K_s . That leads to a higher value of sound velocity that is observed in the BLS experiments. The same applies in some way for the 9 nm samples, since it was still possible to measure restricted motion of PDMS that is infiltrated into these samples, which manifests itself through higher sound velocity in infiltrated state, than the sound velocity of empty effective medium.

6.4 Conclusion and outlook

Empty and PDMS infiltrated CPG membranes with different mean pore diameter were investigated using BLS spectroscopy. It has been shown that there might be a mode-guiding effect in the empty CPG membrane, due to the presence of multiple phononic branches. The postulated model suggests that there are two different ways how the sound waves might propagate through the CPG membranes - the sound propagation through the glass and air as an effective medium that leads to a lower sound velocity and the selective propagation through the pore walls that leads to a higher sound velocity. This effect of selective propagation of sound waves porous glasses has not been observed up to now.

Investigations of PDMS infiltrated CPG membranes revealed two phenomena. First, one can measure only one sound velocity, which supports the theory of mode-guiding for the empty membranes, since the elastic contrast between pore walls and PDMS is lower, and therefore there is only effective medium that is visible for the pressure waves. Second effect is the higher effective sound velocity in infiltrated 2 nm CPG membranes that could only be explained by strong reduction of the mobility of infiltrated polymers. The effective sound velocity of infiltrated 2 nm CPG is 340 m/s higher, than the maximal sound velocity of empty 2 nm membranes. That means the sound velocity in the PDMS filled area must be higher than that in the pore walls, so the whole sound velocity is higher. The most simple explanation is the fact that the polymer chains are constantly

in contact with pore walls, since the average diameter of the pore walls is 2 nm and the average length of the chain about 3 nm. The specific interaction of the pore walls and PDMS molecules reduces the mobility of polymers, changing their elastic properties, such as sound velocity.

Chapter 7

Self diffusion of non-volatile fluids in quasi one-dimensional confinement

7.1 Introduction

Self diffusion coefficient of polymer molecules is a fundamental property in polymer dynamics. Therefore, this quantity has often been investigated, mainly with destructive methods, such as PFG-NMR ([139],[140]). Measurements of low diffusion coefficients at room temperature for relatively high chain length is not an easy task. Especially when it comes to the dynamics inside different nanoporous materials such as anodic aluminium oxide. Standard methods can not measure the diffusion coefficient in this system due to a very long observation time. Here a method is presented that allows to determine the diffusion coefficient of different non-volatile fluorescing substances inside AAO. This method is not destructive. It is based on the bleaching of fluorescing molecules in a certain area and observing of regeneration of fluorescence intensity in this area due to the molecular motion. It must be mentioned that this chapter has an explorative character. The theoretical and experimental methods presented here must be proven, controlled and optimized. The basis of the proposed method is fluorescence recovery after photobleaching (FRAP). It is a widely used optical method in the biology and biochemistry ([141], [142], [143]). Using this technique one can easily quantify diffusive properties of fluorescing probes. This method is widely established and

well understood for two-dimensional diffusion processes.

Axelrod et. al [144] proposed a model for uniform circular disc profile, D. M. Soumpas. [145] expanded this model, K. Braeckmans et. al. [141] and [146] has developed a model for 3D diffusion in a living cells. There is however no model describing one dimensional diffusion that would describe self-diffusion of polymers in a quasi one-dimensional environment of AAO. A theoretical and experimental model was created in order to investigate the diffusion process of polymers under nano-confinement of AAO.

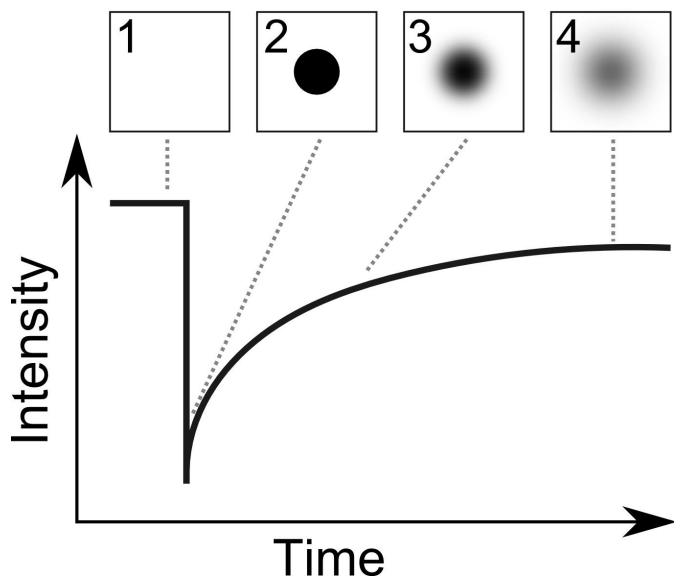


FIGURE 7.1: Different phases of regeneration during a FRAP experiment. (1) A non-bleached area is shown with a maximal intensity. (2) The same area is shown right after the photobleaching, resulting in a black circle that represents the ideal case, when all fluorescing molecules are bleached. The fluorescence intensity drops to a minimal value. (3) The bluring of the black circle is observed, which means there is a diffusion between bleached and non-bleached molecules. The fluorescence intensity starts to grow. (4) The process of regeneration continues, the fluorescence intensity in the photobleached area keeps growing.

7.2 Modification of the mathematical model of Fluorescence Recovery After Photobleaching (FRAP) method for one dimensional geometries.

A certain volume of the substance with the initial fluorescence intensity I_0 (Figure 7.1 [1]) is bleached by intense laser radiation, wherein the laser pulse duration should be shorter than the characteristic time of the system dynamics. This creates an area of photobleached molecules (Figure 7.1 [2]), resulting in a substantial reduction in intensity in a given volume. The intensity regeneration (Figure 7.1 [3]) is observed with a second laser, or with the initial one with significantly reduced radiation intensity to prevent further photobleaching. The recovery process takes place due to the natural diffusion of photobleached and non-photobleached molecules. The observation of the signal happens using confocal laser scanning microscope. The intensity at the end of restoration process (Figure 7.1 [4]) I_{end} is smaller than the initial intensity I_0 because the total amount of fluorescence capable molecules has decreased. Based on the recovery dynamics, expressed in the "Fluorescence Intensity vs. Time" graph, one can elucidate basic diffusion parameters such as the average diffusion time, the average distance, as well as generally characterize the investigated substance [142]. In addition, based on the nature of observed recovery profile one can conclude about the nature of the recovery itself - is it a pure diffusion, or is there other phenomena. One needs a mathematical model in order to extract the parameters from the experimental data.

Modeling fluorescence recovery implies two important points - **creating a mathematical model** and **parametrization of the model using computer algorithms**. The diffusion process inside porous alumina can be considered as quasi-onedimensional because of the geometrical restriction of this materials. The pores are parallel, non interconnected and the pore diameter is much smaller than the membrane thickness, which is well illustrated in Figure 7.2 that shows the underlying geometry for 1D modelling. The pore diameter of the AAO membranes used for the further experiments is 60nm and the bleached area is about 10 μm , therefore there are more than 300 pores in the bleached are. In order to calculate the diffusion coefficient from the 1D model, it is enough to know the intensity from the middle of the burned profile in x-z direction, which might be one single pore

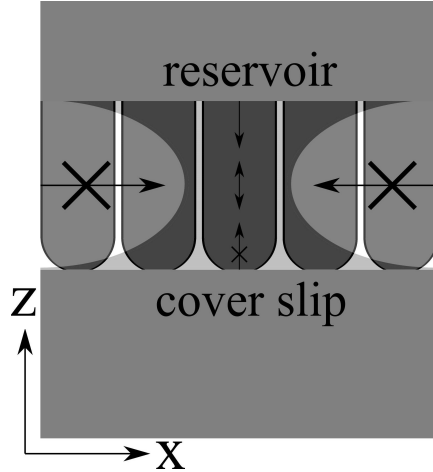


FIGURE 7.2: The underlying geometry of porous alumina with infiltrated and photobleached material. On the top there a reservoir of polymers. The pores are opened on the one side (top) and closed on the other (bottom).

in the ideal case.

Diffusion can be written in the form of a partial differential equation as the sum of a source function and the local derivative of the mass flow.

$$\frac{\partial C(x, t)}{\partial t} = f[C(x, t)] - \frac{\partial}{\partial x} J_c(x, t) \quad (7.1)$$

The bleaching is irreversible, so there is no source function in the considered system, so $f = 0$. In general, the mass flow of a sample surface is proportional to the concentration gradient (first Fick's law):

$$J_c(x, t) = D_x \cdot \nabla C(x, t) \quad (7.2)$$

With one dimensional system it is possible to reduce the gradient to the first spacial derivation and a factor D_x which is the proportionality factor which is in this case the diffusion coefficient. The equation 7.1 is reduced to:

$$\frac{\partial C(z, t)}{\partial t} = D_z \frac{\partial^2}{\partial z^2} C(z, t) \quad (7.3)$$

The first assumption is that the photobleaching process, i.e. conversion of the fluorophore to the nonfluorescent state is a first order reaction. The rate constant is defined as $\alpha I(r)$, the concentration of fluorescing molecules is $C(r, t)$, r is the position and t is time. Then one can define a differential equation that describes

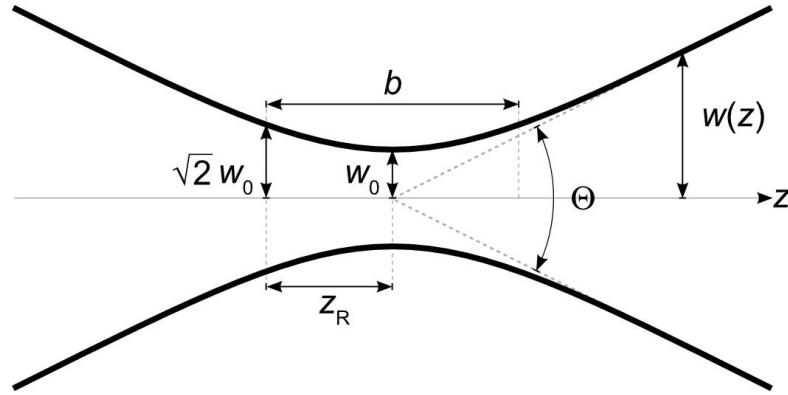


FIGURE 7.3: Gaussian beam width $w(z)$ as a function of the distance z along the beam. w_0 : beam waist; b : depth of focus; z_R : Rayleigh range; Θ : total angular spread [147]

the bleaching dynamics:

$$\frac{dC(r, t)}{dt} = -\alpha I(r)C(r, t) \quad (7.4)$$

which means the change of the concentration is linearly correlated to the concentration itself. The rate constant $\alpha I(r)$ consist of the factor α and the bleaching intensity $I(r)$. The initial boundary condition, describing the number of bleached molecules is determined using the fact that the initial laser pulse lasts much less than the dynamics of the system recovery.

$$C(r, 0) = C_0 e^{-\alpha T I(r)} \quad (7.5)$$

with T - the time interval of the initial pulse and C_0 - the initial concentration of activated fluorophores before bleaching.

The bleaching intensity $I(r)$ is defined by the Gaussian intensity profile of the laser beam, which is shown on Figure 7.3. Some important parameters are shown, such as the beam waist w_0 , $w(z)$ the beam width as a function of the distance z along the beam, b - the depth of focus, z_R - the Rayleigh range, Θ - the total angular spread, and z - the propagation direction.

The intensity of the beam at the point z in the distance r from the axis of propagation is:

$$I(r, z) = I_0 \left(\frac{w_0}{w(z)} \right)^2 \cdot e^{-2\left(\frac{r}{w(z)}\right)^2} \quad (7.6)$$

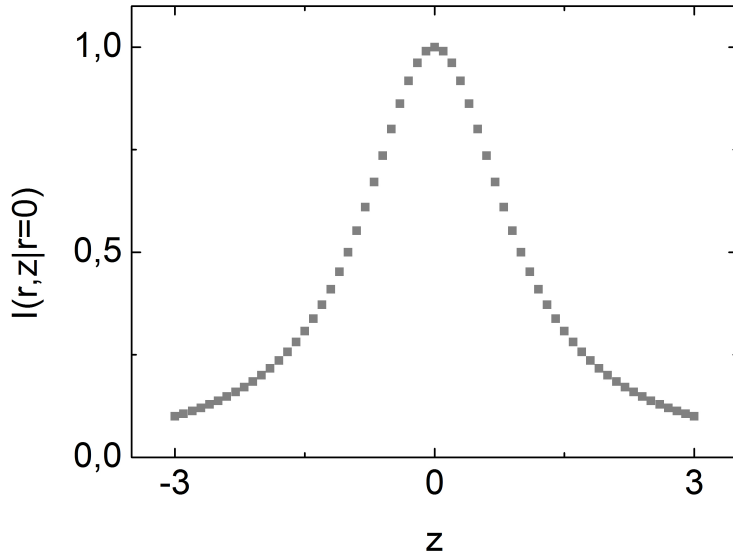


FIGURE 7.4: The intensity of the laser beam along the propagation axis z , for $z_0 = 1$ and $I_0 = 1$.

The initial intensity I_0 can be written as:

$$I_0 = \frac{2P}{\pi w_0^2} \quad (7.7)$$

where P is the total power of the laser beam. The Gaussian beam width can be expressed as:

$$w(z) = \sqrt{w_0^2 \cdot \left(1 + \left(\frac{z}{z_0}\right)^2\right)} \quad (7.8)$$

We now consider the intensity of the laser beam along the propagation axis only. In this case, Equation 7.6 can be simplified to:

$$I(r, z|r=0) = I_0 \cdot \frac{1}{1 + \left(\frac{z}{z_0}\right)^2} \quad (7.9)$$

The intensity along the propagation axis z for $I_0 = 1$ and $z_0 = 1$ can be seen on Figure 7.4.

The fundamental solution for Equation 7.1 is the so called heat kernel or diffusion propagator:

$$H(z, t) = \frac{1}{\sqrt{4\pi Dt}} \cdot \exp\left(\frac{-z^2}{4Dt}\right) \quad (7.10)$$

The particular solution of the diffusion equation can be found by folding the fundamental solution with initial conditions:

$$C(z, t) = C(z, 0) * H(z, t)C(z, t) = \int_{\mathbb{R}} H(z - \tau, t) \cdot C(\tau, 0) d\tau \quad (7.11)$$

Subsequently, the quasi one-dimensional diffusion model is used to study the self diffusion of polymers in the porous alumina. We examine only the membranes, which are open on one side (see Figure 7.2).

The particular solution has to be modified based on the system with only one opening. To do this, we introduce additional boundary condition. The mass flow at the bottom of the membrane must be zero. This is illustrated by the Neumann boundary condition. It is possible to implement, because the function of the initial condition is even throughout the real space.

$$C(z, t) = \int_0^{\infty} (H(z - \tau, t) + H(z + \tau, t)) \cdot C(\tau, 0) d\tau \quad (7.12)$$

The initial condition has the zero point in the focus of the laser beam. That does not match the zero point of the fundamental solution. Due to the Neumann boundary condition, we set the zero point on the underside of the membrane. The function of the initial condition needs to be shifted, which is represented by the parameter z_m .

$$C(z, t) = \int_0^{\infty} (H(z - \tau, t) + H(z + \tau, t)) \cdot C(\tau - z_m, 0) d\tau \quad (7.13)$$

Now we use the terms for the initial condition and the fundamental solution:

$$C(z, t) = \frac{C_0}{\sqrt{4\pi Dt}} \int_0^{\infty} \left(\exp\left(\frac{-(z - \tau)^2}{4Dt}\right) + \exp\left(\frac{-(z + \tau)^2}{4Dt}\right) \right) \cdot \exp(-\alpha T I(\tau - z_m)) d\tau \quad (7.14)$$

Using Equation 7.9 one can write:

$$C(z, t) = \frac{C_0}{\sqrt{4\pi Dt}} \int_0^{\infty} \left(\exp\left(\frac{-(z - \tau)^2}{4Dt}\right) - \exp\left(\frac{-(z + \tau)^2}{4Dt}\right) \right) \cdot \exp\left(\frac{K}{1 + \left(\frac{\tau - z_m}{z_0}\right)^2}\right) d\tau \quad (7.15)$$

Equation 7.15 describes the concentration along the beam axis at the point z and time t during the regeneration process. A new parameter K is introduced, which

is the product of three parameters α , I_0 and T . Combining the three parameters in one simplifies the task of modelling, because now we only need to determine a value of the parameter K . This parameter determines the degree of bleaching of the fluorophores. This value is easy to quantify, since photobleaching is the first order process and follows an exponential decay. Therefore, as it is possible to determine by measuring the intensity of the signal immediately before and after photobleaching:

$$K \approx -\ln \left(\frac{C(0)}{C(-T)} \right) \quad (7.16)$$

The problem is reduced to find suitable parameters for Equation 7.15 that correspond to the maximum correlation with the experimental data. The solution of this equation and the search for the required parameters is done using numerical methods.

7.3 Algorithmic parameterization and search for parameters

Equation 7.15 is the product of two functions, the first is a function of the inverse root of time, the second is an integral function, which in turn consists of the external and internal functions.

For further numerical solution of this equation we write it in the form of:

$$C(z, t) = \frac{C_0}{\sqrt{4\pi Dt}} \int_0^\infty T(z, t, \tau) d\tau \quad (7.17)$$

with

$$T(z, t, \tau) = \left(\exp \left(\frac{-(z-\tau)^2}{4Dt} \right) - \exp \left(\frac{-(z+\tau)^2}{4Dt} \right) \right) \cdot \exp \left(\frac{K}{1 + \left(\frac{\tau-z_m}{z_0} \right)^2} \right) \quad (7.18)$$

Algorithm 1: Calculation of a data point of $C(z, t)$

```

coefficient = C0/sqrt(4*pi*D*t);
wholeSumTau = 0;
tau = 0;
oldvalue = 0;
newvalue = 0;
sumTau = 1;
while sumTau > epsilon  $\vee$  tau < L do
    tau += deltaTau;
    newvalue = innerFunction(z, t, tau);
    sumTau = deltaTau*0.5*(oldvalue+newvalue);
    wholeSumTau += sumTau;
    oldvalue = newvalue;
dataPoint = new dataPoint(z, t, wholeSumTau*coefficient));

```

The inner function T can be easily calculated with numerical methods. For this purpose we use the so called "Proceeding to the limit" method [148].

$$\int_0^\infty T(z, t, \tau) d\tau \approx \sum_{n=1}^N \frac{1}{2} (T(z, t, (n-1)\Delta\tau) + T(z, t, n\Delta\tau)) \quad (7.19)$$

$$\frac{1}{2} (T(z, t, (n-1)\Delta\tau) + T(z, t, n\Delta\tau)) < \epsilon \quad \forall n > N \quad (7.20)$$

In this method, the function is divided into intervals of size $\Delta\tau$. These intervals are then summed with the trapezium rule. The upper limit of the integral remains uncertain. Instead, the integral is calculated until the sum of the intervals do not exceed a certain value ϵ .

This method is designed for a monotonically decreasing function, converging to zero. Internal function T does not conform to these criteria. Instead, it increases its value to the maximum. Nevertheless, we can use the numerical method, if you add the parameter L , which is an additional boundary beyond which the calculation of the integral occurs. First of all the algorithmic calculation of the function $C(z, t)$ is described using the pseudo code (Algorithm 1). Part of the algorithm requests the value of the inner function T . Calculation of the internal function is depicted in Algorithm 2. For further calculations it is necessary to average the calculated values for the given time t , since we do not consider the spacial resolution along the z axis. For this purpose the values are integrated using the trapezoidal rule. Algorithm 3 shows, how the values for $C(z, t)$ are finally calculated. The formulated model comprises four main parameters, each of which has

Algorithm 2: Internal function of the integral

```
innerFunction(z,t,tau)
return (exp(-(z-tau)*(z-tau)/(4*D*t)) + exp(-(z+tau)*(z+tau)/(4*D*t))) *
exp(K/(1+((tau-zM)*(tau-zM)/(z0*z0))));
```

Algorithm 3: Calculation of an averaged data point of C(t)

```
coefficient = C0/sqrt(4*pi*D*t);
sumZ = 0;
alterWertZ = 0;
for z = 0; z ≤ zMax; z += deltaZ do
    gesamtsumTau = 0;
    tau = 0;
    oldValue = 0;
    newValue = 0;
    sumTau = 1;
    while sumTau > epsilon ∨ tau < L do
        tau += deltaTau;
        newValue = innerFunction(z, t, tau);
        sumTau = deltaTau*0.5*(oldValue+newValue);
        wholeSumTau += sumTau;
        oldValue = newValue;
    sumZ += deltaZ*0.5*(oldValueZ+wholeSumTau*coefficient);
    oldValueZ = wholeSumTau*coefficient;
datenPunkt = new DataPoint(t, summeZ);
```

a significant effect on the final computations. Those parameters are D , K , z_0 and C_0 . It is necessary to conduct a parameter search, to get maximum correlation with experimental data. For this purpose, different sets of parameters are used. Each set is inserted into the model and is evaluated. Then we calculate the correlation between theoretical and experimental data. One set of parameters that corresponds to the maximal correlation is considered to be the closest to the real values.

To do this, a parameter space with a given grid resolution is defined. Increase of the resolution around a certain set values with maximal correlation leads to more precise results. Figure 7.5 illustrates the idea of the search for parameters in a grid space. The maximum of this graph corresponds to the maximal correlation. Therefore it can be concluded that the selected parameters actually describe the system. Due to the limitation of visual perception one can only show the correlation coefficient as a function of two parameters. The real calculated parameter space consists of five dimensions.

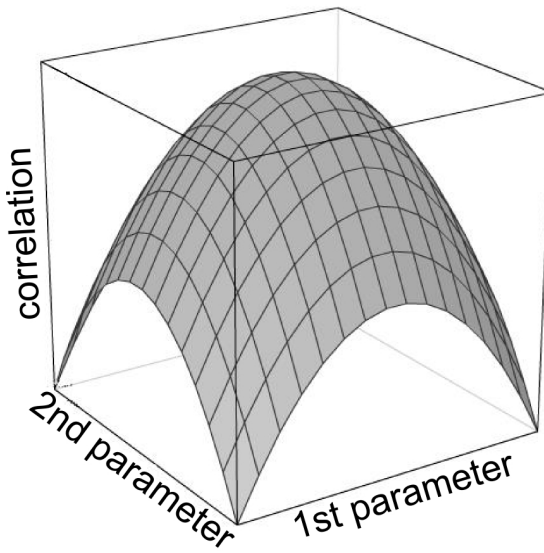


FIGURE 7.5: Search for the maximum correlation with two parameters in a parameter space, idealized illustration.

Correlation of experimental and theoretical data is calculated using the empirical correlation coefficient ([149]).

$$\text{corr}(x_i, y_i) = \frac{\sum_{i=1}^n (x_i - \bar{x}) \cdot (y_i - \bar{y})}{\sqrt{\sum_{i=1}^n (x_i - \bar{x})^2 \cdot \sum_{i=1}^n (y_i - \bar{y})^2}} \quad (7.21)$$

This equation basically "compares" two data sets and delivers the correlation value between 0 and 1. The x_i is the calculated data and y_i is the experimental data. Both data rows must have the same scale, otherwise they must be interpolated. Both data rows should also have the same amount of elements. The correlation coefficient is calculated numerically using following algorithm 4

Algorithm 4: Numerical calculation of the correlation coefficient

```

function correlation(double[] series1, double[] series2)
int length = series1.length > series2.length ? series2.length : series1.length;
double xAv = 0, yAv = 0;
for int index=0; index<length; index++ do
    xAv += series1[index];
    yAv += series2[index];
xAv = xAv/length;
yAv = yAv/length;
double sumCovariance = 0, sumDivX = 0, sumDivY = 0;
for int index=0; index<length; index++ do
    sumCovariance += (series1[index]-xAvg)*(series2[index]-yAvg);
    sumDivX += (series1[index]-xAvg)*(series1[index]-xAvg);
    sumDivY += (series2[index]-yAvg)*(series2[index]-yAvg);
return sumCovariance/sqrt(sumDivX*sumDivY);

```

7.4 Experimental implementation and tentative results

The AAO membranes that are used in this experiments are described in Section 2.2.2. The fluorescence mapping is described in Section 3.1.2. FRAP experiments where performed using confocal laser microscope Olympus LSM FV1000 with 60x oil objective (see Section 3.1.3). Figure 3.2 from Section 3.1.2 depicts the schematic arrangement of the components (not to scale).

A thin layer of immersion oil is applied to the lens to eliminate the influence of the refractive index of the air layer and to average this value for the whole system. The tested sample (AAO) is fixed on a glass substrate by hot glue. A small drop of glue is heated on the glass, then a small fragment of AAO is pressed to the molten glue with opened pores up. After that the glass substrate is fixed on the objective so the glass touches the oil layer and the AAO sample is on top.

The experiments where performed at 25°C. The thickness of used AAO membrane is 30 μm and the pore diameter is 60 nm. Native polybutadiene is present in a pure non crosslinked form. The $M_n = 33500$ and $PDI = 1.03$. Physical data of pure polymer is selected so as to coincide with the labelled polymer. The dye-labelled polymer, polybutadiene with perylene derivate, has an attached modified dye group (Figure 7.6). The $M_p = 37600$, $M_n = 36400$ and $PDI = 1.03$.

10 mg of non marked PB was mixed with 1 mg of perylene-labeled PB using toluene as solvent. After both substances are solved in a vial, the mixture is

put into a shaker in order to create a homogeneous substance. Figure 7.7 shows this mixture while two different phases of production. The first picture shows the polymeric mixture after two hours of shaking. Large clusters are visible and the whole substance is not homogeneous. The second picture shows the same mixture after almost twenty hours of shaking. The substance is homogeneous. The infiltration process of polymer mix in AAO membranes happens as follows: one creates the reservoir on top of the AAO by applying an a droplet of mixture and than let it infiltrate for several hours. Figure 7.8 shows an AAO membrane with $30\ \mu\text{m}$ thikness and $60\ \text{nm}$ pore diameter that is completely infiltrated with PB mixture.

After the AAO membrane is infiltrated, as is shown in Figure 7.8, it is possible to continue with photobleaching. First, a point in the middle of the infiltrated AAO

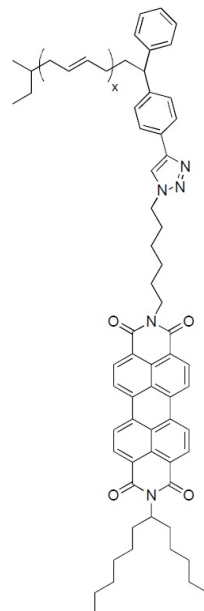


FIGURE 7.6: Perylene labeled polybutadiene.

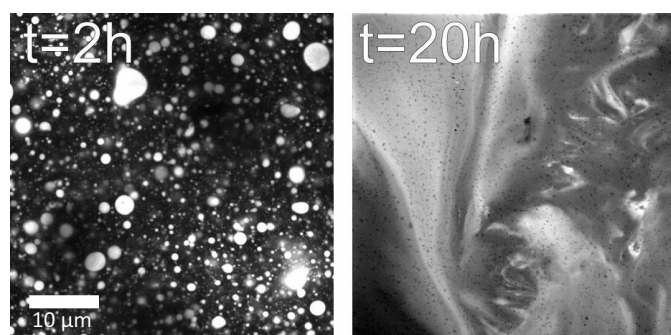


FIGURE 7.7: Homogeneity of the mixture of marked and pure polybutadiene after 2 and 20 hours. XY plane, picture taken with CLSM

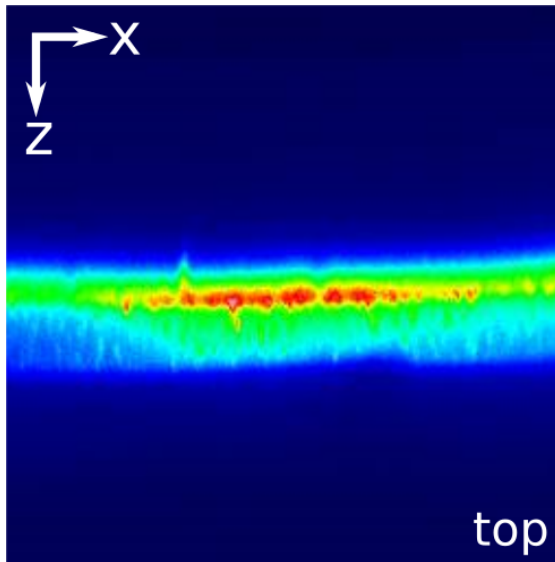


FIGURE 7.8: AAO membrane ($30\ \mu\text{m}$ membrane thickness and $60\ \text{nm}$ pore diameter) infiltrated with a polymer mixture. The edge length corresponds to $100\ \mu\text{m}$.

membrane is chosen in the x-z plane, the laser beam is focused on a single point in the x-y plane, the fluorescence intensity of this point is saved and plotted vs. bleaching time. The laser intensity is changed from 1% (observation mode, $1,7\ \mu\text{W}$) to 100% (bleaching mode, $180\ \mu\text{W}$). Figure 7.9 shows what happens with fluorescence intensity of the infiltrated membrane shown in Figure 7.8 during the photobleaching process. One can see that after about one second the fluorescence intensity starts to decrease. The bleaching took 4 seconds

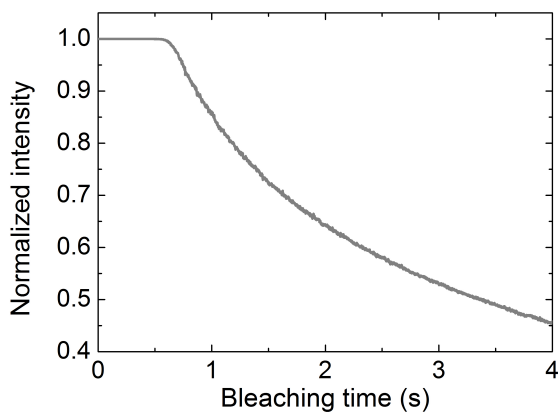


FIGURE 7.9: Intensity vs. Time during the bleaching process.

After the intensity reaches half of the initial value, the radiation intensity is reduced from the bleaching mode to the scanning mode, in order to detect fluorescence intensity, without disturbing it. The laser transitivity goes again to 1 %

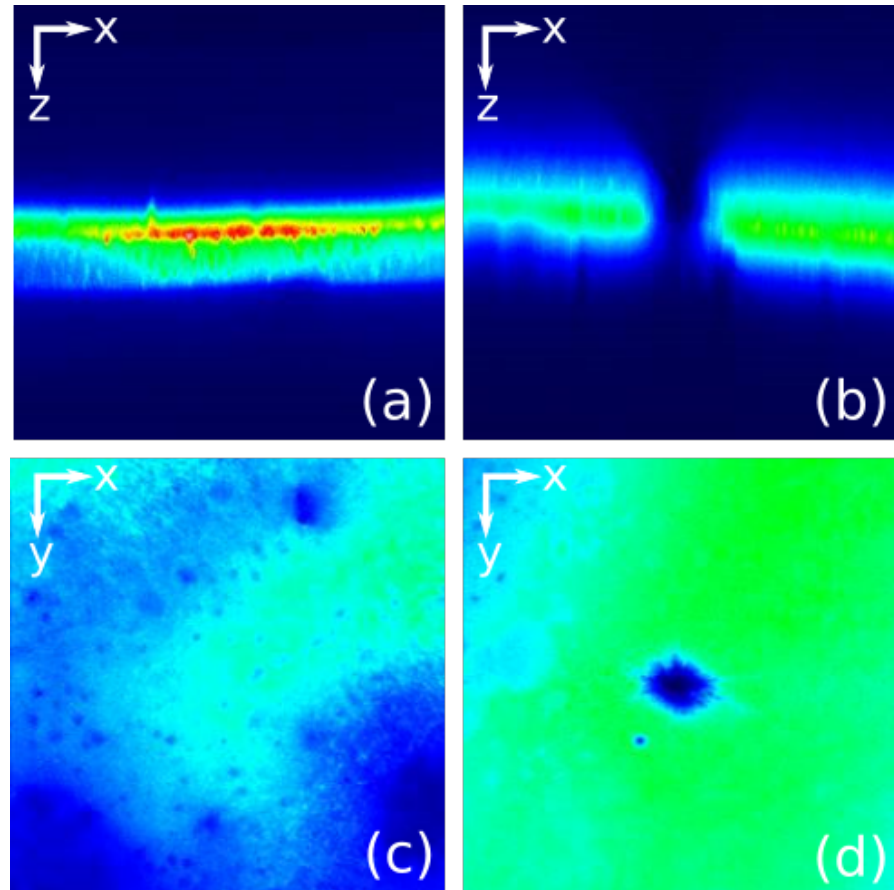


FIGURE 7.10: a) and b) show the x-z plane of infiltrated AAO membrane before and after photobleaching. c) and d) show the x-y plane of the same membrane before and after photobleaching. The edge length corresponds to $100 \mu\text{m}$.

($1,7 \mu\text{W}$). Figure 7.10 shows what happens in the x-y and x-z planes after photobleaching of infiltrated AAO membrane shown in Figure 7.8. In the x-y plane there is a photo-bleached spot with clearly reduced intensity that is surrounded by non photo-bleached PB-mixture. In the x-z plane the bleaching profile resembles a conical profile. The regeneration process begins as soon as the laser radiation intensity is set to minimum value and a reservoir of a polymer blend is put on top of the AAO. The photo-bleached molecules are diffusing into the reservoir and vice versa. All this results in a slow increase of fluorescence intensity in the observed bleached volume of AAO. The regeneration dynamics is saved as x-z-Intensity mapping pictures in chronological order. These pictures are evaluated using the spatio-temporal method described in Section 4.3. The results are shown in Figure 7.11.

Figure 7.11 shows the evaluation of the regeneration process. The intensity of the middle of the bleached area is extracted as described in Section 4.3 in order to

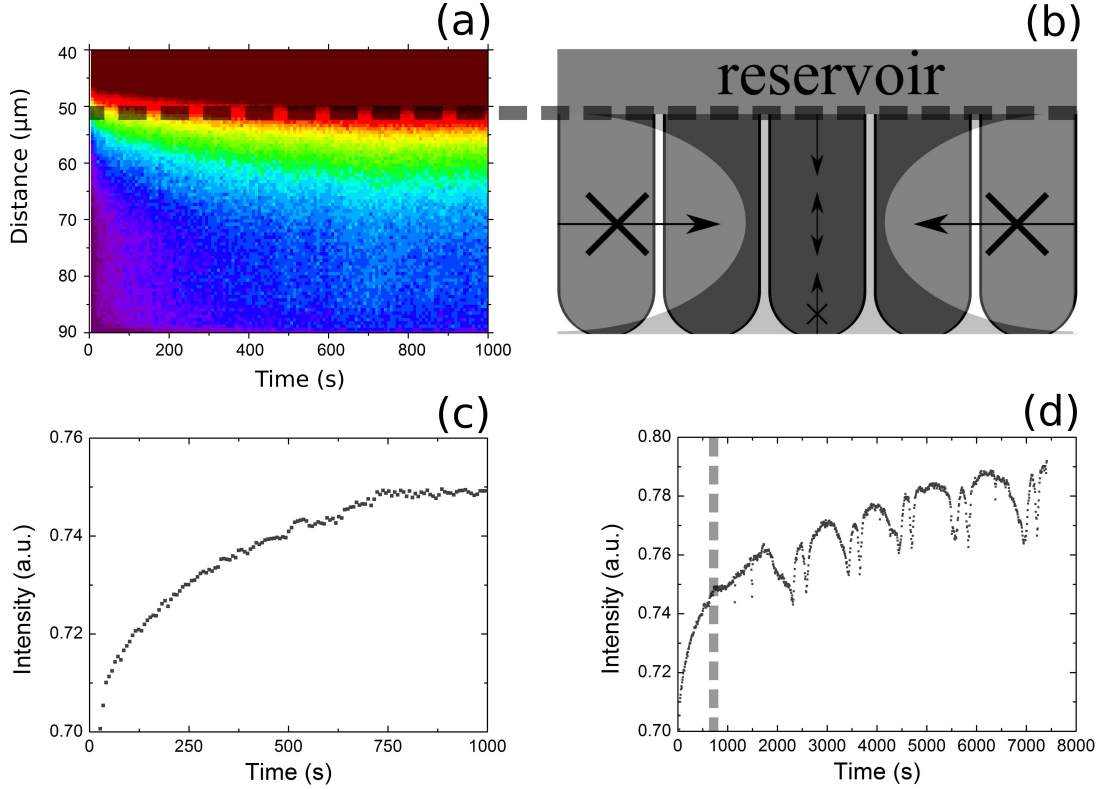


FIGURE 7.11: Regeneration process, intensity vs. regeneration time. (a) Spatiotemporal representation of regeneration process between 0 and 1000 seconds of observation; (b) Schematic arrangement of key elements in (a), the polymer reservoir is on top of AAO membrane, there is no exchange between infiltrated pores in x-direction, only in z-direction between reservoir and pore openings. (c) Integrated fluorescence intensity between 0 and 1000 seconds of the region that is shown in (a); (d) Depiction of the whole measured regeneration process based on the whole data extracted from the fluorescence mapping pictures during the complete measurement.

show the intensity evolution as a function of time integrated along the x-direction. This intensity evolution is shown in Figure 7.11(a). Figure 7.11(b) shows the ideal configuration of the bleached profile and the key elements that are shown in (a). The polymer reservoir is on top of AAO, the border between the AAO membrane and the reservoir is marked with semitransparent dashed line. Since the spatiotemporal profile consists of intensities along the z-direction in chronological order, it is possible to plot the integrated intensity of these profiles as a function of time. This plot is shown in Figure 7.11(c). Figure 7.11(d) shows the whole regeneration profile during the whole observation time. There are some artefacts visible after 1000 seconds of observation. Their origin is unknown. They might originate from mechanical movement of piezo elements or motors of the LSM FV1000 or because of air bubbles inside the oil layer that is between the glass slice and

the microscope objective.

Figure 7.12 illustrates the process of the search for maximal correlation between obtained experimental data that is shown in Figure 7.11(c) and Equation 7.15 using the algorithms that are described in Section 7.3 . All the parameters are fixed except the diffusion coefficient that is varied in order to maximize the correlation. Following parameters have been chosen for the calculation of maximal correlation coefficient:

- D varies from 1E-6 to 1E-4 with a resolution of 1E-6
- z_0 was set to 3.0
- K was set to 3
- C_0 was set to 1

The diffusion coefficient is varied in an interval between 1E-6 to 1E-4 with a resolution of 1E-6. The maximal correlation point corresponds to a diffusion coefficient that describes the diffusion process the best. The maximal correlation was calculated as 0,96084 which corresponds to a diffusion coefficient $D = 5 \cdot 10^{-5} \frac{\mu m^2}{s}$ or $D = 5 \cdot 10^{-13} \frac{cm^2}{s}$.

The experimental recovery curve shown in 7.11(c) and the calculated curve based on the optimal parameters are shown on Figure 7.13. Black dots are experimentally obtained data and blue line is theoretically calculated regeneration curve.

The calculated diffusion coefficient is relatively small when compared to some literature data. Pearson et. al [140] studied the viscosity and self-diffusion coefficient of hydrogenated polybutadiene using PFG-NMR methods. The diffusion coefficients were determined at 175°C and the lowest value is $D = 5 \cdot 6,3^{-12} \frac{cm^2}{s}$ for PB with Mn = 304000. The experiments shown in this section were performed at 25°C that is 150°C colder. That surely reduces the mobility of investigated PB molecules. However, the molecular mobility is also restricted due to the chain length, which is much smaller than shown in [140].

Fleischer and Appel [150] studied the chain length and temperature dependence of the self-diffusion of polyisoprene and polybutadiene in the melt using also using the PFG-NMR method. The lowest measured self diffusion coefficient of polybutadiene with Mn = 49900 at 100°C is $D = 5 \cdot 2^{-10} \frac{cm^2}{s}$ which is three order of magnitude faster than the results shown in Figure 7.13. Higher self diffusion might occur due to higher temperature. The most simple explanation for very low value for the

diffusion coefficient are the geometrical restrictions that are shown in Figure 7.11b and the lower temperature. The calculated diffusion coefficient does not really describe the self diffusion of PB, but rather the diffusion between the reservoir on top of AAO and the openings of the pores of AAO.

It must be mentioned that these results are rather indicative. The method presented here has yet to be optimized and tested.

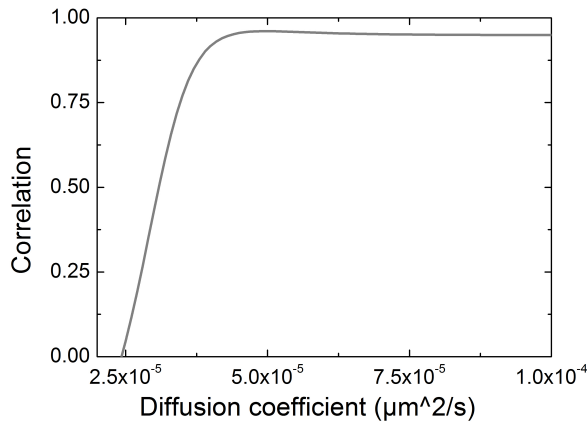


FIGURE 7.12: Parameter search for a diffusion coefficient with a given value for other two parameters.

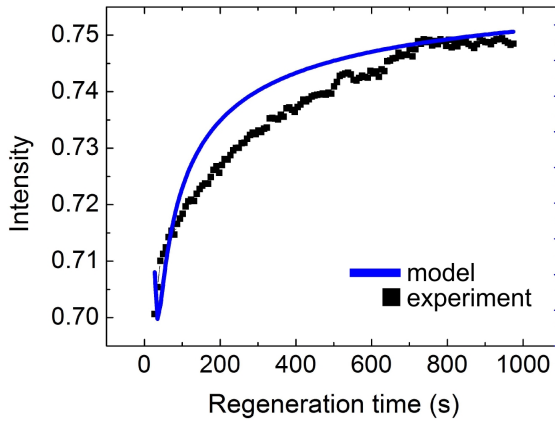


FIGURE 7.13: Measured (black dots) and simulated (blue line) regeneration curve of bleached area inside porous alumina that is illustrated on Figure 7.10

7.5 Conclusion and outlook

Since standard NMR methods are not effective when it comes to lower temperatures and higher chain lengths especially inside such porous materials as AAO,

a new non destructive method had to be developed. The theory of fluorescence recovery after photobleaching (FRAP) was modified to described one-dimensional diffusion inside AAO, because the self diffusion inside an AAO membrane can be considered as quasi-onedimensional. A numerical method was developed that allows calculation of maximal correlation and therefore diffusion coefficient based on the experimental data. The experimental data were obtained using dye-labelled PB molecules with perylene as a mixture with non marked PB. After complicated set of steps the diffusion coefficient was extracted.

It has to be specified that the performed experiments only deliver preliminary results. There are many reasons, why the obtained result should be treated very carefully.

The degree of infiltration is one parameter that plays critical role for the whole mathematical model. AAO samples should be filled completely with fluorescing PB derivative during the bleaching and regeneration phase. The mixture of pure PB and fluorescing PB is however not perfectly homogeneous (Figure 7.7). This leads to a different correlation between experimental and calculated data. Therefore one obtaines different diffusion coefficient.

Post-bleaching plays also a crucial role. The mathematical model is based on the implication that after the bleaching phase there is no post-bleaching. However, this effect can not be excluded.

Kinetics of photolytic reaction should be treated with caution. The mathematical modelling implies that the photobleaching reaction is a first order reaction. It does not have to be that way and is only assumed to simplify the out coming equations.

Crosslinking of PB is also a serious problem. The fluorescing PB could not be freshly prepared for the experiments. Therefore it is necessary to proceed from the fact that part of the molecule is in crosslinked state.

Chapter 8

Summary and outlook

This thesis deals with non destructive investigation methods of volatile and non-volatile liquids inside nanoporous materials. Nanoporous material with infiltrated liquid is a simple model system for a nanocomposite. Two nanoporous host systems where chosen. The first one is anodic aluminium oxide (AAO) as a model system for aligned separated pores with well defined morphology (Figure 2.7, Section 2.2.1). The second one is controlled porous glass (CPG) as model system for sponge like morphology (Figure 2.10, Section 2.3.1).

First, evaporation of ethanol as a model system for a volatile liquid was studied (Chapter 4). Using confocal microscopy and combined TGA/DSC analysis (both methods are described in corresponding Chapter 3, Sections 3.1 and 3.4) it was shown that evaporation of ethanol from CPG is partially driven by adiabatic burst events (Figures 4.3 and 4.5). The experimentally measured vaporization enthalpy differs significantly from the calculated vaporization enthalpy (Section 4.5) when assuming that evaporation process happens exclusively endothermic. It is assumed that about half of infiltrated ethanol evaporates adiabatically. Up to $10^7 \mu\text{m}^3$ of liquid ethanol can be converted to gas during such adiabatic burst event.

The reason for observed adiabatic burst evaporation is the geometry of CPG. The low pressure of ethanol that is caused by strong curvature of menisci inside nanopores leads to a metastable state. The trigger for an abrupt conversion of metastable liquid to gas is unstable meniscus configurations at air invasion fronts. The unstable configuration is caused by the build-up of high capillary pressures. The impetuous propagation of adiabatic evaporation bursts stops when a new stable configuration is reached.

Haines jumps is a mechanism that is known for the relaxation of unstable air invasion front [104]. However, this mechanism would only be responsible for reconfiguration of the menisci at the ethanol-air interface. The observed mass transfer away from the air invasion front is the reason why adiabatic evaporation bursts prevail over Haines jumps.

Observation of evaporation of ethanol from AAO confirmed that the main reason for adiabatic burst events is the geometry of CPG (Chapter 5). Measured evaporation profiles inside an AAO membrane (Figures 5.1 and 5.4) do not reveal any irregularities. Ethanol evaporates from straight, aligned and separated pores of AAO. Unstable configuration at the air invasion front is not observed.

In order to make ethanol evaporation visible for confocal microscopy, R6G was used as fluorescing marker (3.1.2). It was assumed that the presence of fluorescence signal in the x-z area (which covers the length and the hight of investigated membranes) is a direct indication of the presence of ethanol. This assumption had to be reconsidered due to significant grow in the integral fluorescence intensity along the z-axis after ethanol completely evaporated from AAO (Section 5.3, Figures 5.4 and 5.6b). The R6G molecules on the bottom are the primary source of fluorescence signal that is scattered along the whole AAO membrane and reaches the detector that is placed beyond the AAO membrane. Fluorescence signal at this position is interpreted as if it came from the point where it was measured. It is still necessary to understand the nature of fluorescence quenching and regeneration right after the complete evaporation of the solvent. Possible explanation is the absorption of surrounding water and regaining of fluorescing properties. However, this statement is speculative and must be proven by further experiments. Experiments on glass (Figure 5.6a) did not reveal any signal enhancement or regeneration after evaporation of ethanol. Time resolved 3D orientation spectroscopy (description in Chapter 3, Section 3.2) of R6G molecules on a glass surface and inside an AAO membrane did not show any differences on characteristic features. Therefore it can be concluded that angle distribution of R6G molecules is not a reason for observed signal reactivation and enhancement.

Polydimethylsiloxane (PDMS) and polybutadiene (PB) are used as model systems for non-volatile liquids. BLS study (Chapter 3, Section 3.3) of nanocomposites consisting of liquid PDMS and CPG revealed that the effective sound velocity inside PDMS infiltrated CPG with 2 nm average pore diameter is significantly higher than the effective sound velocity inside an empty CPG membrane (experimental results in Section 6.2, Figures 6.1, 6.2 and 6.3, Tables 6.1 and 6.2). This could

be explained by strong reduction of the mobility of infiltrated polymers. Similar effect was observed for CPG with 9 nm pore diameter. The mobility of infiltrated polymers might be influenced in the vicinity of the pore walls.

BLS studies of empty CPG membrane revealed presence of multiple phononic branches. The sound wave may have two different ways how to propagate through CPG - through the pore walls only (higher sound velocity) and through an effective medium including the air gaps (lower sound velocity) (Section 6.3.1). Only one sound velocity was measured inside infiltrated CPG membranes with 2 nm and 9 nm pore diameter, which support the theory of mode guiding.

In conclusion, studies were conducted on self diffusion of polybutadiene inside AAO membrane(Chapter 7). NMR techniques could not be applied due to very low temporal resolution. The underlying theory of fluorescence recovery after photobleaching (FRAP) that is usually applied for two-dimensional diffusion in biological probes was modified for one-dimensional diffusion geometry inside the pores of AAO (Section 7.2). In order to make diffusion visible for confocal microscopy dye-labelled polybutadiene was used as guest system. The obtained diffusion coefficient is three orders of magnitude lower than self diffusion of polybutadiene in a free melt that is known from literature(Section 7.4, [140], [150]). That can be explained by many factors. First, all results from the literature are obtained for higher temperatures. That increases the diffusion time. Second, diffusion under nano-confinement inside the pores of AAO is surely different to the diffusion process inside a free volume of polymer melt. It has to be specified that the performed experiments only deliver preliminary results. There are many reasons, why the obtained result should be treated very carefully.

In further research it is necessary to pay particular attention to the physics of R6G on the bottom of AAO. As mentioned above, it was possible to observe an intensity drop right after the moment when solvent completely evaporated, following by regeneration of fluorescence intensity. The nature of this phenomenon has not been understood properly.

It is also worth paying attention to the geometry of studied porous membranes. CPG and AAO are two extreme cases - sponge like morphology vs. well defined morphology. One should try to investigate evaporation of ethanol from membranes with mixed characteristic features.

The effect of mode-guiding could be calculated numerically in order to prove the idea of selective pressure-wave propagation through the whole medium and selectively only through the pore walls.

For a better implementation of FRAP in AAO a more liquid polymer mixture is needed in order have a quicker infiltration and regeneration times. Also the theory should be tested with different one dimensional geometries in order to improve the repeatability of the results.

Bibliography

- [1] R. M. Jones, *Mechanics of composite materials*, vol. 1. McGraw-Hill New York, 1975.
- [2] B. M. Novak *et al.*, “Hybrid nanocomposite materials-between inorganic glasses and organic polymers,” *Advanced Materials*, vol. 5, no. 6, pp. 422–433, 1993.
- [3] P. M. Ajayan, L. S. Schadler, and P. V. Braun, *Nanocomposite science and technology*. John Wiley & Sons, 2006.
- [4] D. Enke, F. Janowski, and W. Schwieger, “Porous glasses in the 21st century - a short review,” *Microporous and Mesoporous Materials*, vol. 60, no. 1, pp. 19–30, 2003.
- [5] W. Lee and S.-J. Park, “Porous anodic aluminum oxide: anodization and templated synthesis of functional nanostructures,” *Chemical Reviews*, vol. 114, no. 15, pp. 7487–7556, 2014.
- [6] Y. Wang, C. He, W. Xing, F. Li, L. Tong, Z. Chen, X. Liao, and M. Steinhart, “Nanoporous metal membranes with bicontinuous morphology from recyclable block-copolymer templates,” *Advanced Materials*, vol. 22, no. 18, pp. 2068–2072, 2010.
- [7] P. Van de Witte, P. Dijkstra, J. Van den Berg, and J. Feijen, “Phase separation processes in polymer solutions in relation to membrane formation,” *Journal of Membrane Science*, vol. 117, no. 1, pp. 1–31, 1996.
- [8] Q. Jiang and M. D. Ward, “Crystallization under nanoscale confinement,” *Chemical Society Reviews*, vol. 43, no. 7, pp. 2066–2079, 2014.

- [9] B. Vigolo, B. Vincent, J. Eschbach, P. Bourson, J.-F. Marêché, E. McRae, A. Mueller, A. Soldatov, J.-M. Hiver, A. Dahoun, *et al.*, “Multiscale characterization of single-walled carbon nanotube/polymer composites by coupling raman and brillouin spectroscopy,” *The Journal of Physical Chemistry C*, vol. 113, no. 41, pp. 17648–17654, 2009.
- [10] M. Tirrell, “Polymer self-diffusion in entangled systems,” *Rubber Chemistry and Technology*, vol. 57, no. 3, pp. 523–556, 1984.
- [11] C. Wei, D. Srivastava, and K. Cho, “Thermal expansion and diffusion coefficients of carbon nanotube-polymer composites,” *Nano Letters*, vol. 2, no. 6, pp. 647–650, 2002.
- [12] G. Q. Lu, X. S. Zhao, and T. K. Wei, *Nanoporous materials: science and engineering*, vol. 4. Imperial College Press, 2004.
- [13] N. Hüsing and U. Schubert, “Aerogels - airy materials: chemistry, structure, and properties,” *Angewandte Chemie International Edition*, vol. 37, no. 1-2, pp. 22–45, 1998.
- [14] J. Butler, R. Mair, D. Hoffmann, M. Hrovat, R. Rogers, G. Topulos, R. Walsworth, and S. Patz, “Measuring surface-area-to-volume ratios in soft porous materials using laser-polarized xenon interphase exchange nuclear magnetic resonance,” *Journal of Physics: Condensed Matter*, vol. 14, no. 13, p. L297, 2002.
- [15] H. A. Patel, S. H. Je, J. Park, D. P. Chen, Y. Jung, C. T. Yavuz, and A. Coskun, “Unprecedented high-temperature co₂ selectivity in n₂-phobic nanoporous covalent organic polymers,” *Nature Communications*, vol. 4, p. 1357, 2012.
- [16] L. Ge, P. Dai, S. Ge, and J. Yu, “High selectivity chemiluminescence sensor for determination of puerarin in diet foods/weight loss promoters based on novel rhodanine and monodisperse molecularly imprinted microspheres,” *Analytical Methods*, vol. 2, pp. 1506–1513, 2010.
- [17] D. A. Nield and A. Bejan, *Mechanics of Fluid Flow Through a Porous Medium*. Springer, 2013.
- [18] J. Montero-Moreno, M. Sarret, and C. Mueller, “Self-ordered porous alumina by two-step anodizing at constant current: Behaviour and evolution of the

- structure," *Microporous and Mesoporous Materials*, vol. 136, no. 1–3, pp. 68 – 74, 2010.
- [19] K. R. Hebert, S. P. Albu, I. Paramasivam, and P. Schmuki, "Morphological instability leading to formation of porous anodic oxide films," *Nature Materials*, vol. 11, no. 2, pp. 162–166, 2011.
- [20] G. D. Sulka, *Highly ordered anodic porous alumina formation by self-organized anodizing*. Wiley-VCH, Weinheim, Germany, 2008.
- [21] T. Kumeria, A. Santos, and D. Losic, "Nanoporous anodic alumina platforms: Engineered surface chemistry and structure for optical sensing applications," *Sensors*, vol. 14, no. 7, pp. 11878–11918, 2014.
- [22] N. Gaponenko, "Sol–gel derived films in meso-porous matrices: porous silicon, anodic alumina and artificial opals," *Synthetic Metals*, vol. 124, no. 1, pp. 125–130, 2001.
- [23] M. Steinhart, J. H. Wendorff, A. Greiner, R. B. Wehrspohn, K. Nielsch, J. Schilling, J. Choi, and U. Goesele, "Polymer nanotubes by wetting of ordered porous templates," *Science*, vol. 296, no. 5575, p. 1997, 2002.
- [24] S. Shingubara, "Fabrication of nanomaterials using porous alumina templates," *Journal of Nanoparticle Research*, vol. 5, no. 1-2, pp. 17–30, 2003.
- [25] Z. Yang, Z. Niu, X. Cao, Z. Yang, Y. Lu, Z. Hu, and C. C. Han, "Template synthesis of uniform 1d mesostructured silica materials and their arrays in anodic alumina membranes," *Angewandte Chemie International Edition*, vol. 42, no. 35, pp. 4201–4203, 2003.
- [26] M. Sander, A. Prieto, R. Gronsky, T. Sands, and A. Stacy, "Fabrication of high-density, high aspect ratio, large-area bismuth telluride nanowire arrays by electrodeposition into porous anodic alumina templates," *Advanced Materials*, vol. 14, no. 9, pp. 665–667, 2002.
- [27] T. Kumeria, M. M. Rahman, A. Santos, J. Ferre-Borrull, L. F. Marsal, and D. Losic, "Nanoporous anodic alumina rugate filters for sensing of ionic mercury: toward environmental point-of-analysis systems," *ACS applied materials & interfaces*, vol. 6, no. 15, pp. 12971–12978, 2014.

- [28] T. Kyotani, W. Xu, Y. Yokoyama, J. Inahara, H. Touhara, and A. Tomita, “Chemical modification of carbon-coated anodic alumina films and their application to membrane filter,” *Journal of Membrane Science*, vol. 196, no. 2, pp. 231 – 239, 2002.
- [29] R. K. Hart, “The oxidation of aluminium in dry and humid oxygen atmospheres,” *Proceedings of the Royal Society of London A: Mathematical, Physical and Engineering Sciences*, vol. 236, no. 1204, pp. 68–88, 1956.
- [30] C. Chang, D. Fraser, M. Grieco, T. Sheng, S. Haszko, R. Kerwin, R. Marcus, and A. Sinha, “Aluminum oxidation in water,” *Journal of The Electrochemical Society*, vol. 125, no. 5, pp. 787–792, 1978.
- [31] A. Despic and V. P. Parkhutik, “Electrochemistry of aluminum in aqueous solutions and physics of its anodic oxide,” in *Modern Aspects of Electrochemistry No. 20*, pp. 401–503, Springer, 1989.
- [32] F. Keller, M. Hunter, and D. Robinson, “Structural features of oxide coatings on aluminum,” *Journal of the Electrochemical Society*, vol. 100, no. 9, pp. 411–419, 1953.
- [33] H. Masuda, F. Hasegawa, and S. Ono, “Self-ordering of cell arrangement of anodic porous alumina formed in sulfuric acid solution,” *Journal of the electrochemical society*, vol. 144, no. 5, pp. L127–L130, 1997.
- [34] H. Masuda, K. Yada, and A. Osaka, “Self-ordering of cell configuration of anodic porous alumina with large-size pores in phosphoric acid solution,” *Japanese Journal of Applied Physics*, vol. 37, no. 11A, p. L1340, 1998.
- [35] G. D. Sulka and W. J. Stepniowski, “Structural features of self-organized nanopore arrays formed by anodization of aluminum in oxalic acid at relatively high temperatures,” *Electrochimica Acta*, vol. 54, no. 14, pp. 3683–3691, 2009.
- [36] R. C. Alkire, Y. Gogotsi, P. Simon, and A. Eftekhari, *Nanostructured materials in electrochemistry*. John Wiley & Sons, 2008.
- [37] D. Losic and A. Santos, *Nanoporous Alumina: Fabrication, Structure, Properties and Applications*, vol. 219. Springer, 2015.

- [38] H. Masuda and K. Fukuda, “Ordered metal nanohole arrays made by a two-step replication of honeycomb structures of anodic alumina,” *Science*, vol. 268, no. 5216, pp. 1466–1468, 1995.
- [39] O. Jessensky, F. Müller, and U. Gösele, “Self-organized formation of hexagonal pore arrays in anodic alumina,” *Applied Physics Letters*, vol. 72, no. 10, pp. 1173–1175, 1998.
- [40] A. F. Feil, M. V. da Costa, L. Amaral, S. R. Teixeira, P. Migowski, J. Dupont, G. Machado, and S. B. Peripolli, “The influence of aluminum grain size on alumina nanoporous structure,” *Journal of Applied Physics*, vol. 107, no. 2, pp. –, 2010.
- [41] C. Cheng, *Electro-chemo-mechanics of anodic porous alumina nano-honeycombs: self-ordered growth and actuation*. Springer, 2015.
- [42] G. Mie, “Beiträge zur optik trüber medien, speziell kolloidaler metallösungen,” *Annalen der Physik*, vol. 330, no. 3, pp. 377–445, 1908.
- [43] N. P. Bansal and R. H. Doremus, *Handbook of glass properties*. Elsevier, 2013.
- [44] M. O. Adebajo, R. L. Frost, J. T. Kloprogge, O. Carmody, and S. Kokot, “Porous materials for oil spill cleanup: a review of synthesis and absorbing properties,” *Journal of Porous Materials*, vol. 10, no. 3, pp. 159–170, 2003.
- [45] L. M. Ellerby, C. R. Nishida, *et al.*, “Encapsulation of proteins in transparent porous silicate glasses prepared by the sol-gel method,” *Science*, vol. 255, no. 5048, p. 1113, 1992.
- [46] J. Walsh, W. Brace, and A. England, “Effect of porosity on compressibility of glass,” *Journal of the American Ceramic Society*, vol. 48, no. 12, pp. 605–608, 1965.
- [47] V. L. Mauricio, O. L. Alves, and I. O. Mazali, “Macroporous glass monoliths prepared from powdered niobium phosphate glass by fast sintering,” *Materials Characterization*, vol. 62, no. 3, pp. 263 – 267, 2011.
- [48] N. Murase and T. Yazawa, “Partially reduced cuprous oxide nanoparticles formed in porous glass reaction fields,” *Journal of the American Ceramic Society*, vol. 84, no. 10, pp. 2269–2273, 2001.

- [49] L. D. Gelb, K. Gubbins, R. Radhakrishnan, and M. Sliwinska-Bartkowiak, “Phase separation in confined systems,” *Reports on Progress in Physics*, vol. 62, no. 12, p. 1573, 1999.
- [50] E. Kierlik, P. Monson, M. Rosinberg, L. Sarkisov, and G. Tarjus, “Capillary condensation in disordered porous materials: Hysteresis versus equilibrium behavior,” *Physical review letters*, vol. 87, no. 5, p. 055701, 2001.
- [51] K. Page and P. Monson, “Phase equilibrium in a molecular model of a fluid confined in a disordered porous material,” *Physical Review E*, vol. 54, no. 1, p. R29, 1996.
- [52] A. P. Hahn, “Spherical sodium borosilicate initial glass.”
http://www.chemie.uni-halle.de/bereiche_der_chemie/technische_chemie/ak_prof._hahn, 2015 (accessed August 7, 2015).
- [53] J. Scheve, “Poröse gläser herstellung, eigenschaften und anwendung,” *Zeitschrift für Chemie*, vol. 22, no. 10, pp. 396–396, 1982.
- [54] J. W. Cahn, “Phase separation by spinodal decomposition in isotropic systems,” *The Journal of Chemical Physics*, vol. 42, no. 1, pp. 93–99, 1965.
- [55] A. J. Schwartz, J. S. Huang, and W. I. Goldburg, “Spinodal decomposition in a binary liquid mixture near the critical point,” *The Journal of Chemical Physics*, vol. 62, no. 5, pp. 1847–1852, 1975.
- [56] Y. Jean, “Positron annihilation spectroscopy for chemical analysis: a novel probe for microstructural analysis of polymers,” *Microchemical Journal*, vol. 42, no. 1, pp. 72–102, 1990.
- [57] W. Gille, O. Kabisch, S. Reichl, D. Enke, D. Fürst, and F. Janowski, “Characterization of porous glasses via small-angle scattering and other methods,” *Microporous and Mesoporous Materials*, vol. 54, no. 1–2, pp. 145 – 153, 2002.
- [58] H. MacDonell, J. Noonan, and J. Williams, “Porous glass as an adsorption medium for gas chromatography.,” *Analytical Chemistry*, vol. 35, no. 9, pp. 1253–1255, 1963.
- [59] L. D. Gelb and K. E. Gubbins, “Pore size distributions in porous glasses: A computer simulation study,” *Langmuir*, vol. 15, no. 2, pp. 305–308, 1999.

- [60] S. Paddock, T. Fellers, and M. Davidson, *Confocal microscopy*. Springer, 2001.
- [61] S. Nie, D. T. Chiu, and R. N. Zare, “Probing individual molecules with confocal fluorescence microscopy,” *Science*, vol. 266, no. 5187, pp. 1018–1021, 1994.
- [62] H. Chiu and S. Quake, “Single-molecule fluorescence observed with mercury lamp illumination,” *Biotechniques*, vol. 27, no. 5, pp. 1008–1014, 1999.
- [63] M. Bratzel, R. Dagnall, and J. Winefordner, “Evaluation of 150-w eimac xenon lamp for atomic fluorescence flame spectrometry,” *Analytica Chimica Acta*, vol. 52, no. 1, pp. 157–159, 1970.
- [64] W. Duley, *Laser processing and analysis of materials*. Springer Science & Business Media, 2012.
- [65] D. R. Sandison, R. M. Williams, K. S. Wells, J. Strickler, and W. W. Webb, “Quantitative fluorescence confocal laser scanning microscopy (clsm),” in *Handbook of Biological Confocal Microscopy*, pp. 39–53, Springer, 1995.
- [66] H. C. Ishikawa-Ankerhold, R. Ankerhold, and G. P. C. Drummen, “Advanced fluorescence microscopy techniques frap, flip, flap, fret and flim,” *Molecules*, vol. 17, no. 4, pp. 4047–4132, 2012.
- [67] N. N. Alder, R. E. Jensen, and A. E. Johnson, “Fluorescence mapping of mitochondrial tim23 complex reveals a water-facing, substrate-interacting helix surface,” *Cell*, vol. 134, no. 3, pp. 439–450, 2008.
- [68] I. Rosenthal, “Photochemical stability of rhodamine 6g in solution,” *Optics Communications*, vol. 24, no. 2, pp. 164 – 166, 1978.
- [69] A. Penzkofer and Y. Lu, “Fluorescence quenching of rhodamine 6g in methanol at high concentration,” *Chemical Physics*, vol. 103, no. 2–3, pp. 399 – 405, 1986.
- [70] R. Börner, D. Kowerko, C. Von Borczyskowski, and C. G. Hübner, “Time resolved 3d orientation spectroscopy: experimental realization and simulation,” in *SPIE BiOS*, pp. 79050D–79050D, International Society for Optics and Photonics, 2011.

- [71] G. Benedek and K. Fritsch, “Brillouin scattering in cubic crystals,” *Physical Review*, vol. 149, no. 2, p. 647, 1966.
- [72] L. D. Landau and E. M. Lifshitz, *Course of theoretical physics*. Elsevier, 2013.
- [73] B. Chu, *Laser light scattering*. Elsevier, 1974.
- [74] W. C. Chew, *Waves and fields in inhomogeneous media*, vol. 522. IEEE press New York, 1995.
- [75] G. Landsberg, “Optika (optics),” *Moscow, Fizmatlit Publ*, 1976.
- [76] D. Meschede, *Gerthsen Physik*. Springer, 2010.
- [77] M. Born and E. Wolf, *Principles of optics: electromagnetic theory of propagation, interference and diffraction of light*. Cambridge university press, 1999.
- [78] R. Ditchburn, *Physical Optics*. Nauka, 1965.
- [79] T. Still, *High frequency acoustics in colloid-based meso- and nanostructures by spontaneous Brillouin light scattering*. PhD thesis, Johannes Gutenberg Universitaet Mainz, 2009.
- [80] S. M. Lindsay, M. W. Anderson, and S. J.R., “Construction and alignment of a high performance multipass vernier tandem fabry-perot interferometer,” *Review of Scientific Instruments*, vol. 52(10), pp. 1478–1486, 1981.
- [81] A. Sato, *Nanoporous Alumina based Hypersonic Phononic Hybrid Structures Studied by Brillouin Spectroscopy*. PhD thesis, University of Mainz, 2009.
- [82] G. Höhne, W. Hemminger, and H.-J. Flammersheim, *Differential scanning calorimetry*. Springer Science & Business Media, 2003.
- [83] H. Wang, P. Skeldon, and G. Thompson, “Thermogravimetric–differential thermal analysis of the solid-state decomposition of ammonium tetrathiomolybdate during heating in argon,” *Journal of Materials Science*, vol. 33, no. 12, pp. 3079–3083, 1998.
- [84] A. Coats and J. Redfern, “Thermogravimetric analysis, a review.,” *Analyst*, vol. 88, no. 1053, pp. 906–924, 1963.

- [85] N. A. Tikhonov, I. V. Arkhangelsky, S. S. Belyaev, and A. T. Matveev, “Carbonization of polymeric nonwoven materials,” *Thermochimica Acta*, vol. 486, no. 1–2, pp. 66 – 70, 2009.
- [86] R. Narayanan and R. M. Laine, “Synthesis and characterization of precursors for group ii metal aluminates,” *Applied Organometallic Chemistry*, vol. 11, no. 10-11, pp. 919–927, 1997.
- [87] S. Ichilmann, K. Rücker, M. Haase, D. Enke, M. Steinhart, and L. Xue, “Adiabatic burst evaporation from bicontinuous nanoporous membranes,” *Nanoscale*, vol. 7, no. 20, pp. 9185–9193, 2015.
- [88] S. J. Kowalski, *Drying of porous materials*. Springer, 2007.
- [89] T. Heinrich, U. Klett, and J. Fricke, “Aerogels – nanoporous materials part i: Sol-gel process and drying of gels,” *Journal of Porous Materials*, vol. 1, no. 1, pp. 7–17, 1995.
- [90] K. Masters *et al.*, “Spray drying handbook.,” *Spray drying handbook.*, no. Ed. 3, 1979.
- [91] J. Philip and D. De Vries, “Moisture movement in porous materials under temperature gradients,” *Eos, Transactions American Geophysical Union*, vol. 38, no. 2, pp. 222–232, 1957.
- [92] D. Rose, “Water movement in porous materials iii. evaporation of water from soil,” *Journal of Physics D: Applied Physics*, vol. 1, no. 12, p. 1779, 1968.
- [93] N. Sghaier, S. Geoffroy, M. Prat, H. Elouabi, and S. B. Nasrallah, “Evaporation-driven growth of large crystallized salt structures in a porous medium,” *Physical Review E*, vol. 90, no. 4, p. 042402, 2014.
- [94] C. J. Brinker, Y. Lu, A. Sellinger, and H. Fan, “Evaporation-induced self-assembly: nanostructures made easy,” *Advanced Materials*, vol. 11, no. 7, pp. 579–585, 1999.
- [95] D. Karamanis, E. Kyritsi, and S. Krimparis, “Well-ordered nanoporous materials for low-temperature water phase changes and solar evaporative cooling,” *Solar Energy Materials and Solar Cells*, vol. 139, pp. 34–43, 2015.

- [96] C. K. Wei, H. T. Davis, E. A. Davis, and J. Gordon, “Evaporation from porous media - a capillary model of a penetrating front,” *Chemical Engineering Communications*, vol. 56, no. 1-6, pp. 269–284, 1987.
- [97] J. B. Laurindo and M. Prat, “Numerical and experimental network study of evaporation in capillary porous media. drying rates,” *Chemical Engineering Science*, vol. 53, no. 12, pp. 2257–2269, 1998.
- [98] J. B. Laurindo and M. Prat, “Numerical and experimental network study of evaporation in capillary porous media. phase distributions,” *Chemical Engineering Science*, vol. 51, no. 23, pp. 5171–5185, 1996.
- [99] A. Hunt, R. Ewing, and B. Ghanbarian, *Percolation theory for flow in porous media*, vol. 880. Springer, 2014.
- [100] I. Tsipmanogiannis, Y. Yortsos, S. Poulou, N. Kanellopoulos, and A. Stubos, “Scaling theory of drying in porous media,” *Physical Review E*, vol. 59, no. 4, p. 4353, 1999.
- [101] J. Page, J. Liu, B. Abeles, H. Deckman, and D. Weitz, “Pore-space correlations in capillary condensation in vycor,” *Physical review letters*, vol. 71, no. 8, p. 1216, 1993.
- [102] A. Thompson, A. Katz, and R. Raschke, “Mercury injection in porous media: A resistance devil’s staircase with percolation geometry,” *Physical review letters*, vol. 58, no. 1, p. 29, 1987.
- [103] S. Berg, H. Ott, S. A. Klapp, A. Schwing, R. Neiteler, N. Brussee, A. Makurat, L. Leu, F. Enzmann, J.-O. Schwarz, *et al.*, “Real-time 3d imaging of haines jumps in porous media flow,” *Proceedings of the National Academy of Sciences*, vol. 110, no. 10, pp. 3755–3759, 2013.
- [104] W. B. Haines, “Studies in the physical properties of soil. v. the hysteresis effect in capillary properties, and the modes of moisture distribution associated therewith,” *The Journal of Agricultural Science*, vol. 20, no. 01, pp. 97–116, 1930.
- [105] S. Berg, R. Armstrong, H. Ott, A. Georgiadis, S. Klapp, A. Schwing, R. Neiteler, N. Brussee, A. Makurat, L. Leu, *et al.*, “Multiphase flow in porous rock imaged under dynamic flow conditions with fast x-ray computed microtomography,” *Petrophysics*, vol. 55, no. 04, pp. 304–312, 2014.

- [106] R. T. Armstrong and S. Berg, “Interfacial velocities and capillary pressure gradients during haines jumps,” *Physical Review E*, vol. 88, no. 4, p. 043010, 2013.
- [107] D. R. Lide, ed., *CRC Handbook of Chemistry and Physics, 87th Edition*. CRC Press, 2006.
- [108] N. R. Tas, P. Mela, T. Kramer, J. Berenschot, and A. van den Berg, “Capillarity induced negative pressure of water plugs in nanochannels,” *Nano Letters*, vol. 3, no. 11, pp. 1537–1540, 2003.
- [109] T. D. Wheeler and A. D. Stroock, “The transpiration of water at negative pressures in a synthetic tree,” *Nature*, vol. 455, no. 7210, pp. 208–212, 2008.
- [110] O. Vincent, P. Marmottant, P. A. Quinto-Su, and C.-D. Ohl, “Birth and growth of cavitation bubbles within water under tension confined in a simple synthetic tree,” *Physical Review Letters*, vol. 108, no. 18, p. 184502, 2012.
- [111] R. Zhang, Y. Ikoma, and T. Motooka, “Negative capillary-pressure-induced cavitation probability in nanochannels,” *Nanotechnology*, vol. 21, no. 10, p. 105706, 2010.
- [112] H.-J. Butt, K. Graf, and M. Kappl, *Physics and chemistry of interfaces*. John Wiley & Sons, 2004.
- [113] L. Xu, S. Davies, A. B. Schofield, and D. A. Weitz, “Dynamics of drying in 3d porous media,” *Physical Review Letters*, vol. 101, no. 9, p. 094502, 2008.
- [114] N. Shokri, P. Lehmann, and D. Or, “Liquid-phase continuity and solute concentration dynamics during evaporation from porous media: Pore-scale processes near vaporization surface,” *Physical Review E*, vol. 81, no. 4, p. 046308, 2010.
- [115] N. Shokri and M. Sahimi, “Structure of drying fronts in three-dimensional porous media,” *Physical Review E*, vol. 85, no. 6, p. 066312, 2012.
- [116] D. Or and M. Tuller, “Cavitation during desaturation of porous media under tension,” *Water Resources Research*, vol. 38, no. 5, pp. 19–1, 2002.
- [117] C. Duan, R. Karnik, M.-C. Lu, and A. Majumdar, “Evaporation-induced cavitation in nanofluidic channels,” *Proceedings of the National Academy of Sciences*, vol. 109, no. 10, pp. 3688–3693, 2012.

- [118] D. Turnbull, “Kinetics of heterogeneous nucleation,” *The Journal of Chemical Physics*, vol. 18, no. 2, pp. 198–203, 1950.
- [119] X. She, G. Song, J. Li, P. Han, S. Yang, W. Shulong, and Z. Peng, “Non-polar polymer nanotubes and nanowires fabricated by wetting anodic aluminium oxide template,” *Polymer Journal*, vol. 38, no. 7, pp. 639–642, 2006.
- [120] M. Fischer and J. Georges, “Fluorescence quantum yield of rhodamine 6g in ethanol as a function of concentration using thermal lens spectrometry,” *Chemical Physics Letters*, vol. 260, no. 1–2, pp. 115 – 118, 1996.
- [121] Y. Lu and A. Penzkofer, “Absorption behaviour of methanolic rhodamine 6g solutions at high concentration,” *Chemical Physics*, vol. 107, no. 2, pp. 175–184, 1986.
- [122] A. Penzkofer and W. Leupacher, “Fluorescence behaviour of highly concentrated rhodamine 6g solutions,” *Journal of Luminescence*, vol. 37, no. 2, pp. 61–72, 1987.
- [123] C. Levelut and J. Pelous, “Acoustic properties of a porous glass (vcor) at hypersonic frequencies,” *Journal of Physics: Condensed Matter*, vol. 19, no. 41, p. 416110, 2007.
- [124] C.-s. Zha, R. J. Hemley, H.-k. Mao, T. S. Duffy, and C. Meade, “Acoustic velocities and refractive index of sio 2 glass to 57.5 gpa by brillouin scattering,” *Physical Review B*, vol. 50, no. 18, p. 13105, 1994.
- [125] V. M. Litvinov and H. W. Spiess, “²h nmr study of molecular motions in polydimethylsiloxane and its mixtures with aerosils,” *Die Makromolekulare Chemie*, vol. 192, no. 12, pp. 3005–3019, 1991.
- [126] K. U. Kirst, F. Kremer, and V. M. Litvinov, “Broad-band dielectric spectroscopy on the molecular dynamics of bulk and adsorbed poly(dimethylsiloxane),” *Macromolecules*, vol. 26, no. 5, pp. 975–980, 1993.
- [127] G. Tsagaropoulos and A. Eisenberg, “Dynamic mechanical study of the factors affecting the two glass transition behavior of filled polymers. similarities and differences with random ionomers,” *Macromolecules*, vol. 28, no. 18, pp. 6067–6077, 1995.

- [128] T. Cosgrove, M. J. Turner, and D. R. Thomas, “The adsorption of polydimethylsiloxane onto silica from the melt,” *Polymer*, vol. 38, no. 15, pp. 3885–3892, 1997.
- [129] G. Evmenenko, H. Mo, S. Kewalramani, and P. Dutta, “Conformational rearrangements in interfacial region of polydimethylsiloxane melt films,” *Polymer*, vol. 47, no. 3, pp. 878–882, 2006.
- [130] D. Fragiadakis, P. Pissis, and L. Bokobza, “Glass transition and molecular dynamics in poly(dimethylsiloxane)/silica nanocomposites,” *Polymer*, vol. 46, no. 16, pp. 6001 – 6008, 2005.
- [131] R. G. Horn and J. N. Israelachvili, “Molecular organization and viscosity of a thin film of molten polymer between two surfaces as probed by force measurements,” *Macromolecules*, vol. 21, no. 9, pp. 2836–2841, 1988.
- [132] A. Sato, W. Knoll, Y. Pennec, B. Djafari-Rouhani, G. Fytas, and M. Steinhart, “Anisotropic propagation and confinement of high frequency phonons in nanocomposites,” *The Journal of Chemical Physics*, vol. 130, no. 11, pp. –, 2009.
- [133] A. Polian, D. Vo-Thanh, and P. Richet, “Elastic properties of a-sio 2 up to 2300k from brillouin scattering measurements,” *EPL (Europhysics Letters)*, vol. 57, no. 3, p. 375, 2002.
- [134] A. Dawidowicz, J. Matusewicz, and J. Wysocka-Lisek, “Determination of residual boron in thermally treated controlled-porosity glasses, by colorimetry, spectrography and isotachophoresis,” *Talanta*, vol. 36, no. 5, pp. 581–584, 1989.
- [135] Y. Ryabov, A. Gutina, V. Arkhipov, and Y. Feldman, “Dielectric relaxation of water absorbed in porous glass,” *The Journal of Physical Chemistry B*, vol. 105, no. 9, pp. 1845–1850, 2001.
- [136] M. Agamalian, J. Drake, S. Sinha, and J. Axe, “Neutron diffraction study of the pore surface layer of vycor glass,” *Physical Review E*, vol. 55, no. 3, p. 3021, 1997.
- [137] L. Zhuravlev, “Concentration of hydroxyl groups on the surface of amorphous silicas,” *Langmuir*, vol. 3, no. 3, pp. 316–318, 1987.

- [138] A. D. Pierce *et al.*, *Acoustics: an introduction to its physical principles and applications*. Acoustical Society of America Melville, NY, 1991.
- [139] T. Lodge, N. Rotstein, and S. Prager, “Dynamics of entangled polymer liquids: Do linear chains reptate?,” *Advances in Chemical Physics*, vol. 79, pp. 1–1, 1992.
- [140] D. S. Pearson, L. J. Fetters, W. W. Graessley, G. Ver Strate, and E. von Meerwall, “Viscosity and self-diffusion coefficient of hydrogenated polybutadiene,” *Macromolecules*, vol. 27, no. 3, pp. 711–719, 1994.
- [141] K. Braeckmans, K. Remaut, R. E. Vandenbroucke, B. Lucas, S. C. De Smedt, and J. Demeester, “Line frap with the confocal laser scanning microscope for diffusion measurements in small regions of 3-d samples,” *Biophysical Journal*, vol. 92, no. 6, pp. 2172–2183, 2007.
- [142] A. Lopez, L. Dupou, A. Altibelli, J. Trotard, and J. Tocanne, “Fluorescence recovery after photobleaching (frap) experiments under conditions of uniform disk illumination. critical comparison of analytical solutions, and a new mathematical method for calculation of diffusion coefficient d,” *Biophysical Journal*, vol. 53, no. 6, pp. 963 – 970, 1988.
- [143] A. M. Weiss, T. Saraidarov, and R. Reisfeld, “Confocal microscopy for characterization of porous sol–gel glasses incorporating luminescent dyes,” *Optical Materials*, vol. 16, no. 1, pp. 15–20, 2001.
- [144] D. Axelrod, D. Koppel, J. Schlessinger, E. Elson, and W. Webb, “Mobility measurement by analysis of fluorescence photobleaching recovery kinetics.,” *Biophysical Journal*, vol. 16, no. 9, p. 1055, 1976.
- [145] D. Soumpasis, “Theoretical analysis of fluorescence photobleaching recovery experiments,” *Biophysical Journal*, vol. 41, no. 1, pp. 95 – 97, 1983.
- [146] K. Braeckmans, L. Peeters, N. N. Sanders, S. C. De Smedt, and J. Demeester, “Three-dimensional fluorescence recovery after photobleaching with the confocal scanning laser microscope,” *Biophysical Journal*, vol. 85, no. 4, pp. 2240–2252, 2003.
- [147] Wikipedia, “Gaussian beam — Wikipedia, the free encyclopedia.” <https://commons.wikimedia.org/w/index.php?title=File:>

- GaussianBeamWaist.svg&oldid=156837785, 2015 (accessed September 21, 2015).
- [148] P. J. Davis and P. Rabinowitz, *Numerical integration*. Blaisdell Publishing Company London, 1967.
- [149] L. Sachs and J. Hedderich, “Angewandte statistik,” 2008.
- [150] G. Fleischer and M. Appel, “Chain length and temperature dependence of the self-diffusion of polyisoprene and polybutadiene in the melt,” *Macromolecules*, vol. 28, no. 21, pp. 7281–7283, 1995.

Declaration of Authorship

I, Sachar Ichilmann, declare that this thesis titled, Nondestructive Investigation of Guest Evaporation and Dynamics in Nanoporous Hosts and the work presented in it are my own. I confirm that:

- This work was done wholly or mainly while in candidature for a research degree at this University.
- Where any part of this thesis has previously been submitted for a degree or any other qualification at this University or any other institution, this has been clearly stated.
- Where I have consulted the published work of others, this is always clearly attributed.
- Where I have quoted from the work of others, the source is always given. With the exception of such quotations, this thesis is entirely my own work.
- I have acknowledged all main sources of help.
- Where the thesis is based on work done by myself jointly with others, I have made clear exactly what was done by others and what I have contributed myself.

Signed:

Date:

Acknowledgements

First of all, I would like to thank Prof. Dr. Steinhart for his great support and constant commitment throughout the project.

I want to thank Prof. Dr. Fytas and Dr. Schneider for collaboration, their support with the measurements of CPG spectra and valuable discussions concerning their interpretation.

I would like to thank Prof. Dr. Saalwächter for valuable discussions and the idea to investigate the diffusion properties of polymers using dye-labelled polymers.

I want to thank Prof. Dr. Hübner for collaboration, valuable discussions, his help with CLSM measurements and angle-distribution measurements and his idea to use FRAP for one-dimmensional diffusion in AAO.

My thanks to Prof. Dr. Müller and Dr. Hanisch for the production of perylene-marked PB.

I am thankful to Dr. Longian Xue for his idea regarding the evaporation dynamics from porous hosts and his constant commitment, which led to a scientific publication.

My thanks to Prof. Dr. Enke for collaboration and valuable discussions.

I am thankful to Prof. Dr. Haase for his help with understanding the intensity profiles of CLSM experiments.

I would like to thank Mrs. Rücker for her support during the TGA measurements.

I am very thankful to the technical support by the Centre of Advanced Light Microscopy and Dr. Kurre for his support during the CLSM experiments.

I want to thank Mr. Ott for writing java code for determination of diffusion coefficient of FRAP experiments as a part of his bachelor thesis.

My thanks to Mr. Kähler and Mr. Leitmann for their active and diligent work during their bachelor projects.

I would like to thank Dr. Schaefer for long and meaningful discussions and a possibility to be a co-author in his scientific publications.

I want to thank my colleagues for the great time I had working together. The atmosphere, support and friendship was really enjoyable.

Special thanks to Mrs. Gunkel, Mrs. Hess, Mrs. Hartmann. and Mr. Tobergte.

Last but not least, I wish to thank my family who has always supported me.